The Organic Component as a Ligand in a Polymeric Coordination Complex Cation

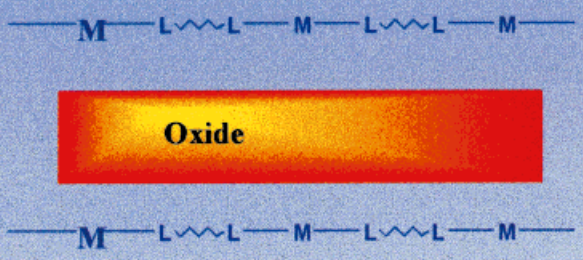

a)

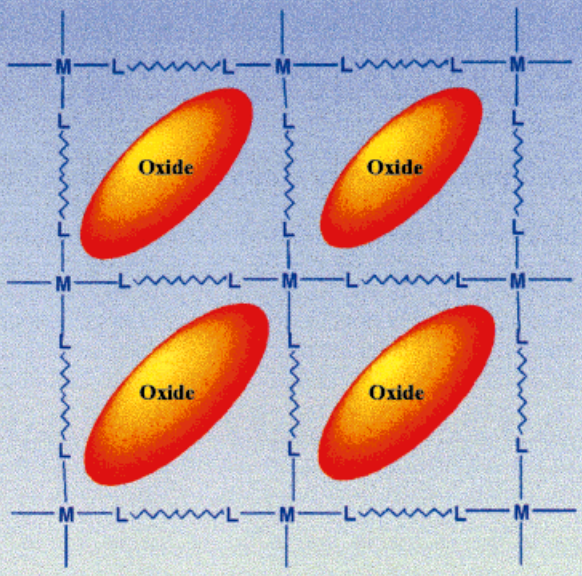

b)

Ligand geometry and metal coordination preferences may provide a) one-, b) two-, or c) three-dimensional polymeric coordination complex cations as scaffolding for the manipulation of metal oxide substructures.

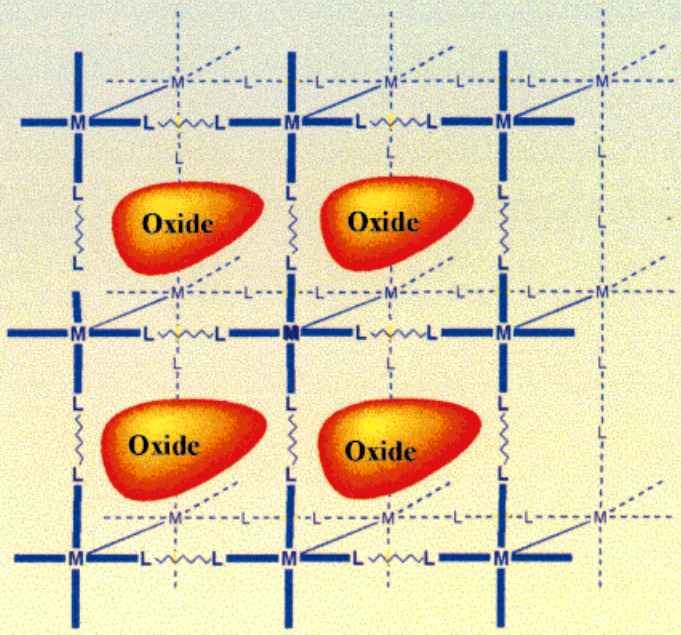

c)

ANGEWANDTE CHEMIE

Organic – Inorganic Hybrid Materials: From "Simple" Coordination Polymers to Organodiamine-Templated Molybdenum Oxides

Pamela J. Hagrman, Douglas Hagrman, and Jon Zubieta*

Dedicated to Professor Achim Müller on the occasion of his 60th birthday

The vast range of solid-state properties exhibited by the oxides is a result of their diversity of chemical composition and structure type. However, while many naturally occurring oxides and minerals possess complex crystal structures, the majority are of simple composition and have highly symmetrical structures with rather small unit cells. Most silicates, important ores, gems, and many rocks and soils are examples of these materials. Although such simple oxides can possess unique and specific properties—such as piezoelectricity, ferromagnetism, or catalytic activity—as a general rule there is a correlation between the complexity of the structure of a material and its functionality. One approach to the design of novel oxide materials mimics nature's use of organic molecules to modify inorganic microstructures. In this instance, the inorganic oxide contributes to the increased functionality by assimilation as one component in a hierarchical structure where there is a synergistic interaction between organic material and the inorganic oxide. Synthetic studies of materials that possess such an interface, coupled with the acquisition of the appropriate structural information, should contribute to the development of an increased understanding of methods to control the structure – property relationships within these hybrid materials. While the organic component may assume a variety of structural or functional roles in the design of novel oxide-based composite materials, the extensive contemporary interest in framework solids suggested their use as ligands in a polymeric coordination complex cation which provides not only charge compensation for the anionic oxide substructure but also a rigid framework for entraining and, to a degree, for controlling the surface of the growing oxide microstructure. These framework solids are particularly attractive from several perspectives: 1) They are accessible by self-assembly under exceedingly mild conditions which allows retention of the structural integrity of the starting materials and the isolation of kinetic, rather than exclusively thermodynamic, products; 2) they possess a remarkable chemical and structural diversity; and 3) the numerous examples described in recent years demonstrate that some control is achievable in defining their architectures. Consequently, by appropriate selection of ligand types and through exploitation of the coordination preferences of the metal, one-, two-, or three-dimensional coordination complex cations may be constructed to provide a scaffolding for the entraining of the oxide substructure. Application of this strategy to the study of the molybdenum oxide/organodiamine – metal complex interface has produced a wealth of organic – inorganic hybrid materials of the MOXI family. These materials demonstrate not only the complexity of the organic – inorganic synthetic interface in the construction of such materials but also provide evidence of a powerful tool for the low-temperature synthesis of new materials endowed with structural complexity.

Keywords: coordination polymers · crystal engineering · hydrothermal synthesis · metal oxides · molybdenum

One of the continuing scandals in the physical sciences is that it remains in general impossible to predict the structures of even the simplest crystalline solids from a knowledge of their chemical compositions.

John Maddox

But in two or three dimensions, it's a synthetic wasteland. The methodology for exercising control so that one can make unstable but persistent extended structures on demand is nearly absent. Or to put it in a positive way—this is a certain growth point of the chemistry of the future.

Roald Hoffmann

[*] Prof. J. Zubieta, P. J. Hagrman, D. Hagrman
Department of Chemistry, Syracuse University
Syracuse, New York 13244 (USA)
Fax: (+1) 315-443-4070
E-mail: jazubiet@mailbox.syr.edu

1. Introduction

Oxygen is not only the most abundant terrestrial element, it is also highly reactive; consequently, oxides exist for most of

  1433-7851/99/3818-2639 $ 17.50+.50/0

the elements with the exceptions of radon and the lighter noble gases,[1] and inorganic oxides are ubiquitous in the geosphere and the biosphere.[2] In addition to the hydrogen oxide that forms the basis of life, oxygen is found in combination with silicon and aluminum in the form of complex aluminosilicates which make up the vast proportion of igneous rocks.[3] Not only are most ores and gems examples of solid-state oxides, but bones, shells, teeth, spicules, and petrified wood represent structurally complex oxides fashioned through biomineralization.[4, 5]

The intense contemporary interest in solid-state oxides reflects their properties, which endow these materials with applications from heavy construction to microelectronic circuitry. The huge range of solid-state properties summarized in Table 1 is a result of the diversity of chemical compositions and structure type exhibited by the inorganic oxides.[6]

However, while many naturally occurring oxides and minerals and even synthetic oxides possess complex crystal structures, the majority are of relatively simple composition and exhibit highly symmetrical structures with rather small unit cells. Although such simple oxides possess undeniably useful properties, there exists, in general, a correlation between the complexity of the structure of a material and the functionality which it displays.[30] Thus, many of the remarkable materials fashioned by nature contain mixtures of inorganic oxides coexisting with organic molecules. For example, the calcite or aragonite forms of calcium carbonate can be specifically nucleated in molluscs by molecular manipulation induced by small amounts of an organic component.[31] It is now apparent that organic components can dramatically influence the microstructures of inorganic oxides, thus providing a method for the design of novel materials.

1.1. Organic – Inorganic Hybrid Materials

The control of inorganic structure by an organic component reveals an interactive structural hierarchy in materials.[32] In such materials, the inorganic oxide contributes to the increased complexity and hence functionality through incorporation as one component in a multilevel-structured material where there is a synergistic interaction between the organic and inorganic components.[30] Since this interaction within these organic – inorganic hybrid materials derives from the nature of the interface between the organic component and the inorganic oxide, synthetic and structural studies of materials that exhibit such an interface will contribute to the development of structure – function relationships for these hybrid materials.

There are now four major classes of materials in which organic components exert a significant structural role in the control of the inorganic oxide microstructure. These materials are zeolites,[32, 33] mesoporous oxides of the MCM-41 class,[34] biomineralized materials,[2, 5, 35] and microporous octahedral – tetrahedral or square-pyramidal – tetrahedral framework transition metal phosphates (TMPO) with entrained organic cations.[36, 37] While the dramatically expanding field of


J. Zubieta


P. Hagrman


D. Hagrman

Jon Zubieta, born and raised in New York City, received his B.S. degree from Fordham University in 1966 and his Ph.D. from Columbia University in 1971. After postdoctoral work at the University of Sussex (UK), he joined the chemistry faculty at the State University of New York at Albany. In 1990 he moved to Syracuse University. His research interests include the design and structural characterization of metal oxide clusters and solids, applications of the coordination chemistry of technetium and rhenium to radiopharmaceuticals, and the development of drug delivery systems based on the organic – inorganic oxide interface.

Pamela Hagrman, born in Syracuse, New York, received her B.S. degree from the State University of New York at Buffalo in 1994. She is currently pursuing her Ph.D. degree in inorganic chemistry at Syracuse University. Her research focuses on the applications of the techniques of solvatothermal synthesis to the isolation of organically templated metal oxide materials.

Douglas Hagrman, born in Salt Lake City, Utah, and raised in Idaho Falls, Idaho, received his B.S. degree in Chemical Engineering from the University of Nebraska-Lincoln. He is currently pursuing a Ph.D. in inorganic chemistry at Syracuse University, where he has been honored with the Outstanding Teaching Assistant Award and the William D. Johnson Award for teaching excellence. He is the recipient of the ACA Pauling Prize for the outstanding poster presentation at the ACA meeting in Buffalo in 1999. His research has focused on the hydrothermal synthesis and structural characterization of new oxide materials. His future plans include the elaboration of new synthetic methods in solid-state chemistry, including combinatorial synthesis and high throughput screens for property assessment.

Table 1. Some examples and applications of inorganic oxides

Class	Examples	Application	Ref.
magnetic oxides	CrO_2	magnetic tapes	[7]
	ferrites of type $Zn_{x+2}Fe_{1-x}[Mn_{1-x}Fe_x]O_4$	transformer cores	[8]
	(Mn, Mg) spinels	computer memories	[8]
oxide sensors	$BaTiO_3$	temperature sensor	[7]
	$PbZrO_3$	acoustical pickup, piezo speakers	[10]
phosphors	Mn-doped Zn_2SiO_4	green phosphor for oscilloscope tubes	[11]
	Eu-doped Y_2O_3	red phosphor	
electronic materials	$BaTiO_3$	surge protector	[9]
	ZnO	high-resistance semiconductor	[12]
	$YBa_2Cu_3O_{7-x}$	high-temperature superconductor	[13]
pigments	Fe_3O_4	black pigment	[8]
	Fe_2O_3	red pigment	[8]
ceramics	Al_2O_3	fefractory for fire brick	[14]
	$PbZr_{1-x}Ti_xO_3$	ferroelectrics	[15]
optical materials	$LiNbO_3$, $KTi(PO_4)$	harmonic generators, frequency mixers	[16]
catalysts	$(VO)_2P_2O_7$	selective oxidation of *n*-butane to maleic anhydride	[17]
	$Bi_2Mo_2O_9$	selective oxidation of propene to acrylonitrile	[18]
	V_2O_5/TiO_2	selective oxidation of naphthalene to phthalic anhydride	[19]
	Cr_2O_3/Al_2O_3	polymerization of alkenes	[20]
	$Cu_2Al_6B_4O_{17}$	oxidative dehydrogenation	[20]
	SiO_2/MgO_3	conversion of ethene into butadiene	[21]
	SO_4^{2-}/ZrO_2	cracking, isomerization, alkylation	[22]
ion exchange	NASICON, $Na_{1+x}Zr_2Si_xP_{3-x}O_{12}$	cation exchange, fast-ion conductor	[23]
	$Mg_6Al_2(OH)_{16}CO_3 \cdot 4H_2O$	anion exchange	[23]
	zeolites, $M_{x/m}^{m+}[Si_{1-x}Al_xO_2] \cdot H_2O$	detergents	[24]
molecular sieves	zeolites	separating agents	[25, 26]
catalysts and molecular sieves	zeolites and ALPOs, $[AlPO_4] \cdot y\,R \cdot n\,H_2O$, faujasite	catalytic cracking	[27]
	ALPO-5	hydrocracking	[28]
	silicalite	xylene isomerization	[29]
biomaterials	organoapatites	artificial bone	[30]

biomineralization will not be discussed in this review, two observations are relevant: 1) Complex inorganic materials may be prepared across a range of length scales by coding of precipitation reactions;[38] 2) biologically-based organic materials interact with inorganic oxides primarily through O-H $\cdots$ O and N-H $\cdots$ O hydrogen-bonding interactions.[39]

The pioneering work of Barrer on the synthetic zeolites[40] represents the first systematic development of materials in which organic molecules were used to influence the growth of inorganic oxides. The incorporation of organic molecules, primarily amines and ammonium salts, into aluminosilicate frameworks has provided a dramatic expansion of this technologically important class of materials. The organic cation serves not only to provide charge compensation required by the substitution of Al^{3+} for Si^{4+} within the zeolite framework, but, by virtue of its size, shape, and polarity, also directs the crystallization of the silicate aggregates into the zeolitic framework. The basic conditions required for dissolution of SiO_2 dictate that quaternary ammonium salts be used as charge-compensating cations. Consequently, the template–framework interaction is primarily of the van der Waals type.

The rapidly expanding field of mesoporous oxides derives from the pioneering work on MCM-41 materials at Mobil Oil.[34, 41] These hybrid materials are prepared by polymerization of soluble silica polyanions around a cationic template with a long hydrophobic tail. Since structural information from the amphiphilic organic template is imprinted on the oxide structure derived from silicate polymerization, variations in size, shape, and charge of the organic surfactant and in concentration, pH value, temperature, and shear forces allow the realization of numerous morphologies which contain periodic arrays with adjustable channel diameters in the range of 16 to 100 Å, after removal of the organic components. Such large variable pore sizes render the materials of this class of interest as size- and shape-selective heterogeneous catalysts and as hosts for nanometer-scale electronic and optical devices.

The first example of a non-silicate, open-framework oxide with entrained organic cations, $(Me_4N)(H_3O)[Mo_4O_4(PO_4)] \cdot x\,H_2O$, was reported in 1989[42] and shown to contain an octahedral–tetrahedral framework constructed from Mo_4 oxoclusters connected by PO_4 tetrahedra into a three-dimensional covalent framework. Most significantly, the organic counterions could be thermally removed from the material to produce a microporous oxomolybdenum phosphate framework. Subsequently, not only were numerous MoPO materials synthesized, but a large and ever-expanding family of organically templated oxovanadium phosphate and phosphonate frameworks was described.[36, 37, 43]

1.2. Design in Metal Oxide Synthesis

The common feature distilled from the four classes of inorganic oxide materials described above is the influence of the organic component in controlling the nucleation and growth of the inorganic oxide. Organic components alter the inorganic oxide microstructure. There is a synergism between the organic and inorganic components which allows the structural information from the organic molecule to imprint

onto the inorganic framework. Implicit in the evolution of these organic–inorganic hybrid materials is a shift from the thermodynamic to the kinetic domain, such that equilibrium phases are replaced by structurally more complex metastable phases. However, traditional solid-state syntheses produce thermodynamic products, often by solid–solid interactions at temperatures of about 1000 °C, conditions which will not retain the structural elements of the organic component. Consequently, low-temperature techniques must be adopted in an approach that resembles small-molecule chemistry. Hydrothermal synthesis has been found to provide a powerful technique for the preparation of organic–inorganic hybrid materials with retention of the structural elements of the reactants in the final products. Consequently, the general approach adopted for the preparation of new inorganic oxides employs organic molecules at low temperature to modify or control the surface of growing oxide crystals in a hydrothermal medium. Following these general guidelines, a fifth major class of organic–inorganic hybrid materials has been identified: dipodal organonitrogen-templated molybdenum oxides.

2. Synthesis

2.1. Hydrothermal Chemistry

While well established for the synthesis of zeolites, the hydrothermal method has more recently been adapted to the preparation of a wide variety of metastable materials, including the TMPO group and even complex polyoxoalkoxometalates.[44] Hydrothermal reactions, typically carried out in the temperature range 120–260 °C under autogenous pressure, exploit the self-assembly of the product from soluble precursors.[45] The reduced viscosity of water under these conditions enhances the diffusion processes so that solvent extraction of solids and crystal growth from solution are favored.[46] Since differential solubility problems are minimized, a variety of simple precursors may be introduced, as well as a number of organic and/or inorganic structure-directing agents, from which those of appropriate size and shape may be selected for efficient crystal packing during the crystallization process. Under such nonequilibrium crystallization conditions, metastable kinetic phases rather than the thermodynamic phase are most likely to be isolated.[47] While several pathways, including the one that results in the most stable phase, are available in such nonequilibrium mixtures, the kinetically favored structural evolution results from the smallest perturbations of atomic positions. Consequently, nucleation of a metastable phase may be favored.

The synthetic conditions employed to prepare the organodiamine molybdenum oxides (MOXI) of this study are relatively simple. An aqueous solution of the organic template, the molybdenum source, and in certain cases a heterometal source are heated to 120–220 °C for 12–72 h. In the majority of cases, crystals form at the reaction temperature and not upon cooling to room temperature. Since X-ray crystallography is the primary characterization technique for these materials, suitable crystals are a prerequisite for the study.

It is also apparent that small changes in one or more of the reaction variables of the vast hydrothermal parameter space—such as time, temperature, pH value, stoichiometry, template identity, and duration—can have a profound influence on the reaction outcome. Consequently, quantitative predictions of reaction products are generally not possible, and one is often guided by analogy to previous results or by knowledge of the geometric constraints associated with a ligand type or of the coordination requirements of the heterometal.

2.2. Role of the Organic Component

The structure-directing organic molecules employed in the synthesis of the MOXI class of oxides are the dipodal organoamines, of the general types illustrated below (see Table 2 for abbreviations of the organic molecules). Such organoamines may adopt a variety of roles in these organic–inorganic hybrid materials: 1) charge-compensating cations, 2) ligands bonded directly to a molybdenum site of the molybdenum oxide skeletal backbone, and 3) ligands bonded to the heterometal site.

As charge-compensating cations, the organodiamines function in a role reminiscent of that adopted by the organic components of zeolites, mesoporous oxides, and TMPOs. The common features that link these structurally diverse materials are the critical phenomena which also influence biomineralization, namely, hydrogen-bonding and hydrophobic–hydrophilic interactions. As shown in Figure 1, the structure of $[H_3N(CH_2)_3NH_3][(VO)_3(OH)_2(H_2O)_2(PO_4)_2]$[48] reveals an open-framework vanadium phosphate with the organodiammonium cations occupying well-defined channels. The important structure-directing role of the entrained polar ammonium

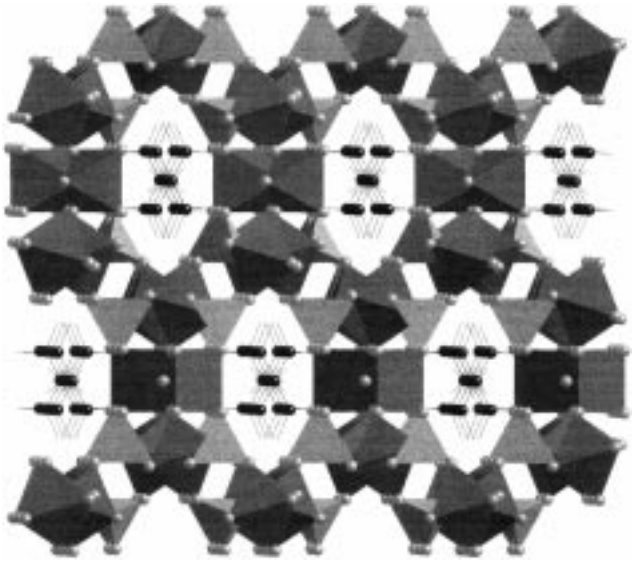

Figure 1. A polyhedral representation of the V-P-O framework of $[H_3N(CH_2)_3NH_3][(VO)_3(OH)_2(H_2O)_2(PO_4)_2]$ down the crystallographic *a* axis. The channels are occupied by the templating $[H_3N(CH_2)_3NH_3]^{2+}$ cations, shown in ball-and-stick representation.

cation manifests itself in strong, geometrically specific hydrogen bonding between the NH groups of the cation and the oxygen atoms of the framework. It is likely that such multipoint hydrogen bonding, which constitutes the strongest interaction aside from the covalent bonds of the oxide framework, may render the material the kinetically least soluble species present in the hydrothermal reaction medium. The influences of hydrophobic–hydrophilic interactions are most evident in the structures of the vanadium organophosphonates, such as $[(C_2H_5)_4N]_2[(VO)_6(OH)_2(H_2O)_2(O_3PC_2H_5)_6]$[49] (Figure 2). Two characteristics which influence structure are the association of organic groups from neighboring phosphonate units and the incorporation of hydrophobic $(C_2H_5)_4N^+$ cations. Consequently, two-dimensional materials are favored to reduce the interactions of the less polar organic moiety with the polar oxide network.

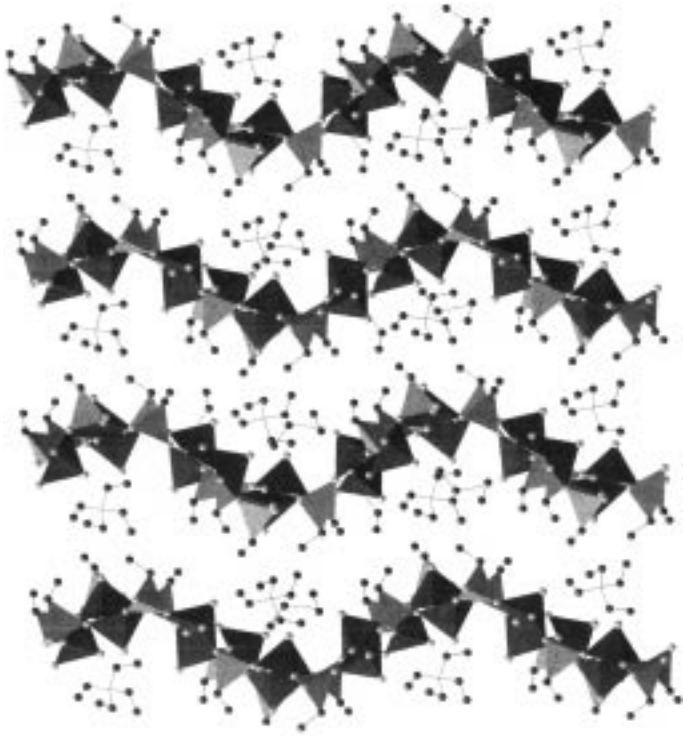

Figure 2. A polyhedral representation of the undulating V-P-O networks of $[(C_2H_5)_4N]_2[(VO)_6(OH)_2(H_2O)_2(O_3PC_2H_5)_6]$, viewed along the *b* axis. The ethyl groups of the organophosphonate ligands project into the interlamellar regions above and below each layer. The organic cations occupy the interlamellar region, and divide the structure into polar and nonpolar domains.

Of course, organoamines may function as ligands in a variety of ligating modes. The material $[(VO)(PO_4)(H_2NCH_2CH_2NH_3)]$[50] (Figure 3) serves as an unusual example of an organic component that serves both as a monodentate ligand through an amine terminus and as a cation through protonation of the pendant nitrogen site. Strong multipoint hydrogen bonding between strands is also apparent in this structure.

In certain cases, it has proved advantageous to introduce a heterometallic component, either to provide charge compensation or as part of the inorganic bimetallic oxide framework itself. The structure of $[Zn(H_2NCH_2CH_2NH_2)_2][V_6O_{14}]$[51]

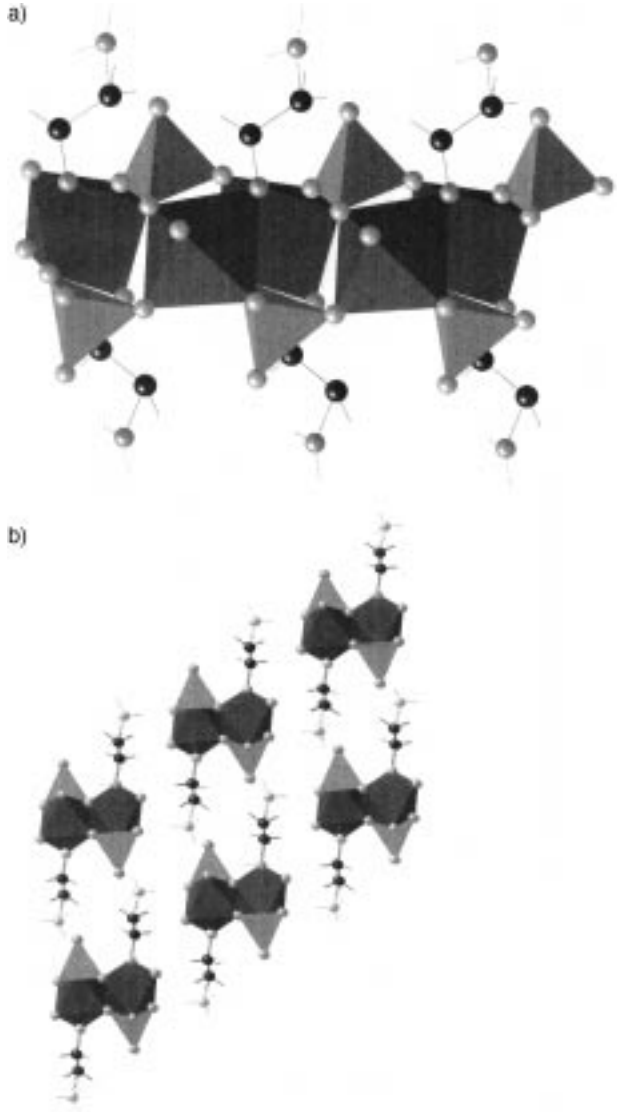

Figure 3. a) A polyhedral representation of the one-dimensional chains of $[(VO)(PO_4)(H_2NCH_2CH_2NH_3)]$, to illustrate the role of the $\{H_2NCH_2CH_2NH_3\}^+$ group as ligand and charge-compensating cation. b) A view of the chain packing along the *b* axis and down the chain axes, showing the outward projection of the $\{H_2NCH_2CH_2NH_3\}^+$ groups which provides effective hydrogen bonding between adjacent chains.

(Figure 4) is an example of a simple coordination complex cation $[Zn(en)_2]^{2+}$ entrained between vanadium oxide layers, which functions as an organic–inorganic counterpart of organoammonium cations in simple structural types. In contrast, the structure of $[\{Zn(4,4'\text{-bpy})_2\}_2V_6O_{17}]$[51] (Figure 5) illustrates the incorporation of the heterometallic complex as a covalently attached unit of the metal oxide framework itself. These latter structures provided the impetus to investigate the role both of organodiamine groups and of organodiamine-ligated heterometals as ligands, counterions, space-filling units, and constituents of the metal oxide framework in molybdenum oxide phases.

It was also evident that ditopic organoamine ligands presented an unusual structural versatility. Such versatility has been exploited in recent years in the development of a vast structural chemistry based on cationic rods, square grids,

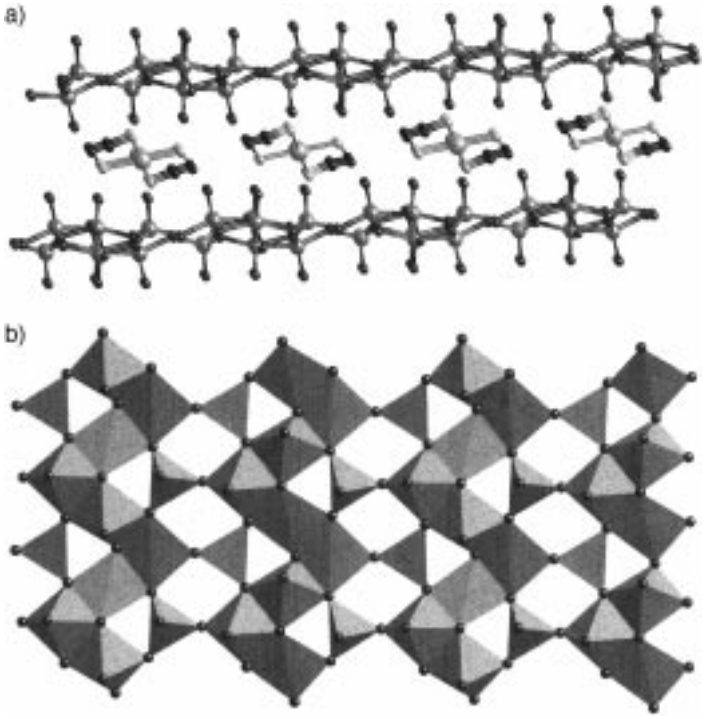

Figure 4. a) A view of the complex layer structure of $[Zn(H_2NCH_2CH_2NH_2)_2][V_6O_{14}]$, to show the disposition of $\{Zn(en)_2\}^{2+}$ groups in the interlamellar region between the $\{V_6O_{14}\}^{2-}$ layers. b) A polyhedral representation of the $\{V_6O_{14}\}^{2-}$ layer, showing the chains of edge-sharing V^{IV} square pyramids and bridging V^{V} tetrahedra.

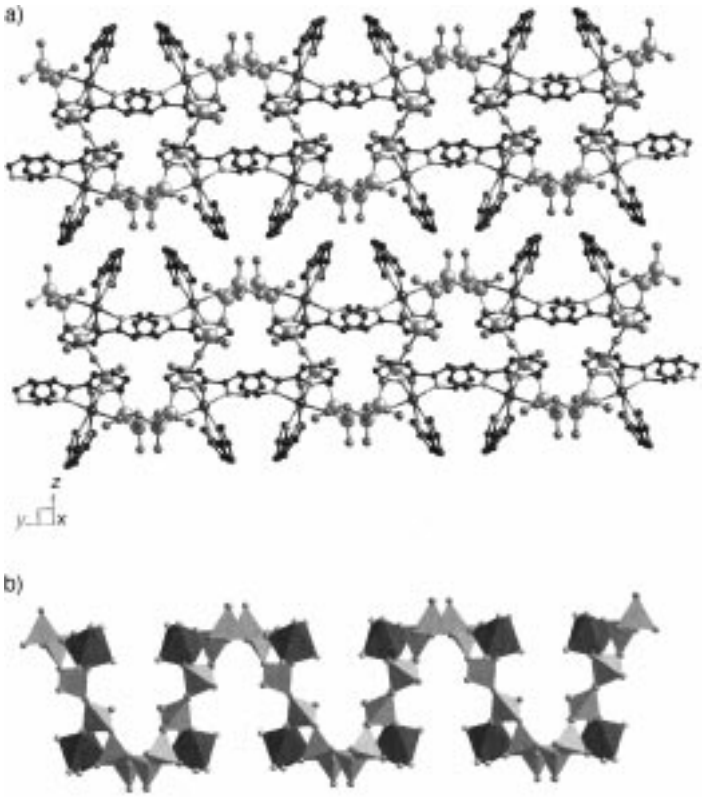

Figure 5. a) A view perpendicular to the vanadium oxide layers of the structure of $[\{Zn(4,4'\text{-bpy})_2\}_2V_6O_{17}]$. b) A polyhedral representation of the corner-sharing $\{VO_4\}$ tetrahedra (light polyhedra) and $\{ZnO_2N_4\}$ octahedra (dark polyhedra), to show the cavities occupied by the 4,4′-bpy ligands.

honeycomb grids, adamantoid frameworks, and interpenetrating networks.[52, 188] Such assemblies seemed to offer novel coordination complex polymers and structural units for incorporation into molybdenum oxide frameworks to generate a new class of organic–heterometallic oxides. The structural diversity of these cationic building blocks is sufficiently complex and fascinating to merit a digression into their crystal architectures, a topic which has not been reviewed despite intense contemporary activity.

3. Structural Chemistry of Organodiamine Coordination Polymers

Crystal engineering of supramolecular architectures is of considerable contemporary interest by virtue of the potential applications of such materials to host–guest chemistry,[53] catalysis,[54] and the evolution of optical, magnetic and electronic properties.[55, 56] Two types of interactions have been exploited in the construction of such supramolecular materials: 1) coordinate covalent bonds connecting metal centers and appropriate ligand types,[57] and 2) hydrogen bonds in organic solids.[58, 59] In the specific case of coordination polymers, the expectation is that the geometry of the metal will be propagated through the bridging ligands. The approach to the design of such coordination polymers has been to exploit organic ligands which, through their geometries and coordination preferences, impose a specific network topology.[60] While organic building blocks of various connectivities and geometries have been used in the preparation of coordination polymers,[57] this discussion will be limited to two- and three-connected units that employ organoamine donors. Although supramolecular cyanometalate systems possess an extensive and well-developed structural chemistry,[61] such materials have yet to be employed in the preparation of molybdenum oxide phases; consequently, their chemistry will not be discussed here.

As summarized in Table 2, the structural versatility of even this limited subclass of coordination polymers is quite remarkable. This observation is less surprising if it is noted that the structural range reflects both metal and ligand properties: the oxidation state and coordination predisposition of the metal; 2) the ligand geometry, including relative orientation of the donor groups and the spacing between donor groups; and 3) the influence of the coordinating anions or ancillary ligands.

From the perspective of structural modification of molybdenum oxide phases, the cationic nature of the metal–organodiamine polymer subunits provides the significant unifying theme for the variety of coordination polymer structures presented in the subsequent sections. The coordination polymer structures are characterized by void volumes occupied by charge-compensating anions. Molybdenum oxides, whether present as polyanions, chains, two-dimensional networks, or three-dimensional frameworks, are in general negatively charged species. From this viewpoint, the cationic coordination polymers as subunits of molybdenum oxide phases can serve as charge-compensating and space-filling units, or they may bond directly to the molybdenum oxide

Table 2. Selected structural information for polymer structures formed from metal cations and ditopic nitrogen-donor ligands and related ligand types.[a]

Compound	Metal–ligand skeletal structure	Metal coordination geometry	Structural description	Figure	Ref.
A. 4,4′-bipyridine as bridge					
$[Cu(4,4'\text{-bpy})(BF_4)_2(H_2O)_2]\cdot(4,4'\text{-bpy})$	1D	$\{CuN_2O_2F_2\}$	linear $[Cu(4,4'\text{-bpy})(BF_4)_2(H_2O)_2]$ chains linked by hydrogen bonding of H_2O protons to uncoordinated 4,4′-bpy groups to form 2D sheets	6	[63]
$[Mn(4,4'\text{-bpy})(NCS)_2(H_2O)_2]\cdot(4,4'\text{-bpy})$	1D	$\{MnN_4O_2\}$	linear $\{Mn(4,4'\text{-bpy})(NCS)_2(H_2O)_2\}$ chains linked by hydrogen bonding of H_2O protons to uncoordinated 4,4′-bpy groups to form a 2D network	–	[64]
$[Cu(4,4'\text{-bpy})(ClO_4)_2(H_2O)_2]\cdot(4,4'\text{-bpy})$	1D	$\{CuN_2O_4\}$	linear $\{Cu(4,4'\text{-bpy})(ClO_4)_2(H_2O)_2\}$ chains linked by hydrogen bonding of H_2O protons to pendant perchlorate oxygen atoms of a neighboring strand to form a 2D network	–	[65]
$[Zn(4,4'\text{-bpy})(H_2O)_4](NO_3)_2\cdot(4,4'\text{-bpy})$	1D	$\{ZnN_2O_4\}$	linear $\{Zn(4,4'\text{-bpy})(H_2O)_4\}$ chains linked by hydrogen bonding to the uncoordinated 4,4′-bpy into 2D sheets	–	[66]
$[Zn(4,4'\text{-bpy})(H_2O)_4](NO_3)_2\cdot 2(4,4'\text{bpy})\cdot 3H_2O$	1D	$\{ZnN_2O_4\}$	linear $\{Zn(4,4'\text{-bpy})(H_2O)_4\}$ chains linked by hydrogen bonding to pairs of uncoordinated 4,4′-bpy into 2D sheets	–	[66]
$[Zn(4,4'\text{-bpy})(H_2O)_4](CF_3SO_3)_2$	1D	$\{ZnN_2O_4\}$	linear $\{Zn(4,4'\text{-bpy})(H_2O)_4\}$ chains linked by hydrogen bonding to pairs of uncoordinated 4,4′-bpy into 2D sheets	–	[66]
$[Fe(4,4'\text{-bpy})(H_2O)_3(ClO_4)](ClO_4)\cdot 1.5(4,4'\text{-bpy})\cdot H_2O$	1D	$\{FeN_2O_4\}$	linear $\{Fe(4,4'\text{-bpy})(ClO_4)(H_2O)_3\}^+$ chains linked by hydrogen bonding to alternating single and paired uncoordinated 4,4′-bpy groups into 2D sheets	7	[66]
$[Cu(4,4'\text{-bpy})(MeCN)_2](BF_4)$	1D	$\{CuN_4\}$	zigzag $\{Cu(4,4'\text{-bpy})(MeCN)_2\}$ chains	8	[67]
$[Co(4,4'\text{-bpy})_{1.5}(NO_3)_2]\cdot MeCN$	1D	$\{CoN_3O_4\}$	linear $\{Co(4,4'\text{-bpy})(NO_3)_2\}$ chains cross-linked by 4,4′-bpy groups into a ladder structure	9	[68]
$[Ni(4,4'\text{-bpy})_{2.5}(H_2O)_2](ClO_4)_2\cdot 1.5(4,4'\text{-bpy})\cdot 2H_2O$	1D	$\{NiN_4O_2\}$	linear $\{Ni(4,4'\text{-bpy})(H_2O)_2\}^{2+}$ chains cross-linked by 4,4′-bpy groups, with each Ni site additionally bonded to a monodentate, pendant 4,4′-bpy to form a 1D "railroad" assembly; π stacking of pendant groups results in a 2D sheet	10	[69]
$[MX_2(4,4'\text{-bpy})]$ (M = Ni, Cu; X = Cl, Br)	1D	$\{MX_4N_2\}$	mutually perpendicular $\{M(4,4'\text{-bpy})\}^{2+}$ and $\{MX_2\}$ chains linked into a 2D network	11	[70]
$[Ag(4,4'\text{-bpy})](NO_3)$	1D	$\{AgN_2Ag\}$, T-shaped	$\{Ag(4,4'\text{-bpy})\}^+$ linear chains linked through Ag–Ag bonds into a 3D structure; threefold interpenetration	12	[71]
$[Cu(4,4'\text{-bpy})(H_2O)_3(SO_4)]\cdot 2H_2O$ (**CUSO-1**)	1D	$\{CuO_4N_2\}$	linear $\{Cu(4,4'\text{-bpy})(H_2O)_3(SO_4)\}$ chains, stacked to produce a hexagonal motif	46	[72]
$[Cu(dmp)(4,4'\text{-bpy})](BF_4)\cdot MeCN$	1D	$\{CuN_4\}$	zigzag chains of tetrahedral $\{CuN_4\}$ sites linked by 4,4′-bpy tethers	–	[73]
$[Cd(4,4'\text{-bpy})_2(NO_3)_2]\cdot 2C_6H_4Br_2$	2D	$\{CdN_4O_2\}$	stacked cationic square-grid networks with no interpenetration	13	[74]
$[Zn(4,4'\text{-bpy})_2(H_2O)_2](SiF_6)$	2D	$\{ZnN_4O_2\}$	stacked cationic square-grid networks with no interpenetration	–	[75]
$[Zn(4,4'\text{-bpy})_2](SiF_6)\cdot DMF$	2D	$\{ZnN_4F_2\}$	sheets of $\{Zn(4,4'\text{-bpy})_2\}$ square grids bridged through SiF_6^{2-} groups into a 3D framework octahedral polymer with no interpenetration	–	[76]
$[Cu_2(C_3H_2O_4)_2(H_2O)(4,4'\text{-bpy})]\cdot H_2O$	2D	$\{CuNO_4\}$	$\{Cu_4(C_3H_2O_4)\}$ squares linked through 4,4′-bpy groups into larger squares forming a 2D network, no interpenetration	14	[77]
$[M_2(4,4'\text{-bpy})_3(NO_3)_4]\cdot xH_2O$, M = Co, Ni, Zn	2D	$\{MN_3O_4\}$, pentagonal bipyramidal	$\{M(4,4'\text{-bpy})(NO_3)_2\}$ chains linked by 4,4′-bpy groups into double sheets; the sheets assemble into a tongue-and-groove 3D structure	15	[78]
$[Cu(4,4'\text{-bpy})Cl]$	2D	$\{CuN_2Cl_2\}$	$\{Cu_2Cl_2\}$ dimers linked through 4,4′-bpy groups into 2D sheets with large hexagonal grid pattern; twofold interpenetration of sheet arrays	16	[79]
$[Cu(4,4'\text{-bpy})_2(H_2O)_2](ClO_4)_4\cdot(4,4'\text{-}H_2\text{bpy})$	2D	$\{CuN_4O_2\}$	2D square-grid network	–	[80]

Table 2. (Continued)

Compound	Metal–ligand skeletal structure	Metal coordination geometry	Structural description	Figure	Ref.
$[M(4,4'\text{-bpy})_2(H_2O)_2](ClO_4)_2 \cdot (2,4'\text{-bpy})_2 \cdot H_2O$, M = Zn, Cd	2D	$\{MN_4O_2\}$	2D square-grid network	–	[80]
$[Ag(4,4'\text{-bpy})_2](CF_3SO_3)$	3D	$\{AgN_4\}$	diamondoid framework based on adamantoid cages; four independent diamondoid frameworks interpenetrate	17	[81]
$[Cu(4,4'\text{-bpy})_2](PF_6)$	3D	$\{CuN_4\}$	diamondoid framework based on adamantoid cages; four independent diamondoid frameworks interpenetrate	–	[82]
$[Cu(3,3'\text{-bpy})_2]X$, $X = BF_4^-$, PF_6^-	3D	$\{CuN_4\}$	diamondoid framework; two independent frameworks interpenetrate	–	[83]
$[Cu(4,4'\text{-bpy})_{1.5}](NO_3)(H_2O)_{1.25}$	3D	$\{CuN_3\}$, trigonal planar	six porous and identical interpenetrating 3D frameworks	18	[84]
B. tethered bipyridine bridges (py-X-py) and related types.					
$[Cu_2(bpbd)_3(MeCN)_2](PF_6)_2$	1D	$\{CuN_4\}$, one CH_3CN nitrogen atom	{Cu(bpbd)(MeCN)} undulating chains cross-linked by dpbd ligands into a ladder; each ladder is interpenetrated by four additional ladders into a polycatenated 2D sheet	19	[85]
$[Cd(dpb)_{1.5}(NO_3)_2]$	1D	$\{CdN_3O_4\}$	$\{Cd(dpb)(NO_3)_2\}$ linear chains cross-linked by dpb groups into a ladder; each ring is interpenetrated by rings of four different ladders	20	[86]
$[Ag(bbp)](CF_3SO_3) \cdot EtOH$	1D	$\{AgN_2\}$	1D sinusoidal chains	22	[87]
$[Ag(bbp)](CF_3SO_3)$	1D	$\{AgN_2\}$, weak additional Ag–Ag interaction to produce T-shaped site	1D helical chains; helices pair into double chains	22	[87]
$[Ag_2(bbp)_4](CF_3SO_3)_2 \cdot bbp$	1D	$\{AgN_4\}$	$\{Ag_2(bbp)_2\}$ 24-membered rings linked into tubular arrays	22	[87]
$[Cu(dmp)(dpe)](BF_4)$	1D	$\{CuN_4\}$	zigzag chains of tetrahedral $\{CuN_4\}$ sites linked by dpe tethers	–	[73]
α-$[Co(dpe)_{1.5}(NO_3)_2]$	1D	$\{CoN_3O_4\}$, pentagonal bipyramidal	$\{Co(dpe)(NO_3)_2\}$ chains linked by dpe into a molecular bilayer	23	[88]
$[Cd(dpe)_{1.5}(NO_3)_2]$	1D	$\{CdN_3O_4\}$	isostructural with α-$[Co(dpe)_{1.5}(NO_3)_2]$	–	[89]
γ-$[Co(dpe)_{1.5}(NO_3)_2]$	1D	$\{CoN_3O_4\}$	$\{Co(dpe)(NO_3)_2\}$ linear chains cross-linked by *anti*-dpe ligands into a ladder	–	[88]
$[Cu(bpac)](NO_3)_2 \cdot 0.5\,EtOH$	1D	$\{CuN_2O_4\}$, O donors from two bridging nitrate groups and one terminal bidentate nitrate group	{Cu(bpac)} linear chains linked by bridging nitrate ligands into a ladder	–	[90]
$[Ag(pytz)(NO_3)]$	1D	$\{AgN_2O_2\}$ distorted square planar with two long Ag···O interactions	{Ag(pytz)} chains linked through $(NO_3)^-$ bridges into a 3D helical array	32	[91]
$[Ag_2(bpy\text{-}4pz)_2](PF_6)_2$	1D	$\{AgN_3S\}$	binuclear $\{Ag_2(bpy\text{-}4pz)_2\}$ boxes linked into a 1D chain	25	[92]
$[Cu_4(bppy)(CH_3CO_2)_8]$	1D	$\{CuO_6\}$ and $\{CuN_2O_3\}$	binuclear $\{Cu_2(CH_3CO_2)_2\}$ units and linked by bppy groups into 1D $\{CuN_2O_3\}$ chains which are in turn linked through acetate bridges for $\{Cu_2(CH_3CO_2)_4\}$ units to form a 2D sheet	26	[93]
$[Co(py_2S)(NCS)_2] \cdot 2H_2O$	1D	$\{CoN_4N'_2\}$ four pyridyl donors, two nitrogen donors from NCS^-	double-stranded 1D chain	–	[94]
$[Cu(bpe)_2][Cu(bpe)(H_2O)_2(SO_4)_2] \cdot 2H_2O$ (**CUSO-2**)	1D and 2D	$\{CuN_2O_4\}$ and $\{CuN_4\}$	2D sheets of $\{Cu(bpe)_2\}^{2+}$ square grids; two independent sets of sheets interpenetrate; 1D $\{Cu(bpe)(H_2O)_2(SO_4)_2\}^{2-}$ chains are interwoven between the sheets	47	[72]
$[Cu(bpe)(H_2O)(SO_4)]$ (**CUSO-3**)	1D	$\{CuN_2O_3\}$, square pyramidal	1D $\{Cu(bpe)\}^{2+}$ chains linked by SO_4^{2-} groups into a 3D covalent framework	48	[72]
$[Ag(pytz)(MeCN)](PF_6)$	1D	$\{AgN_3\}$ two pyridine donors, one methyl cyanide nitrogen donor	linear {Ag(pytz)} chains linked into double chains through long Ag···Ag interactions	33	[91]

Table 2. (Continued)

Compound	Metal–ligand skeletal structure	Metal coordination geometry	Structural description	Figure	Ref.
$[Co(py_2S)Cl_2]$	2D	$\{CoN_4Cl_2\}$	$\{CoCl_2(py_2S)_2\}$ units linked into 2D networks; interpenetration results in a two-layer interwoven network	–	[94]
β-$[Co(dpe)_{1.5}(NO_3)_2]\cdot CH_3CN$	2D	$\{CoN_3O_4\}$	$\{Co(dpe)(NO_3)_2\}$ linear chains cross-linked by *gauche*-dpe ligands into a bilayer	24	[88]
$[Cd(dpb\text{-}F_4)_{1.5}](NO_3)_2$	2D	$\{CdN_3O_4\}$	$\{Cd(dpb\text{-}F_4)(NO_3)_3\}$ linear chains cross-linked by dpb-F_4 ligands into a 2D brick motif; three independent sheets interpenetrate	21	[86]
$[Ag(py_2urea)_2](BF_4)$	2D	$\{AgN_4\}$	2D network based on ligand-bridged distorted tetrahedral Ag^I sites, extended into three dimensions by hydrogen bonding	–	[95]
$[Ag(py_2oxalamide)_2](NO_3)$	2D	$\{AgN_4\}$	As above, but Ag···Ag distances are longer as controlled by the hydrogen bonding between the ligand backbones	–	[95]
$[Cu(dpe)_2](NO_3)_2\cdot 3C_6H_6\cdot 2MeOH$	3D	$\{CuN_4O_2\}$, long Cu···O distances	3D $CdSO_4$ type framework; two independent frameworks interpenetrate to generate large channels occupied by C_6H_6 and MeOH guest molecules	–	[96–98]
$[Cu(bpe)_2](PF_6)$	3D	$\{CuN_4\}$	tetrahedral {Cu(bpe)} sites each linked to four adjacent tetrahedral sites to form a 3D adamantoid structure; five such motifs interweave to form a polycatenated structure	–	[99]
$[Cu(dzp)_2](Pf_6)$	3D	$\{CuN_4\}$	tetrahedral $\{CuN_4\}$ sites linked through dzp ligands into a 3D adamantoid framework; three independent frameworks interpenetrate	–	[100]
$[Ag(tpc)](BF_4)$	3D	$\{AgN_4\}$	tetrahedral {Ag(tpc)} sites linked through the fused ligands to four adjacent Ag centers to give a 3D motif; there is no interpenatration of motifs	29	[101]
$[\{Cu(bpac)_2(H_2O)_2\}\{Cu(bpac)_2(NO_3)(H_2O)_2\}](NO_3)_4\cdot bpac\cdot 1.33H_2O$	3D	$\{CuN_4O_2\}$, two water molecules coordinated; $\{CuN_4OO'\}$, one water, one η^1-nitrate	linear {Cu(bpac)} chains, parallel and perpendicular, linked at the $\{CuN_4\}$ sites into a 3D framework; triply interpenetrated	–	[90]
C. bisimidazole bridges					
$[Ag_2(bix)_3](NO_3)_2$	1D	$\{AgN_3\}$, trigonal planar	$\{Ag_2(bix)_2\}$ rings linked by bix ligands into a 1D chain; chains interpenetrate to form a 2D polyrotoxane sheet	27	[102]
$[Zn(bix)_2](NO_3)_2\cdot 4.5H_2O$	2D	$\{ZnN_4\}$	tetrahedral $\{ZnN_4\}$ sites linked through bix ligands into a 2D polymeric sheet; two independent sheets interpenetrate to form a 2D polyrotaxane	28	[103]
$[Ni(bpa)_2(SO_4)(H_2O)]\cdot 4H_2O$	3D	$\{NiN_4O_2\}$, O donors from monodentate SO_4^{2-} group and an aqua ligand	network of fused $\{Ni_6(bpa)_6\}$ rings linked by bridging bpa groups into a 3D framework; two independent frameworks interpenetrate	—	[104]
$[Cu(bim)_{2.5}](ClO_4)_2\cdot 2MeOH$	3D	$\{CuN_5\}$, intermediate between square pyramidal and trigonal bipyramidal	distorted $\{Cu(bim)_{1.5}\}$ centers linked into hexagonal 2D sheets which are in turn linked above and below by bim groups to adjacent sheets to produce the 3D array	30	[105]
$[Mn(bbi)_3](BF_4)_2$	3D	$\{MnN_6\}$	octahedral $\{Mn(bbi)_3\}$ sites linked by bridging bbi ligands into a 3D framework; two frameworks interpenetrate	31	[106]
D. 1,3,5-triazine, 2,4,6-tri(4-pyridyl)-1,3,5-triazine, and 1,2,4-triazole					
$[Ag(tz)](CF_3SO_3)$	3D	$\{AgN_3O\}$	three-connected triazine ligands linking Ag tetrahedra into a 3D framework	–	[107]
$[Ag(tz)](CF_3SO_3)\cdot H_2O$	3D	$\{AgN_4\}$, $\{AgN_4F\}$, $\{AgN_3F\}$, $\{AgN_3O\}$	exclusively triconnected tz ligands bridging distorted Ag tetrahedra into a complex 3D framework	–	[108]
$[Cu(Htrz)Cl_2]$	1D	$\{CuCl_4N_2\}$	two-connected Htrz ligands bridging distorted octahedral Cu^{II} sites	–	[109]

Table 2. (Continued)

Compound	Metal–ligand skeletal structure	Metal coordination geometry	Structural description	Figure	Ref.
$[Cu_3(tpt)_4](ClO_4)_3$	3D	$\{CuN_4\}$	tetrahedral $\{CuN_4\}$ sites linked into a 3D framework; two independent interpenetrating 3D frameworks	34	[110]
$[Hg(tpt)_2](ClO_4)_2 \cdot 6C_2H_2Cl_4$	3D	$\{HgN_6\}$	octahedral $\{Hg(tpt)_3\}$ sites linked into a 3D framework; no interpenetration	–	[111]
$[Zn(CN)(tpt)_{2/3}(NO_3)] \cdot 0.75C_2H_2Cl_4 \cdot 0.75CH_3OH$	3D	$\{ZnN_3CO_2\}$, one N and one C from CN^- ligands	$\{Zn_4(CN)_4(NO_3)_4\}$ square grids linked by tpt ligands into a 3D framework; two independent frameworks interpenetrate	35	[112]
$[Cu_2Br_2(trz)]$	3D	$\{CuN_2Br_4\}$, Cu^{II} site; $\{CuNBr_2\}$, Cu^{I} sites.	2,4-triazolate-and Br-bridged $\{CuN_2Br_4\}$ chains linked by $\{CuBr_2N\}$ sites into a 2D network, linking through the 1-triazolate site achieves the 3D framework	– 69	[115]
E. pyridine, pyrazine, and pyrimidine					
$[Ag(pz)(NO_3)]$	1D	$\{AgN_2O_3\}$	linear chain of distorted trigonal bipyramidal $\{AgN_2O_3\}$ sites, linked by pz-bridging ligands; each Ag coordinates to a monodentate and a bidentate NO_3^- ligand	–	[116]
$[Ag(pz)](BF_4)$	1D	$\{AgN_2\}$	linear chains	–	[113]
$[Ag(pz)_3](BF_4)$	1D	$\{AgN_4\}$	zigzag chains of distorted tetrahedral $\{AgN_4\}$ sites linked by two-connected pz bridges; each Ag bonds to two terminal, one-connected pz ligands	–	[116]
$[Cu(pz)_2](CF_3SO_3)$	1D	$\{CuN_3O\}$	spiral chains of distorted tetrahedral Cu^{I} sites bridged by pz ligands; each Cu^{I} site bonds to a terminal pz and to an O donor of a $CF_3SO_3^-$ group	–	[117, 118]
$[Cu(pz)X_2]$ (X = Cl, Br)	1D	$\{CuN_2X_2\}$	linear chains cross-linked by long Cu···Br bonds into a 2D sheet	36	[119]
$[Ag(pz)](PF_6)_{0.5}(OH)_{0.5}$	1D	$\{AgN_2\}$	linear chains of alternating pz bridging ligands and digonal Ag^{I} sites	–	[107]
$[Ag(pz)_{1.5}](CF_3SO_3)$	1D	$\{AgN_3O\}$	linear $\{Ag(pz)\}$ chains linked to a neighboring chain by a bridging pz ligand to form a ladder motif	–	[107]
$[Cd(pz)Cl_2]$	1D	$\{CdN_2Cl_4\}$	mutually perpendicular linear $\{Cd(pz)\}$ chains and $\{CdCl_2\}$ chains linked into planar 2D sheets	36	[120]
$[Zn(pyrd)Cl_2]$	1D	$\{ZnN_2Cl_4\}$	mutually perpendicular undulating $\{Zn(pyrd)\}$ chains and $\{ZnCl_2\}$ chains, linked into undulating 2D sheets	–	[120]
$[Cu(pz)(dmg)_2]$	1D	$\{CuN_6\}$	linear chains	–	[121]
$[Cu(pzca)(Me_2CO)_{0.5}](BF_4)$	1D	$\{CuN_2O_2\}$, one oxygen from a μ^2-bridging acetone	1D $\{Cu(pzca)(Me_2CO)\}$ chains linked by bridging pzca molecules into a 3D helical framework	37	[122]
$[Cd(pyrd)(NO_3)_2] \cdot 2H_2O$	1D	$\{CdN_2O_4\}$	1D $\{Cd(\mu\text{-pyrd})(NO_3)_2(H_2O)_2\}$ chains; hydrogen bonding between chains results in a 3D framework	–	[123]
$[Cu_2Cl_2(pz)]$	2D	$\{CuN_2Cl_2\}$	$\{Cu_2Cl_2\}$ double chains linked through pz bridges into a 2D sheet	–	[124]
$[Cu_2(pz)_3](SiF_6)$	2D	$\{CuN_3\}$, trigonal planar	2D honeycomb networks constructed of $\{Cu_6(pz)_6\}$ hexagons	38	[82]
α-$[Ag_2(pz)_3](BF_4)_2$	2D	$\{AgN_3\}$	$\{Ag_3pz_3\}$ rings fused into an undulating sheet	–	[113]
$[Ag(pz)_2](PF_6)$	2D	$\{AgN_4\}$, distorted tetrahedral geometry	2D pleated sheets constructed of fused $\{Ag_6(pz)_7\}$ bicyclic folded rings	39	[125]
$[Ag(pz)_2][Ag_2(pz)_5](PF_6)_3$	2D	$\{AgN_5\}$, square pyramidal and $\{AgN_4\}$, square planer	Parallel sheets of fused $\{Ag_4(pz)_4\}$ square grids, linked by pz bridges into a double layers; such double layers alternate with simple sheets of fused $\{Ag_4(pz)_4\}$ square grids	41 b	[126]
$[Ag_{2.5}(pyrd)_3](ClO_4)_{2.5}$	1D	$\{AgN_2\}$ and $\{AgN_3O\}$	$\{Ag_4(pyrd)_4\}^{4+}$ squares cross-linked by $\{Ag(pyrd)_2\}^+$ units into a 1D chain	–	[127]
$[Cu_2(pzca)_3](ClO_4)_2 \cdot 2Me_2CO$	2D	$\{CuN_3O\}$, distorted trigonal pyramidal and $\{CuN_3O_2\}$, trigonal bipyramidal	$\{Cu_6(pzca)_6\}$ rings fused into a 2D sheet with a hexagonal motif	40	[122]
$[Ag_{2.5}(pyrd)_3](ClO_4)_{2.5}$	1D	$\{AgN_2\}$ and $\{AgN_3O\}$	$\{Ag_4(pyrd)_4\}^{4+}$ squares cross-linked by $\{Ag(pyrd)_2\}^+$ units into a 1D chain	–	[127]

Table 2. (Continued)

Compound	Metal–ligand skeletal structure	Metal coordination geometry	Structural description	Figure	Ref.
$[Ag_{2.5}(pyrd)_3](ClO_4)_{2.5}$	1D	$\{AgN_2\}$ and $\{AgN_3O\}$	$\{Ag_4(pyrd)_4\}^{4+}$ squares cross-linked by $\{Ag(pyrd)_2\}^+$ units into a 1D chain	–	[127]
$[Co(pz)_2(NCS)_2]$	2D	$\{CoN_4N'_2\}$, 4 pyrazine, 2 thiocyanate nitrogen donors.	Octahedral $\{Co(NCS)_2(pz)_4\}$ sites linked by pyrazine bridges into a layer	–	[128]
$[Co(pyrd)_2(NCS)_2]$	2D	$\{CoN_4N'_2\}$	As above	–	[128]
$[Cd(pz)X_2]$ (X = Cl, Br, I)	2D	$\{CdN_4X_2\}$	$\{CdX_2\}$ chains linked by pyrazine bridges into a layer	–	[123]
$[Cu(pz)_2(CH_3SO_3)]$	2D	$\{CuN_4O_2\}$	$\{Cu_4(pz)_4\}$ square grids fused into a sheet	–	[129]
$[Cu(Me_2pz)_3](PF_6)_2$	2D	$\{CuN_3\}$, two weakly interacting F donors from neighboring PF_6^- groups	puckered sheets of fused $\{Cu_6pz_6\}$ rings	–	[130]
$[Fe(pz)_2(NCS)_2]$	2D	$\{FeN_6\}$	2D sheet of fused square grids	–	[131]
$[Cu(pz)_2Cl_2]$	2D	$\{CuN_4Cl_2\}$	2D square grid	–	[132]
$[Ag(pz)_3](SbF_6)$	3D	$\{AgN_6\}$	octahedral $\{AgN_6\}$ sites linked into a cubic 3D framework	41 a	[126]
β-$[Ag_2(pz)_3](BF_4)_2$	3D	$\{AgN_3\}$	three equivalent 3D three-connected frameworks interpenetrate; each framework topologically related to α-$ThSi_2$	–	[113]
$[Ag_2(2,3\text{-}Me_2pz)_3](SbF_6)_2$	3D	$\{AgN_3\}$, T-shaped	Zigzag $\{AgN_2\}$ chains, cross-linked into a 3D framework; two independent frameworks interpenetrate	42	[133]
$[Cu(Me_2pz)_2](PF_6)$	3D	$\{CuN_4\}$	distorted tetrahedral $\{CuN_4\}$ sites linked into a 3D framework	–	[130]
$[Cu(pyrd)_2](BF_4)$	3D	$\{CuN_4\}$	tetrahedral $\{CuN_4\}$ sites linked by pyrimidine-bridging ligands into a 3D framework	43	[134]
F. hexamethylenetetramine and piperazine					
$[Ag_5(hmta)_6](PF_6)_5 \cdot 3CH_2Cl_2$	molecular	$\{AgN_2\}$, two additional weak Ag···F interactions	$[Ag_5(hmta)_6]^{5+}$ clusters	–	[135]
$[Ag(hmta)](SbF_6) \cdot H_2O$	1D	$\{AgN_3O\}$, $\{AgN_3F\}$	ribbons of distorted Ag tetrahedra linked by three-connected hmta ligand	–	[108]
$[Ag(hmta)](ClO_4)$	2D	$\{AgN_3\}$	hexagonal $\{Ag_6(hmta)_6\}$ rings fused into a 2D network	44	[136]
$[Ag(hmta)](NO_3)$	2D	$\{AgN_3\}$	as for $[Ag(hmta)](ClO_4)$.	–	[137]
$[Ag(pip)_2](BF_4)$	2D	$\{AgN_4\}$	folded $\{Ag_6(pip)_7\}$ bicyclic rings fused into an undulating 2D motif	–	[125]
$[Ag_3(hmta)_2](ClO_4)_3 \cdot 2H_2O$	3D	$\{AgN_3\}$ and $\{AgN_2\}$	hexagonal $\{Ag_6(hmta)_6\}$ rings fused into 2D networks, which are in turn bridged by digonally coordinated $\{AgN_2\}$ sites into a 3D framework	–	[136]
$[Ag(hmta)](PF_6) \cdot H_2O$	3D	$\{AgN_3\}$	trigonally flattened $\{AgN_3\}$ sites linked into a 3D helical framework	–	[138]
$[Ag_4(hmta)_3(H_2O)](PF_6)_4 \cdot 3EtOH$	3D	$\{AgN_2\}$ and $\{AgN_3\}$	hexagonal $\{Ag_6(hmta)_6\}^{6+}$ rings linked through three-coordinate Ag sites into a 3D framework	45	[135]
$[Ag_{11}(hmta)_6](PF_6)_{11}$	3D	$\{AgN_2\}$, $\{AgN_3O\}$, $\{AgN_2O_2\}$, $\{AgN_2O\}$, $\{AgN_2F\}$	2D networks of fused $\{Ag_6(hmta)_6\}$ and $\{Ag_3(hmta)_3\}$ rings linked by $\{AgN_2\}$ bridges into a 3D framework	–	[108]
G. hexakis(imidazol-1-ylmethyl)benzene					
$[Cd(hkimb)F_2] \cdot 14H_2O$	3D	$\{CdN_6\}$	3D NaCl-related covalent framework. Water molecules occupy the cavities	–	[139]
H. mixed ligand bridges					
$[Cu(4,4'\text{-bpy})(pz)(H_2O)_2](PF_6)$	2D	$\{CuN_4O_2\}$ 2 pyrazine and 2 4,4′-bpy donors	2D rectangular gridwork	–	[140]

[a] Abbreviations: bbi = N,N′-butylenebisimidazole; bbp = 1,3-bis(4-pyridyl)propane; bim = 1,2-bis(imidazolyl)ethane; bix = 1,4-bis(imidazol-1-ylmethyl)-benzene; bpa = 4,4′-bipyridylamine; bpac = 4,4′-bipyridylacetylene; bpbd = 1,4-bis(4-pyridyl)butadiyne; bpe = 1,2-*trans*-bis(4-pyridyl)ethene; bpp = 2,3-bipyridylpyrazine; bppy = 2,5-bis(2-pyridyl)pyrazine; 2,2′bpy = 2,2′bipyridine; 4,4′bpy = 4,4′bipyridine; bpy-4pz = 4-thiomethyl-6-(4-pyridyl)-2,2′-bipyridine; dmp = 2,9-dimethyl-1,10-phenanthroline; dpb = 1,4-bis(4-pyridyl)benzene; dpb-F_4 = 1,4-bis(4-pyridyl)tetrafluorobenzene; dpe = 1,2-bis(4-pyridyl)-ethane; dzp = 2,7-diazapyrene; en = ethylendiamine; hkimb = hexakis(imidazol-1-ylmethyl)benzene; hmta = hexamethylenetetramine; Htrz = 1,2,4-triazole; Htz = 1,3,4-triazole; pip = piperazine; py_2S = 4,4′-dipyridyl sulfide; pyrd = pyrimidine; pytz = 3,6-bis(4-pyridyl)-1,2,4,5-tetrazine; pz = pyrazine; pzca = pyrazinecarboxamide; tpc = 1,2,3,4-tetrakis(4-pyridyl)cyclobutane; tpt = 2,4,6-tris(4-pyridyl)1,3,5-triazine; tz = 1,3,5-triazine.

skeletal core as terminating groups which passivate the growing oxide surface or as bridging units which can stitch separate molybdenum oxide units into larger assemblies. These arguments will be elaborated in Section 4.

3.1. Two- and Three-Connected Organoamine Ligands

The structures of the coordination polymers of interest are derived from metal-bridging ligand building blocks which contain nitrogen donors in simple geometric dispositions. The most extensively studied two-connected bridging ligand of this type is 4,4′-bipyridine (4,4′-bpy). While the dispositions of donor groups in the related 2,2′-bipyridine and *o*-phenanthroline preclude a metal-bridging role, it will be demonstrated that these ligands afford useful chelates for stabilization of peripheral heterometal sites on molybdenum oxide surfaces or for passivation of molybdenum oxide surfaces.

A degree of structural control may be introduced by manipulation of the disposition of 4-pyridyl groups of the parent 4,4′-bipyridine ligand through introduction of various tether groups. Linear rigid rods with varying spacer lengths are represented by 1,4-bis(4-pyridyl)benzene (dpb), 1,4-bis(4-pyridyl)butadiyne (bpbd), and diazapyrene (dzp). The relative orientations of the pyridyl donors can be modified by introduction of appropriate fixed spacers, as in 1,2-*trans*-bis-(4-pyridyl)ethene (bpe) and bis(4-pyridyl)amine (bpa), or conformationally flexible tethers, as in 1,2-bis(4-pyridyl)-ethane (dpe) and 1,3-bis(4-pyridyl)propane (bpp). The influence of donor-group identity may be addressed as well by the use of imidazole-bridged donors. Furthermore, the donor-group spacing can be dramatically shortened by adoption of pyrazine (pz) or piperazine (pip) as the bridging ligands, while the relative donor-group orientation may be altered as well by pyrimidine (pyrd). The trigonal three-connected ligand type is represented by 2,4,6-tris(4-pyridyl)-1,3,5-triazine (tpt). While square-planar four-connectors have been developed,[62] these will not be discussed here.

3.2. Coordination Polymers Constructed from 4,4′-Bipyridine

The expansive chemistry of coordination polymers based on 4,4′-bipyridine includes one-, two-, and three-dimensional motifs exhibiting diamondoid, grid, ladder, brick, railroad, and octahedral building blocks. The dimensionality of the metal–bipyridyl skeletal unit provides a utilitarian framework for the description of the crystal chemistry of this subclass of coordination polymers.

3.2.1. One-Dimensional 4,4′-Bipyridyl-Based Coordination Polymers

Linear one-dimensional metal–4,4′-bipyridine subunit structures are the most common motif encountered. As shown in Figure 6, the structure of $[Cu(4,4'\text{-bpy})(BF_4)_2(H_2O)_2]\cdot(4,4'\text{-bpy})$[63] consists of octahedral Cu^{II} sites linked through 4,4′-bipyridine groups into a linear chain. The equatorial plane of the copper is occupied by fluorine atoms from each of two BF_4^- groups and two aquo ligands. The aquo groups participate in hydrogen bonding to the uncoordinated 4,4′-bipyridine to produce a two-dimensional hydrogen-bonded network. This is a common characteristic of these one-dimensional materials, shared by the first six entries of Table 2. However, the detailed architecture of the hydrogen-bonding interactions to produce the sheetlike structures may display considerable variations, as indicated by the first fifteen entries of Table 2. The structure of $[Fe(4,4'\text{-bpy})(H_2O)_3(ClO_4)](ClO_4)\cdot 1.5(4,4'\text{-bpy})\cdot H_2O$[66] (Figure 7) illustrates this point. In this case, there are alternating single and double hydrogen-bonded 4,4′-bpy bridges between the $\{Fe(H_2O)_3(ClO_4)(4,4'\text{-bpy})\}^+$ chains.

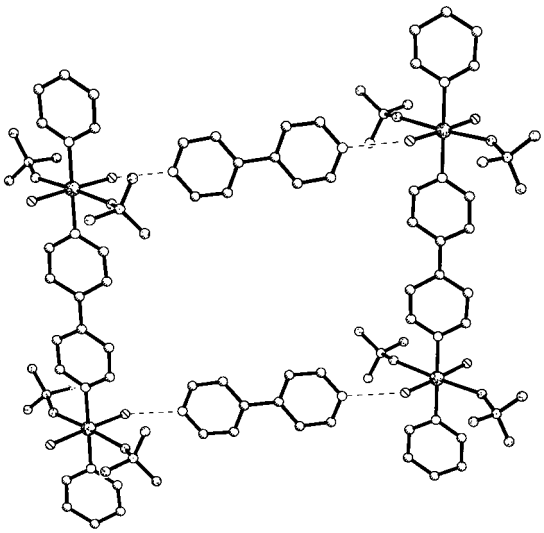

Figure 6. A view of the one-dimensional $\{Cu(4,4'\text{-bpy})(BF_4)_2(H_2O)_2\}$ chains linked into a two-dimensional network through hydrogen bonding of the coordinated aquo ligands to the interstrand 4,4′-bipyridine groups in $[Cu(4,4'\text{-bpy})(BF_4)_2(H_2O)_2]\cdot(4,4'\text{-bpy})$.

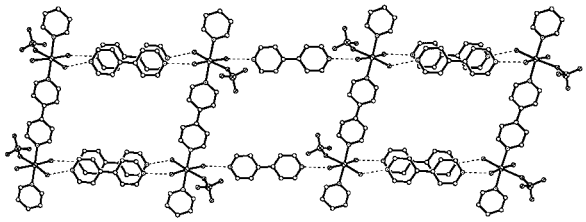

Figure 7. A view of the sheetlike structure adopted by $[Fe(4,4'\text{-bpy})(H_2O)_3(ClO_4)](ClO_4)\cdot 1.5(4,4'\text{-bpy})\cdot H_2O$, which is constructed from linear $\{Fe(4,4'\text{-bpy})(H_2O)_3(ClO_4)\}^+$ chains linked by alternating single and double hydrogen-bonded 4,4′-bpy bridges.

The {M(4,4′-bpy)} motif is subject to considerable structural modification, which reflects the coordination preference of the metal and the nature of the coligands. For example, the Cu^I derivative $[Cu(4,4'\text{-bpy})(MeCN)_2](BF_4)$[67] exhibits zigzag chains (Figure 8), which reflects the preference of the metal for tetrahedral rather than tetragonal or octahedral geometry. Metal coordination and the metal–ligand stoichiometry are reflected in the structure of $[Co(4,4'\text{-bpy})_{1.5}(NO_3)_2]\cdot MeCN$[68]

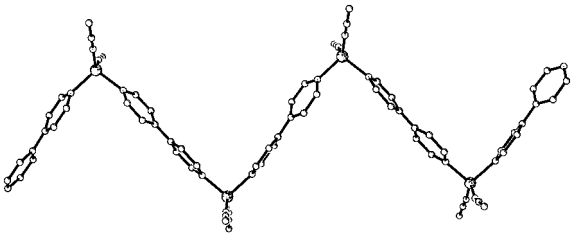

Figure 8. A view of the zigzag $\{Cu(4,4'\text{-bpy})(MeCN)_2\}^+$ cationic chains of $[Cu(4,4'\text{-bpy})(MeCN)_2](BF_4)$.

(Figure 9). The 4,4′-bpy ligands coordinate to the Co^{2+} ions to form the siderails and the rungs of a one-dimensional ladder. Alternatively, the structure may be described as a square motif, propagated in one dimension. The remaining coordination sites are occupied by bidentate NO_3^- groups. An

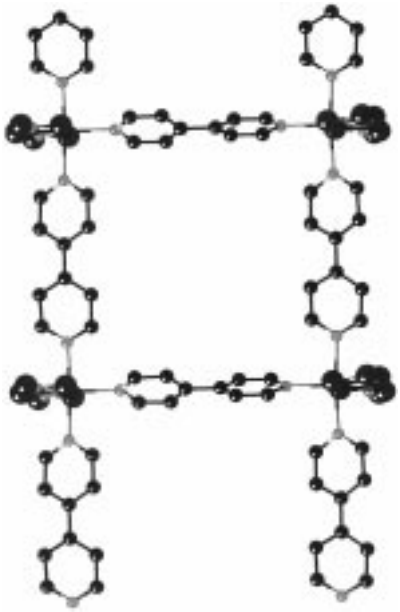

Figure 9. A view of the ladder structure adopted by $[Co(4,4'\text{-bpy})_{1.5}(NO_3)_2]$.

intriguing structural variant is presented by $[Ni(4,4'\text{-bpy})_{2.5}(H_2O)_2](ClO_4)_2 \cdot 1.5(4,4'\text{-bpy}) \cdot 2H_2O$[69] (Figure 10). The ladder or square-grid motif of $[Co(4,4'\text{-bpy})_{1.5}(NO_3)_2]$ is maintained. However, an additional 4,4′-bpy moiety is coordinated to each Ni^{II} site as a monodentate ligand, which projects a pendant pyridyl group into the interstrand volume to produce

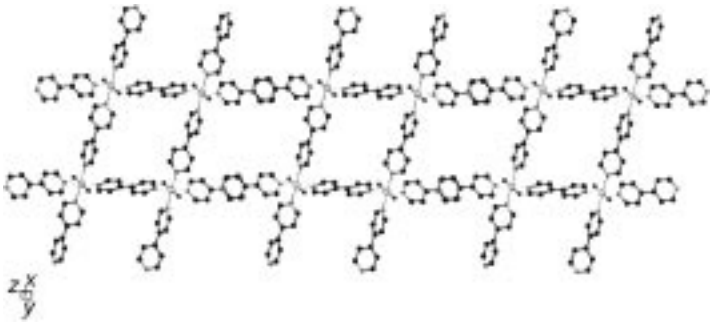

Figure 10. The railroad motif adopted by $[Ni(4,4'\text{-bpy})_{2.5}(H_2O)_2](ClO_4)_2 \cdot 1.5(4,4'\text{-bpy}) \cdot 2H_2O$ as a consequence of the monodentate coordination of one 4,4′-bpy ligand to each Ni^{II} site.

a railroadlike motif. Curiously, the pendant pyridyl groups π stack to form an extended two-dimensional network. The ClO_4^- and H_2O, and uncoordinated 4,4′-bpy units occupy the channels formed by the stacking of these sheets.

Coligand influences are demonstrated in the structure of $[CuBr_2(4,4'\text{-bpy})]$.[70] As shown in Figure 11, the structure consists of linear $\{Cu(4,4'\text{-bpy})\}$ chains linked through bridging Br^- ions into a two-dimensional network. The structure reflects the preference of Cu^{II} for tetragonally distorted six-coordinate geometry and the bridging mode preferred by halides in Cu^{II} phases.

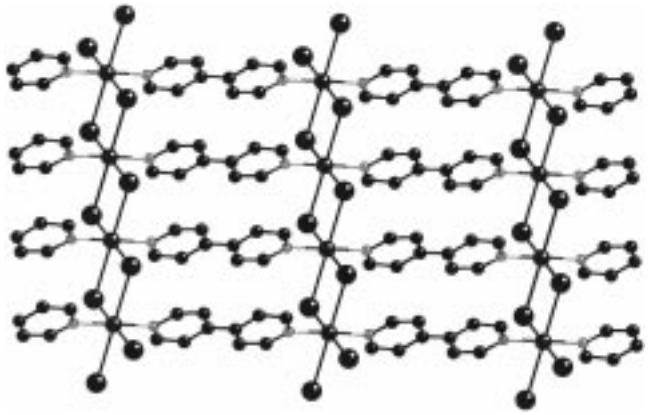

Figure 11. A view of the layer structure of $[CuBr_2(4,4'\text{-bpy})]$, which may be alternatively described as $\{CuBr_2\}$ chains linked by 4,4′-bpy bridges.

A particularly unusual example of the structural influence of the metal is provided by $[Ag(4,4'\text{-bpy})](NO_3)$[71] As shown in Figure 12, the structure consists of linear $\{Ag(4,4'\text{-bpy})\}^+$ chains cross-linked by long Ag–Ag contacts into a three-dimensional framework based on T-shaped building blocks. In common with many coordination polymers of the two- or three-dimensional type, the void space is severely reduced by interpenetration, in this case of three independent frameworks. The NO_3^- counterions nestle in the restricted stairlike microchannels which are formed in this assembly. Interpenetration of two or more independent infinite substructures is a recurrent feature of framework solids. Entanglement based on polycatenane or polyrotaxane architecture appears as an inherent attribute of such structures. The excellent review by Batten and Robson[188] discusses the phenomenon of ordered interpenetration in detail.

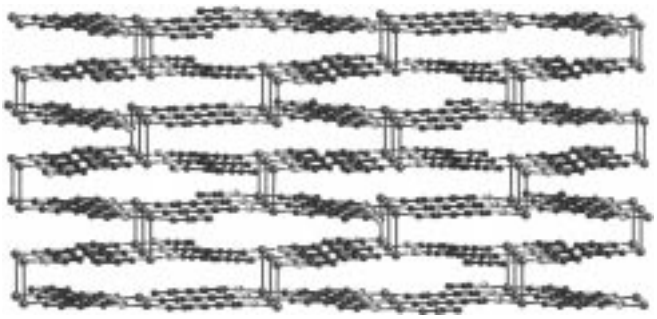

Figure 12. The three-dimensional structure of $[Ag(4,4'\text{-bpy})](NO_3)$, which consists of $\{Ag(4,4'\text{-bpy}\}^+$ chains linked through long Ag···Ag contacts, showing one of three independent frameworks.

3.2.2. Two-Dimensional 4,4′-Bipyridine-Based Coordination Polymers

The fundamental two-dimensional motif of fused square grids is represented in the structure of $[Cd(4,4'\text{-bpy})_2(NO_3)_2]\cdot 2\,C_6H_4Br_2$[74] (Figure 13). The sheets are constructed from fused $\{Cd(4,4'\text{-bpy})_2\}^{2+}$ square grids, with each Cd^{II} site additionally coordinated in a monodentate fashion to two NO_3^- groups which project above and below this plane. The layers are stacked parallel and in registry with an interplane separation of 6.30 Å. Again, there is interpenetration of two independent stacks.

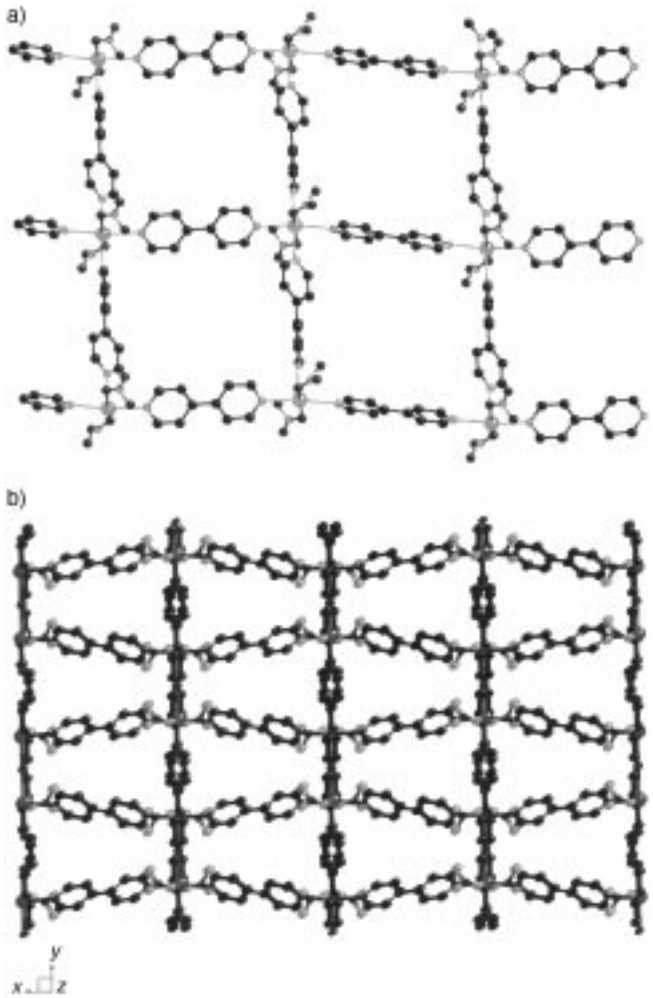

Figure 13. a) A view of the two-dimensional square grid pattern adopted by the layer networks of $[Cd(4,4'\text{-bpy})_2(NO_3)_2]\cdot 2\,C_6H_4Br_2$. b) A view along the crystallographic *c* axis of the two-dimensional networks stacked to form microchannels.

In an attempt to avoid interpenetration, $[Zn(4,4'\text{-bpy})_2(SiF_6)]\cdot DMF$[76] was prepared and shown to consist of $\{Zn(4,4'\text{-bpy})_2\}^{2+}$ layers, constructed from the square-grid motif, and linked through bridging SiF_6^{2-} anions into a three-dimensional covalent framework. The resulting square channels are occupied by guest molecules.

Another strategy for modifying the architecture of the two-dimensional network relies on the introduction of a coligand, as demonstrated in $[Cu_2(C_3H_2O_4)_2(H_2O)(4,4'\text{-bpy})]\cdot H_2O$[77] (Figure 14). The structure consists of $\{Cu_4(malonate)_4\}$ squares linked into a larger square grid through 4,4′-bpy groups. It is noteworthy that the Cu^{II} center adopts square pyramidal $\{CuNO_4\}$ geometry.

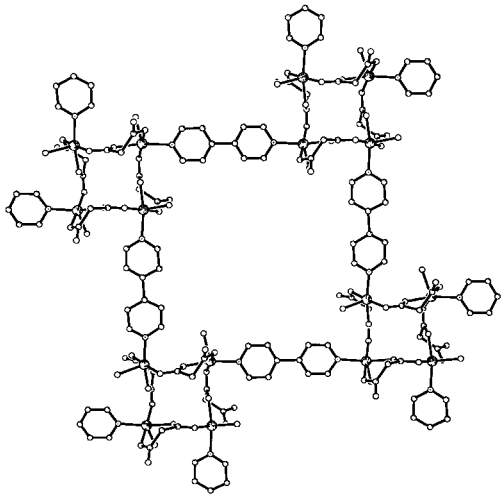

Figure 14. A view of the layer structure of $[Cu_2(C_3H_2O_4)_2(H_2O)(4,4'\text{-bpy})]\cdot H_2O$ to show the $\{Cu_4(malonate)_4\}$ squares linked by 4,4′-bpy bridges.

The structural versatility of these coordination polymers is once again dramatically illustrated by the structure of $[Co_2(4,4'\text{-bpy})_3(NO_3)_4]\cdot H_2O$.[78] The pentagonal bipyramidal $\{CoN_3O_4\}$ sites are linked by 4,4′-bpy groups into one-dimensional chains. As shown in Figure 15, parallel chains are cross-linked through 4,4′-bpy bridges to an adjacent set of parallel chains to produce a double-sheet motif. The double sheets interlock by interdigitation of chains into a complex three-dimensional tongue-and-groove structure.

As illustrated in Figure 16, coligand influences are also manifest in the structure of [Cu(4,4′-bpy)Cl].[79] The structure consists of binuclear Cu^I sites bridged by two chloride atoms $\{Cu_2Cl_2\}$ linked through 4,4′-bpy groups into layers with a large hexagonal grid pattern. Once again, there are two independent sets of interpenetrating two-dimensional motifs.

3.2.3. Three-Dimensional 4,4′-Bipyridine-Based Coordination Polymers

The structure of $[Ag(4,4'\text{-bpy})_2](CF_3SO_3)$[81] (Figure 17) is prototypical of the diamondoid family[52] of three-dimensional materials. The structure consists of tetrahedral $\{AgN_4\}$ sites linked through 4,4′-bpy ligands into a three-dimensional adamantoid framework; four independent frameworks interpenetrate so as to effect efficient packing.

The influence of metal coordination preference and ligand stoichiometry is evident in the structure of $[Cu(4,4'\text{-bpy})_{1.5}](NO_3)\cdot 1.25\,H_2O$[84] (Figure 18). In this instance, the Cu^I sites, which adopt trigonal-planar $\{CuN_3\}$ coordination, are linked by the 4,4′-bpy ligands to form six interpenetrating three-dimensional frameworks. The trigonal geometry of the copper precludes the adamantoid unit as the building block for the framework.

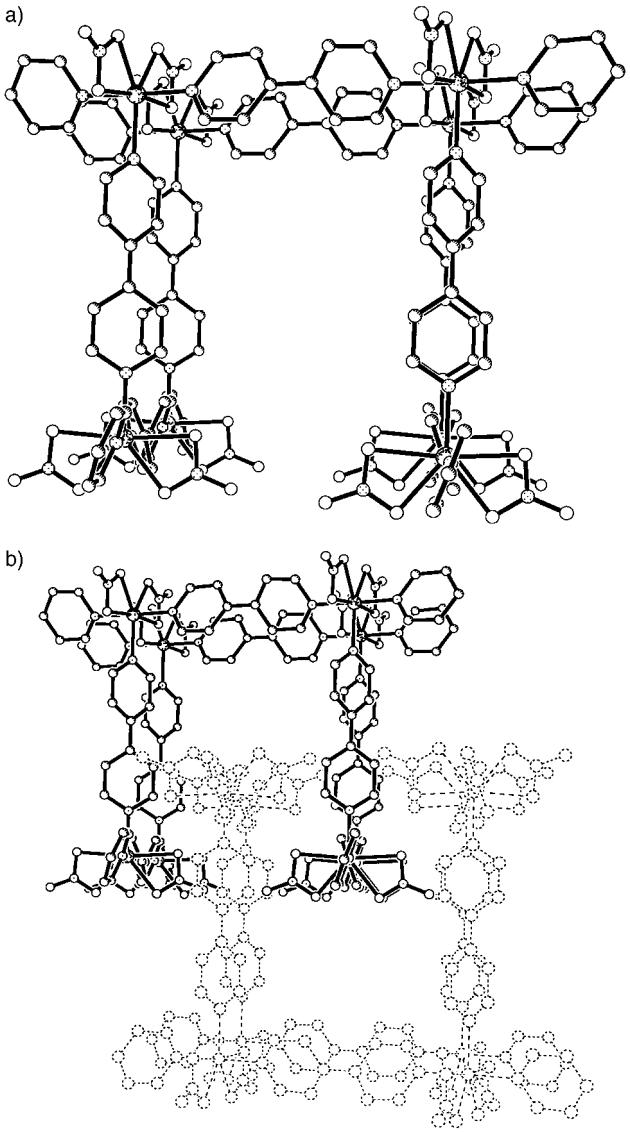

Figure 15. a) The double-sheet motif of $[Co_2(4,4'\text{-bpy})_3(NO_3)_4]\cdot H_2O$, constructed from $\{Co(4,4'\text{-bpy})(NO_3)_2\}$ linear chains linked by 4,4′-bpy bridges. One set of chains lies parallel to the plane of the page while the second set is normal to the page. b) A view of the interlocking of adjacent double sheets.

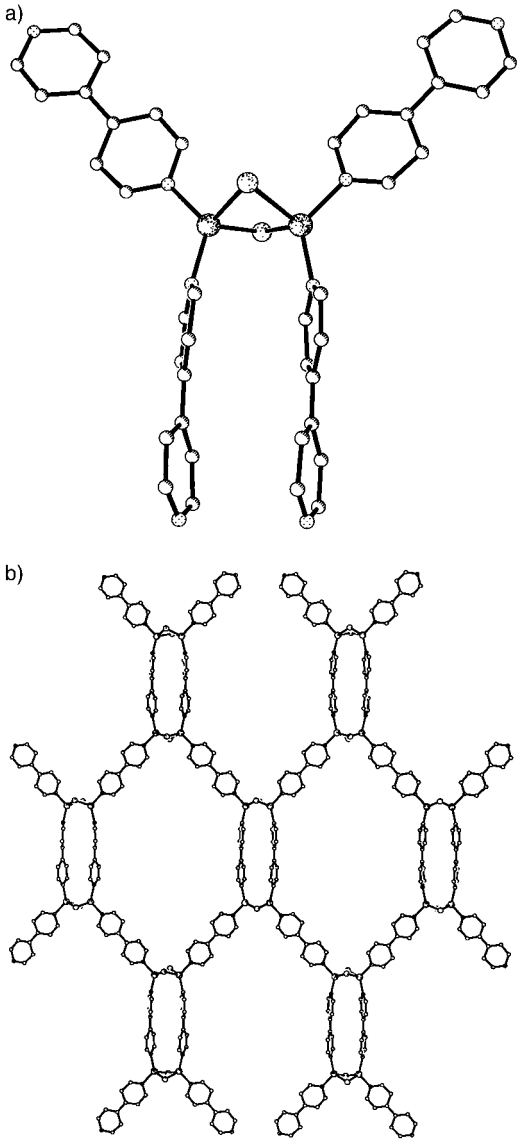

Figure 16. a) Structure of the binuclear $\{Cu_2Cl_2(bpy)_4\}$ fundamental building block of [CuCl(4,4′-bpy)]. b) The two-dimensional hexagonal grid pattern of one of the independent layers in [CuCl(4,4′-bpy)].

3.3. Coordination Polymers Constructed from Tethered Pyridine and Imidazole Groups

The structural consequences of introducing spacers between the nitrogen donor groups can be quite dramatic. Tethers may be introduced which simply add extension to the rodlike bipyridyl ligand, as for 1,4-bis(4-pyridyl)butadiyne, or which maintain a rigid backbone while reorienting the donor groups, as for 1,2-*trans*-bis(4-pyridyl)ethene or which allow conformational flexibility to the ligands, as for 1,2-bis(4-pyridyl)ethane.

3.3.1. One- and Two-Dimensional Coordination Polymers with Tethered Nitrogen Donors

The structural modifications consequent to extension of the donor-to-donor distance are manifested in the structure of

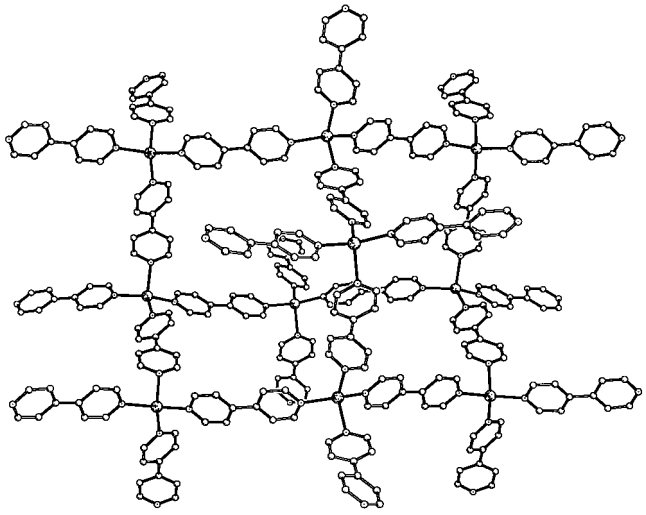

Figure 17. One adamantoid unit of the three-dimensional framework structure of $[Ag(4,4'\text{-bpy})_2](CF_3SO_3)$.

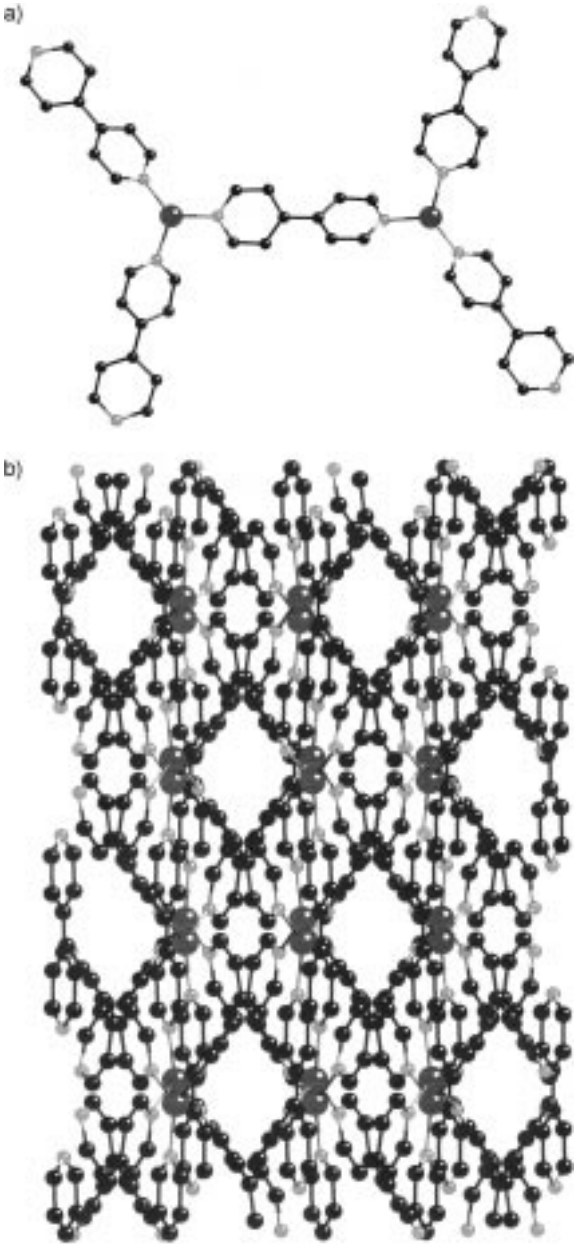

Figure 18. a) The fundamental building block of the three-dimensional structure of $[Cu(4,4'\text{-bpy})_{1.5}](NO_3)\cdot 1.25\,H_2O$. b) A view down the crystallographic *c* axis illustrating the consequences of interpenetration of the independent three-dimensional frameworks to give channels occupied by the NO_3^- anions and water molecules.

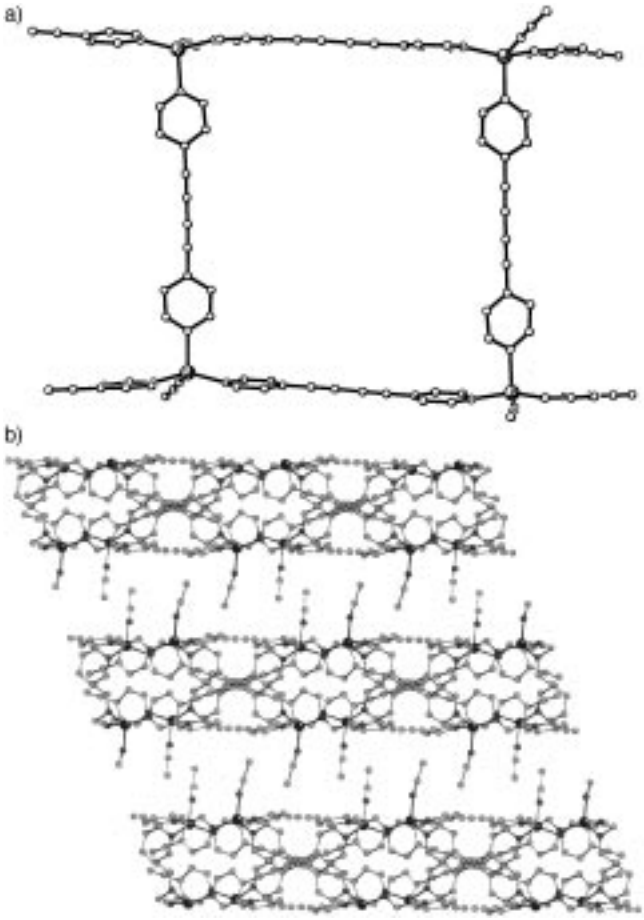

Figure 19. a) The ladder structure of $[Cu_2(bpbd)_3(MeCN)_2](PF_6)_2$. b) The results of interpenetration to form sheets of polycatenated braids parallel to the *ac* plane.

$[Cu_2(bpbd)_3(MeCN)_2](PF_6)_2$.[85] As illustrated in Figure 19, the structure consists of tetrahedral $\{CuN_4\}$ sites linked through bpbd ligands into an undulating ladder. This contrasts with the ladder structure of $[Co(4,4'\text{-bpy})_{1.5}(NO_3)_2]$, which is flat with all linking ligands coplanar. Furthermore, while the Co^{2+} species exhibited no interpenetration, in this case each ladder is interpenetrated by four additional ladders to form a polycatenated braid which extends into a sheet.

The Cd^{II} compound $[Cd(dpb)_{1.5}(NO_3)_2]$[86] also exhibits a ladder motif (Figure 20). In contrast to the structure of $[Cu_2(bpbd)_3(MeCN)_2](PF_6)_2$, the Cd material possesses a flat ladder motif but with bent rungs and siderails. Two independent sets of ladders interpenetrate such that a given ring interlocks with four rings of adjacent ladders. Curiously, substitution of dpb-F_4, the tetrafluoro analogue of dpb, yields $[Cd(dpb\text{-}F_4)_{1.5}(NO_3)_2]$, which, despite the similar formulation, exhibits the two-dimensional bricklike structure shown in Figure 21. Once again there is interpenetration with three independent brick motifs interwoven to produce a two-dimensional slab.

The structural chemistry of coordination polymers is significantly expanded by the introduction of conformationally flexible tethers between donor groups. This observation is nicely illustrated by the structures of $[Ag(bbp)](CF_3SO_3)\cdot$ EtOH, $[Ag(bbp)](CF_3SO_3)$ and $[Ag_2(bbp)_4](CF_3SO_3)_2\cdot bbp$[87] (Figure 22), which consist of sinusoidal chains, helical chains paired into double chains and binuclear $\{Ag_2(bbp)_2\}$ rings fused into tubular motifs, respectively. The structures reveal the role of the variability of the metal coordination number in the determination of structure type. The Ag site of $[Ag(bbp)](CF_3SO_3)\cdot EtOH$ exhibits the characteristic $\{AgN_2\}$ digonal geometry. In contrast, the Ag site of $[Ag(bbp)](CF_3SO_3)$ is T-shaped, in a fashion reminiscent of $[Ag(4,4'\text{-bpy})](NO_3)$, with the long Ag–Ag interaction providing the connectivity between helical chains in the double chain. In $[Ag_2(bbp)_4](CF_3SO_3)_2\cdot bbp$, the Ag site enjoys

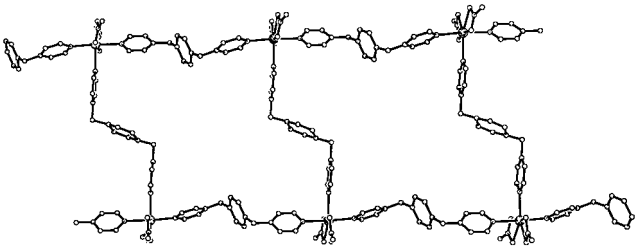

Figure 20. The ladder motif of $[Cd(dpb)_{1.5}(NO_3)_2]$.

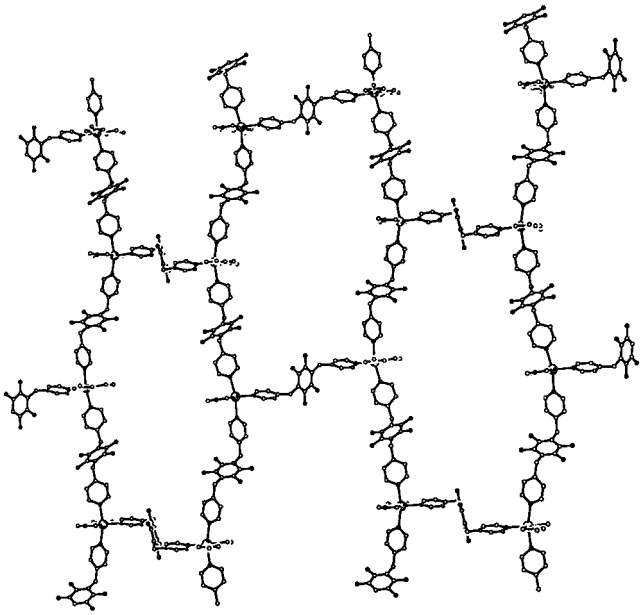

Figure 21. The two-dimensional brick motif of $[Cd(dpb\text{-}F_4)_{1.5}(NO_3)_2]$.

tetrahedral $\{AgN_4\}$ geometry. It is also noteworthy that in this latter structure, the uncoordinated bbp threads the $\{Ag_2(bbp)_2\}$ rings of the tube.

Similarly, the α, β, and γ forms of $[Co(dpe)_{1.5}(NO_3)_2]\cdot Sol$[88] (Sol = solvent molecule) reflect the conformational flexibility of the ligand, which can adopt angular or linear orientations of the donor groups. The α isomer is isostructural with $[Cd(dpe)_{1.5}(NO_3)_2]$[89] and consists of two *gauche* spacers linking Co^{II} sites into a box, linked at the metal edges by *anti* spacers to give linear chains (Figure 23). In contrast, the β isomer contains two *anti* spacers for each *gauche* ligand to produce the bilayer structure shown in Figure 24. In the γ isomer, all spacer ligands adopt the *anti* conformation to produce a ladder structure similar to that described previously.

Coligand influences are evident in the structures of $[Ag_2(bpy\text{-}4pz)_2](PF_6)_2$[92] and $[Cu_4(bppy)(CH_3CO_2)_8]$.[93] Figure 25 shows the structure of $[Ag_2(bpy\text{-}4pz)_2](PF_6)_2$ which exhibits a bridging ligand constructed from 2-pyridyl groups linked by a 4-thiomethylpyridine tether. The affinity of Ag^I for sulfur donors is evidenced by the introduction of the thioether donor into the metal $\{AgN_3S\}$ coordination sphere. The structure consists of $\{Ag_2(bpy\text{-}4pz)_2\}$ binuclear rings linked through Ag–S bonds into a one-dimensional chain.

The structure of $[Cu_4(bppy)(CH_3CO_2)_8]$[93] is also based on tethered 2-pyridyl groups, with pyrazine as the linker in this

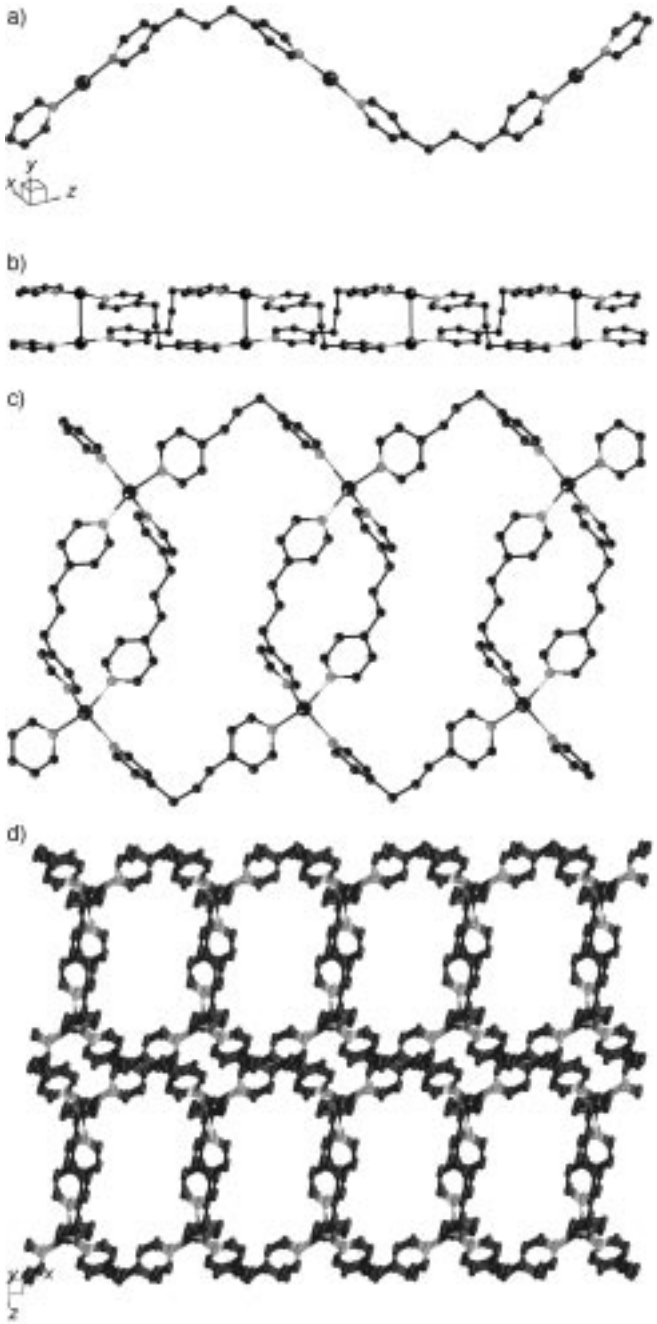

Figure 22. a) The sinusoidal chain of $[Ag(bbp)](CF_3SO_3)\cdot EtOH$. b) A view of the helical chains linkage in $[Ag(bbp)](CF_3SO_3)$. c) The linkage of $\{Ag_2(bbp)_2\}$ rings into tubular channels in $[Ag_2(bbp)_4](CF_3SO_3)_2\cdot bbp$. d) The results of interpenetration of tubes in $[Ag_2(bbp)_4](CF_3SO_3)_2\cdot bbp$.

instance. The structure is constructed from $\{Cu_2(acetate)_2\}$ dimers bridged by bppy ligands into a one-dimensional chain (Figure 26). Each Cu^{II} site of the chain exhibits square-pyramidal $\{CuN_2O_3\}$ geometry. In addition to the μ^2-acetate of the $\{Cu_2(acetate)_2\}$ grouping, each Cu site binds to a third acetate ligand which directs its second oxygen donor into the interstrand region. These donors are used to bond to $\{Cu_2(acetate)_4\}$ binuclear units which serve to link the chains into a two-dimensional sheet.

The consequences of donor-group modification may be perceived in the structure of $[Ag_2(bix)_3](NO_3)_2$[102] (Figure 27).

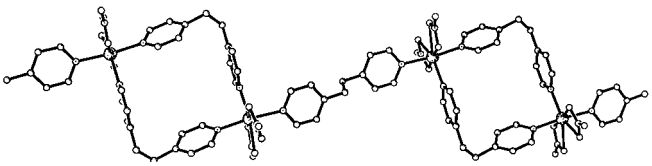

Figure 23. The one-dimensional structure of α-$[Co(dpe)_{1.5}(NO_3)_2]$.

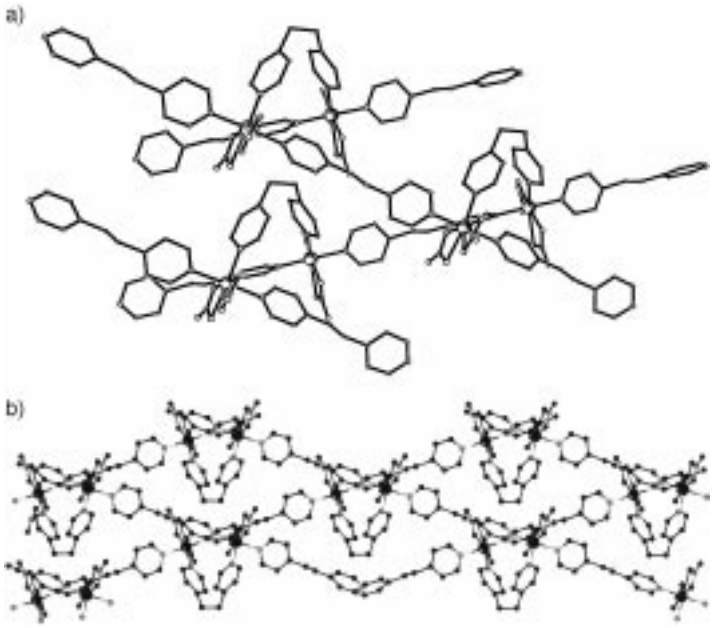

Figure 24. Two views of the bilayer formed by the linking of sets of parallel $\{Co(dpe)(NO_3)_2\}$ chains by *gauche* dpe ligand bridges to provide the building block for the bilayer motif of β-$[Co(dpe)_{1.5}(NO_3)_2]$.

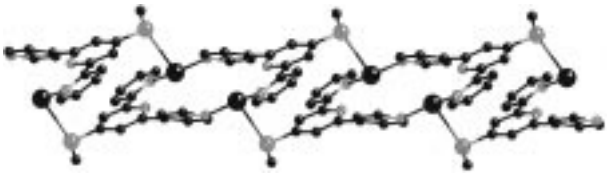

Figure 25. The one-dimensional chain of$[Ag_2(bpy\text{-}4pz)_2](PF_6)_2$.

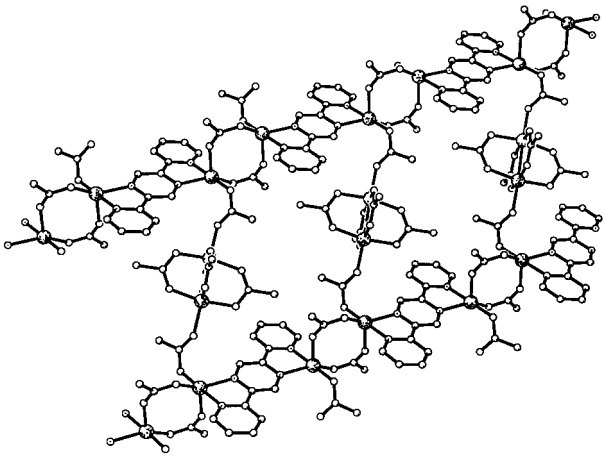

Figure 26. The structure of $[Cu_4(bppy)(CH_3CO_2)_8]$.

The structure is constructed from $\{Ag_2(bix)_2\}$ rings which are linked through a third bridging bix ligand into a one-dimensional chain of equispaced loops or rings. The chains interpenetrate with connector rods through the loops to form a polyrotaxane two-dimensional sheet.

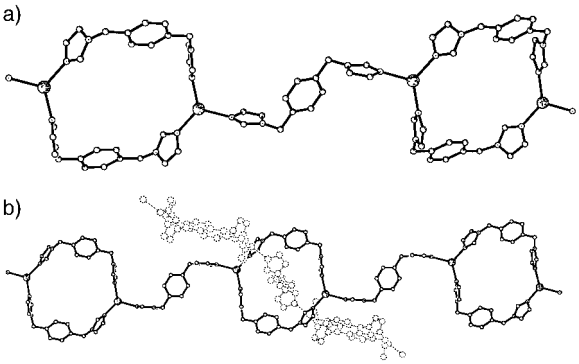

Figure 27. a) A view of a single chain motif of $[Ag_2(bix)_3](NO_3)_2$. b) The interpenetration of chains.

A polyrotaxane structure is also adopted by $[Zn(bix)_2]$-$(NO_3)_2 \cdot 4.5\,H_2O$,[103] but with a distinct structure from that of $[Ag_2(bix)_3](NO_3)_2$ as a consequence of the coordination geometry at the Zn^{II} site. As shown in Figure 28, the structure is constructed of $\{Zn_2(bix)_2\}$ rings linked by bix bridges into a two-dimensional sheet. Two independent sheets interpenetrate to form an extended two-dimensional rotaxane structure.

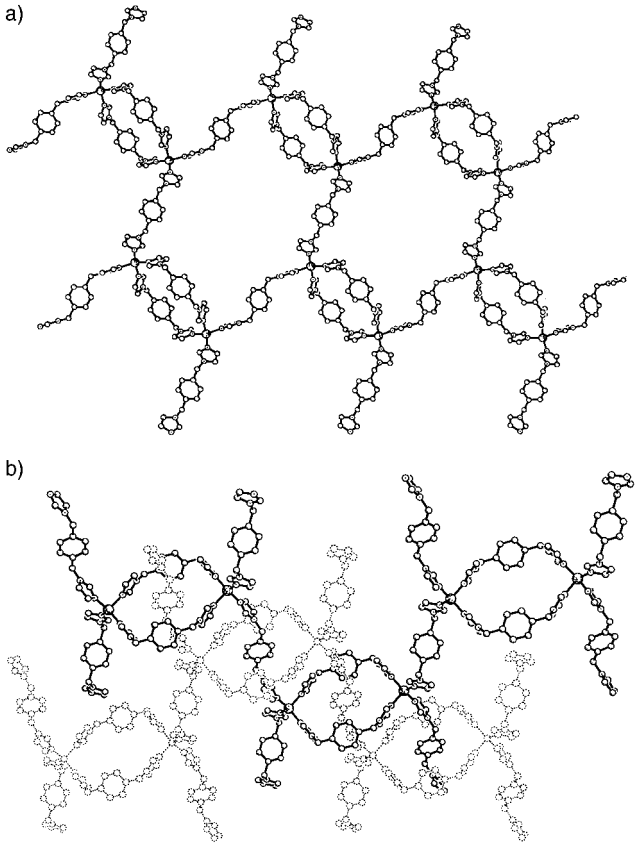

Figure 28. a) A view of one two-dimensional motif of $[Zn(bix)_2](NO_3)_2 \cdot 4.5\,H_2O$. b) The interpenetration of two independent sheets.

3.3.2. Three-Dimensional Coordination Polymers with Tethered Nitrogen Donors

The structure of $[Cu(bpe)_2](BF_4)$[99] illustrates the consequences of lengthening the bipyridyl ligand. The tetrahedral $\{CuN_4\}$ sites are linked through bridging bpe ligands into a

three-dimensional framework of edge-sharing adamantoid units. It is noteworthy that five independent frameworks interpenetrate to produce channels occupied by BF_4^- counterions and solvent molecules. In contrast, $[Cu(4,4'\text{-bpy})_2](PF_6)$ and $[Ag(4,4'\text{-bpy})_2](CF_3SO_3)$ were seen to exhibit four interpenetrating motifs. Consequently, space extension results in larger cavities and inclusion of an additional framework. It is noteworthy that $[Cu(dzp)_2](PF_6)$[100] also exhibits the adamantoid motif but with only three interpenetrating frameworks, an observation that suggests that the steric bulk of the ligand prevents interpenetration by a fourth framework.

An unusual structure is presented by $[Ag(tpc)](BF_4)$,[101] where reaction of $AgBF_4$ with 1,2-*trans*-bis(4-pyridyl)ethene in organic solvents in light results in the in situ cyclization of the ligand to a cyclobutane-linked tetrapyridyl ligand. The tetrahedral $\{AgN_4\}$ geometry at each Ag^+ site gives rise to the three-dimensional framework of Figure 29. Most significantly, there is no interpenetration.

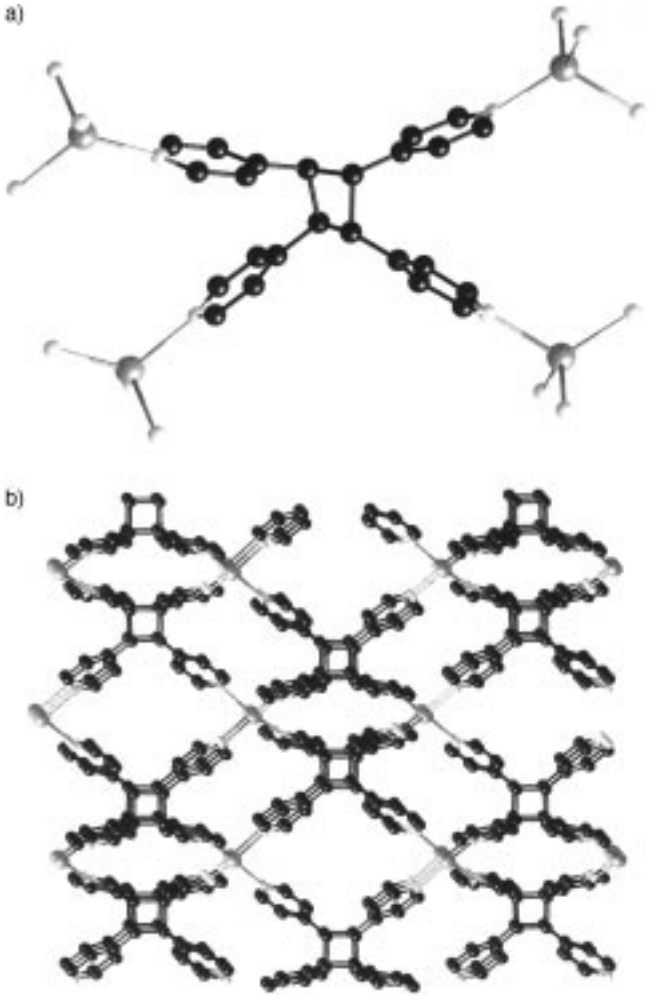

Figure 29. a) The tpc ligand of $[Ag(tpc)](BF_4)$. b) A view of the channels formed by the covalently linked framework of $[Ag(tpc)](BF_4)$.

Substitution of imidazole donors for pyridyl nitrogens again produces unique frameworks. The structure of $[Cu(bim)_{2.5}](ClO_4)_2 \cdot 2MeOH$[105] is constructed from five-coordinate $\{CuN_5\}$ sites linked by bridging bim ligands into a three-dimensional framework. Three ligands on each Cu^{II} site are approximately planar and link to adjacent sites to form hexagonal two-dimensional sheets, which are linked above and below by the remaining bim ligands to form the framework (Figure 30).

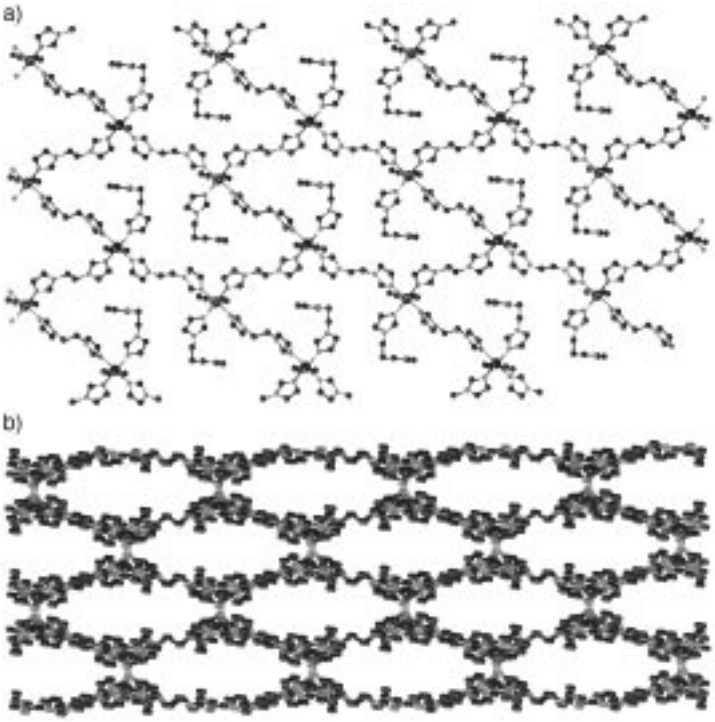

Figure 30. a) A view of the layer motif of $[Cu(bim)_{2.5}](ClO_4)_2 \cdot 2MeOH$. $\{Cu(bim)\}^{2+}$ chains are cross-linked in the *ac* plane to give a two-dimensional network. Each Cu^{II} site is coordinated to an additional bim ligand that projects above or below the plane and links each network to adjacent networks. (b) A view of the large cavities produced by the covalent linkage of the three-dimensional $\{Cu(bim)_{2.5}\}^{2+}$ framework. The ClO_4^- anions and methanol molecules occupy these cavities.

The Mn^{II} site of $[Mn(bbi)_3](BF_4)_2$[106] adopts octahedral $\{MnN_6\}$ geometry, which results in a three-dimensional framework constructed from linked $\{Mn_8(bbi)_{12}\}$ rhombohedral boxes (Figure 31). In common with the majority of such structures, two independent arrays interpenetrate to form cavities occupied by the BF_4^- anions.

Not only are the coordination preferences of the metal center important determinants of structure, but anion coordination or geometry may also dramatically influence the geometry and dimensionality of such solids. An interesting example is provided by the structures of $[Ag(pytz)(NO_3)]$ and $[Ag(pytz)(MeCN)](PF_6)$. The structure of $[Ag(pytz)(NO_3)]$[91] (Figure 32) consists of one-dimensional $[Ag(pytz)]^+$ chains linked by NO_3^- bridges into a three-dimensional framework with a helical motif along the 6_1 screw axis of the structure. In contrast, in the presence of a weakly coordinating anion in $[Ag(pytz)(MeCN)](PF_6)$, a one-dimensional structure, based on $\{Ag(pytz)\}^+$ double chains linked by weak Ag $\cdots$ Ag interactions, is observed (Figure 33).

The structures of $[Ag(py_2urea)_2](BF_4)$ and $[Ag(py_2oxalamide)_2](NO_3)$[95] provide examples of three-dimensional frameworks where the Ag $\cdots$ Ag distances are determined by the hydrogen-bonded frameworks of the ligand backbones. Both structures consist of tetrahedral Ag sites interconnected through the extended bipyridyl ligands. The most remarkable

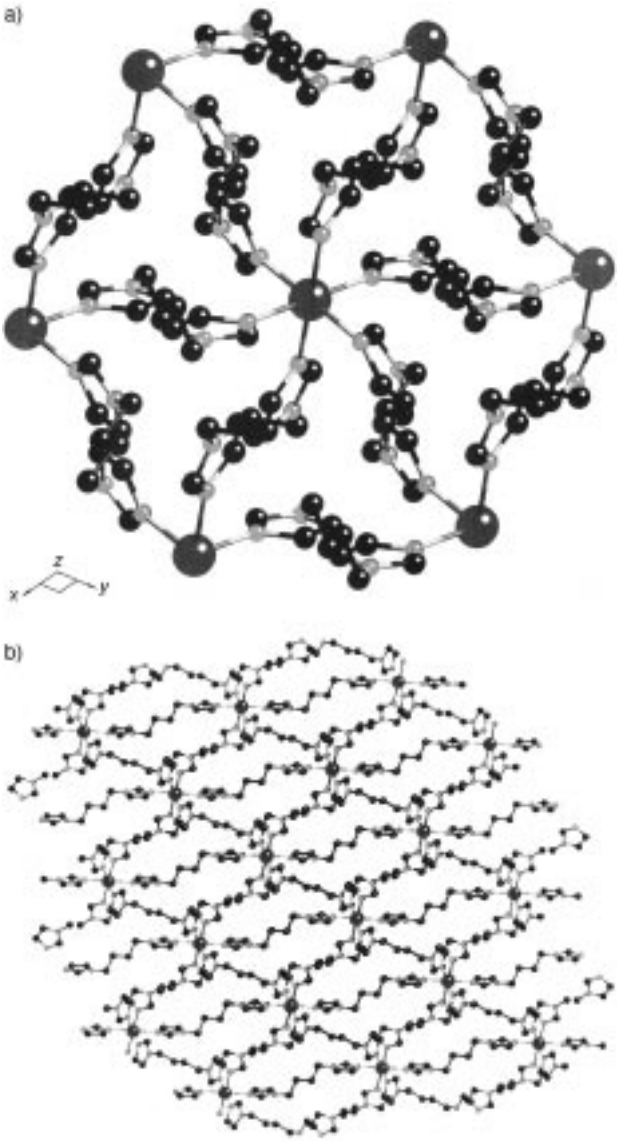

Figure 31. a) The rhombohedral array produced by the octahedral geometry at the $\{MnN_6\}$ site of $[Mn(bbi)_3](BF_4)_2$. b) A view of the three-dimensional structure, to show the effects of interpenetration.

feature of the structures is the presence of one-dimensional α networks of pyridine-substituted ureas and oxalamides, respectively, whose hydrogen-bonding interactions determine the Ag···Ag spacings.

3.4. Coordination Polymers Constructed from Three-Connected Ligands

The structures based on the three-connected pyridyl donor ligand 2,4,6-tri(4-pyridyl)-1,3,5-triazine exhibit geometries that reflect metal coordination preference and influence of coligands. The structure of $[Cu_3(tpt)_4](ClO_4)_3$[110] consists of $\{CuN_4\}$ sites linked into a three-dimensional framework. While there are two interpenetrating frameworks, neither intrudes into the large octahedral cavity of the other (Figure 34). Consequently, the structure exhibits considerable void volume.

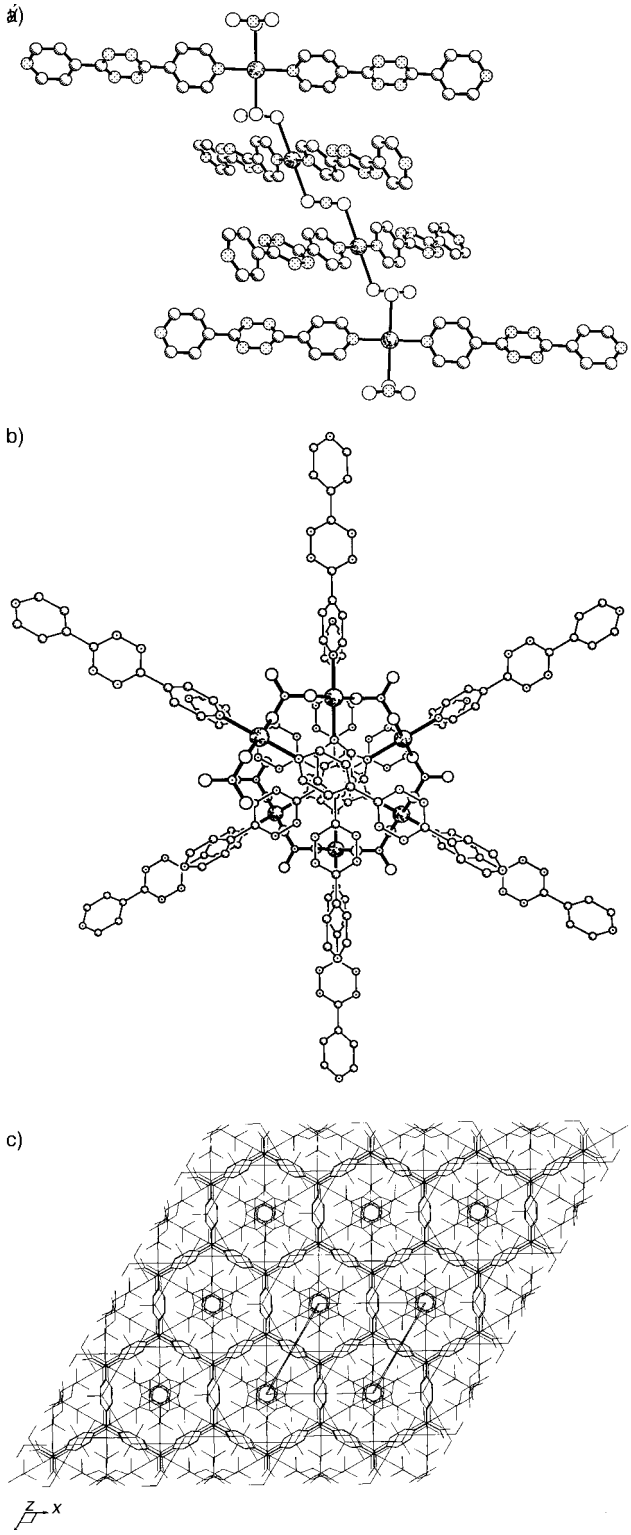

Figure 32. a) The linkage of $\{Ag(pytz)\}^+$ chains by NO_3^- bridges in $[Ag(pytz)(NO_3)]$. Each chain is rotated by 60° relative to its neighbors. b) A view down the helical axis with the Ag–NO_3 units highlighted to show the hexagonal channels. c) A view of the packing to illustrate the elegant symmetry of the structure.

Figure 33. The double chain structure of $[Ag(pytz)(MeCN)](PF_6)$.

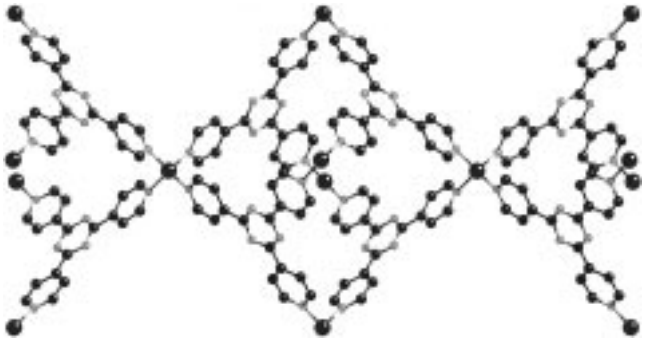

Figure 34. A view of one of the large chambers in $[Cu_3(tpt)_4](ClO_4)_3$, formed by the linkage through tpt groups of six Cu^I centers at the vertices of a regular octahedron.

In contrast, the Hg^{II} site of $[Hg(tpt)_2](ClO_4)_2 \cdot 6\,C_2H_2Cl_4$[111] exhibits octahedral $\{HgN_6\}$ coordination, to produce a three-dimensional framework with no interpenetration. These large intraframework cavities are occupied by $C_2H_2Cl_4$ molecules. The absence of interpenetration is reflected in the solvent molecule:Hg ratio of 6:1 and the spaciousness of the cavities.

The presence of CN^- coligands contributes to the unusual structure of $[Zn(CN)(NO_3)(tpt)_{2/3}] \cdot 0.75\,C_2H_2Cl_4 \cdot 0.75\,CH_3OH$[112] (Figure 35). The structure is constructed from $\{Zn_4(CN)_4(NO_3)_4\}$ squares linked through tpt ligands into a three-dimensional structure with two distinct cage types. There are two interpenetrating frameworks aligned such that the smaller cages are encapsulated within the larger cages, which results in large chambers surrounded by double shells. The cages are somewhat reminiscent of those observed in sodalite minerals but are considerably more spacious and accommodate approximately nine molecules each of $C_2H_2Cl_4$ and MeOH.

3.5. Coordination Polymers with Pyrazine and Pyrimidine as Ligands

Nitrogen heterocycles with two nitrogen donors, such as diazoles and diazines, often act as *exo*-bidentate ligands in the isolation of oligomeric and polymeric metal complexes.[109, 114] Such systems have been extensively investigated for properties such as electrical conductivity, magnetism, and photochemistry.[90] The complexes of pyrazine and pyrimidine reveal the representative structural patterns. With respect to the structural systematics of polymeric coordination complexes, pyrazine and pyrimidine contrast with the ligands of Sections 3.2–3.4: The distance between donor groups is contracted by the adoption of pyrazine as the linker ligand, while the donor group disposition is altered by the use of pyrimidine.

3.5.1. One-Dimensional Coordination Polymers of Pyrazine and Pyrimidine

A prototypical structure is adopted by $[Cd(pz)Cl_2]$[120] (Figure 36). Linear $\{Cd(pz)\}^{2+}$ chains are linked by bridging chlorides into planar two-dimensional sheets. The influence of donor-group disposition is revealed in the structure of the

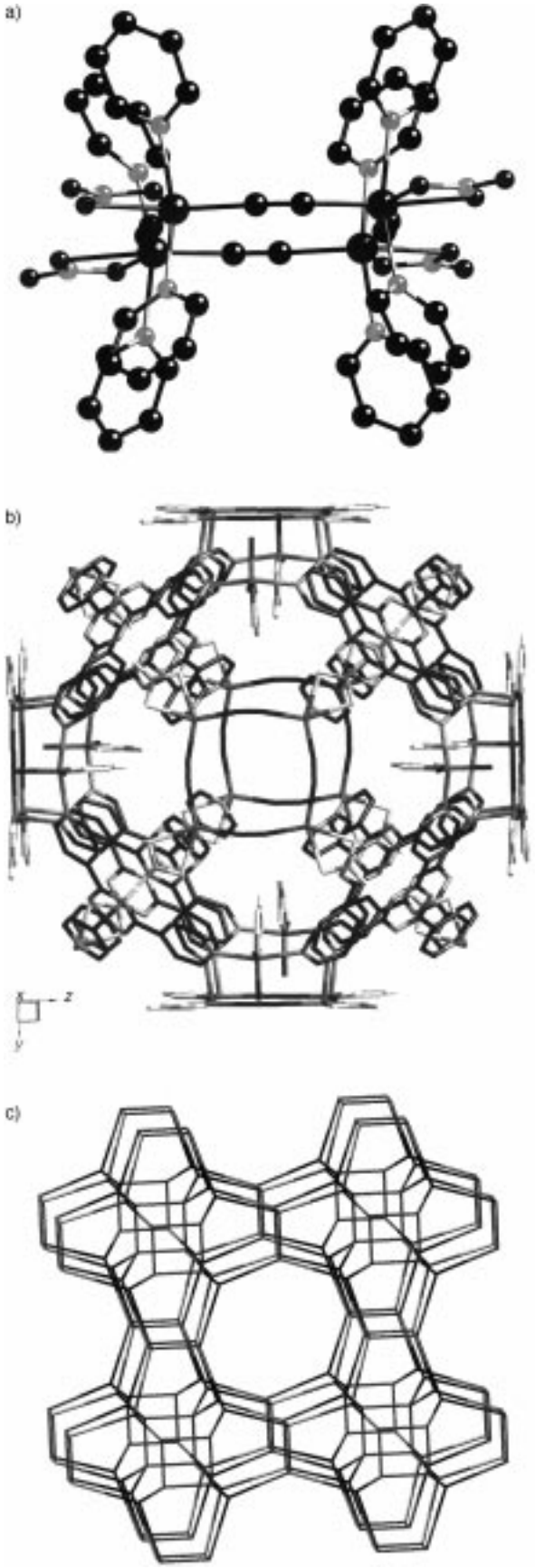

Figure 35. a) The $\{Zn_4(CN)_4(NO_3)_4(tpt)_{8/3}\}$ unit which provides the fundamental building block of $[Zn(CN)(NO_3)(tpt)_{2/3}]$. b) A view of the structure of one of the smaller A-type cages. c) Part of the infinite three-dimensional framework, showing eight A-type cages surrounding a central cavity.

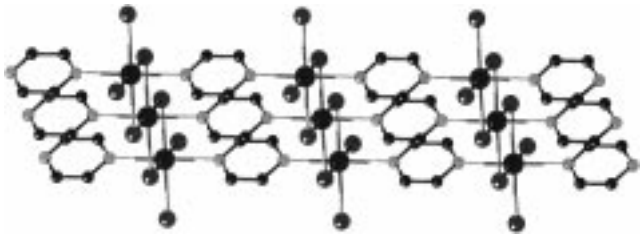

Figure 36. The layer structure of $[Cd(pz)Cl_2]$.

pyrimidine derivative $[Zn(pyrd)Cl_2]$[120] where the {Zn(pyrd)} sheets are linked through Cl bridges into undulating sheets.

The structural influence of substituents is discerned in the structure of $[Cu(pzca)(Me_2CO)_{0.5}](BF_4)$,[122] which consists of one-dimensional $\{Cu(pzca)(Me_2CO)\}^+$ chains linked by bridging pzca molecules into a three-dimensional helical framework (Figure 37). This arrangement generates a stacked two-dimensional hexagonal array with channels occupied by BF_4^- anions.

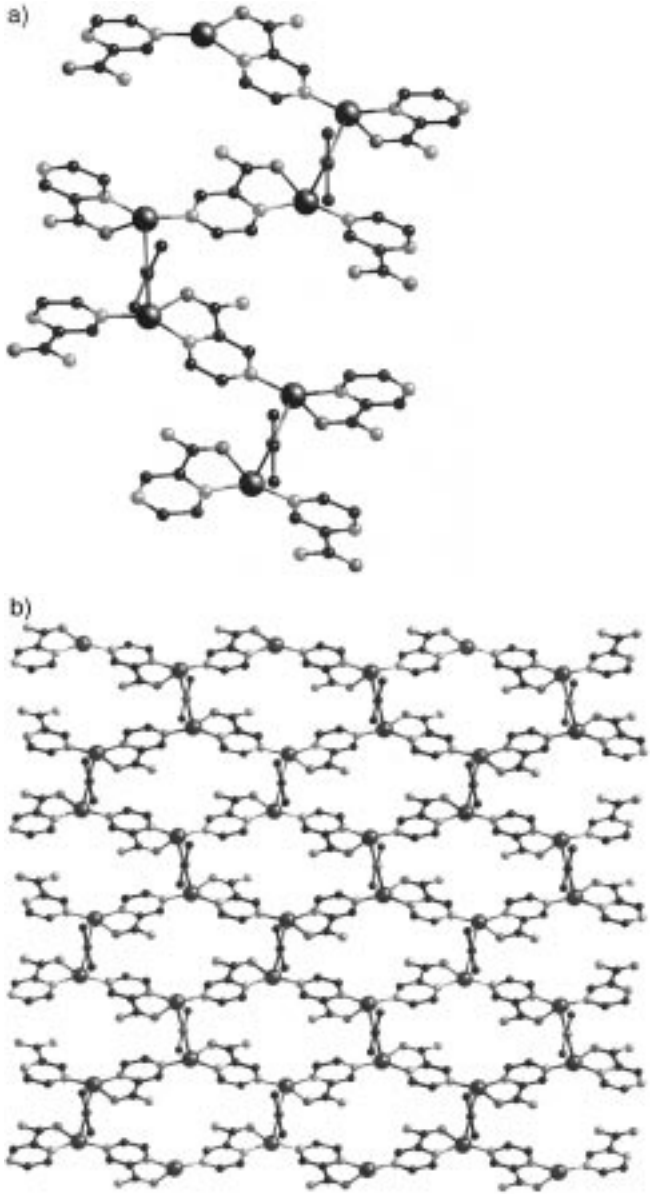

Figure 37. a) A portion of the helical $\{Cu(pzca)(Me_2CO)\}^+$ chains of $[Cu(pzca)(Me_2CO)_{0.5}](BF_4)$. b) The hexagonal channels formed by the three-dimensional covalently linked framework.

3.5.2. Two-Dimensional Coordination Polymers of Pyrazine

Once again, there are no obvious structural prototypes and the details of the networks reflect the metal coordination geometry or ligand influences. The structure of $[Cu_2(pz)_3](SiF_6)$[82] consists of trigonal $\{CuN_3\}$ sites linked by pyrazines into a two-dimensional honeycomb grid of fused $\{Cu_6(pz)_6\}$ rings (Figure 38). Two grids interpenetrate and SiF_6^{2-} anions

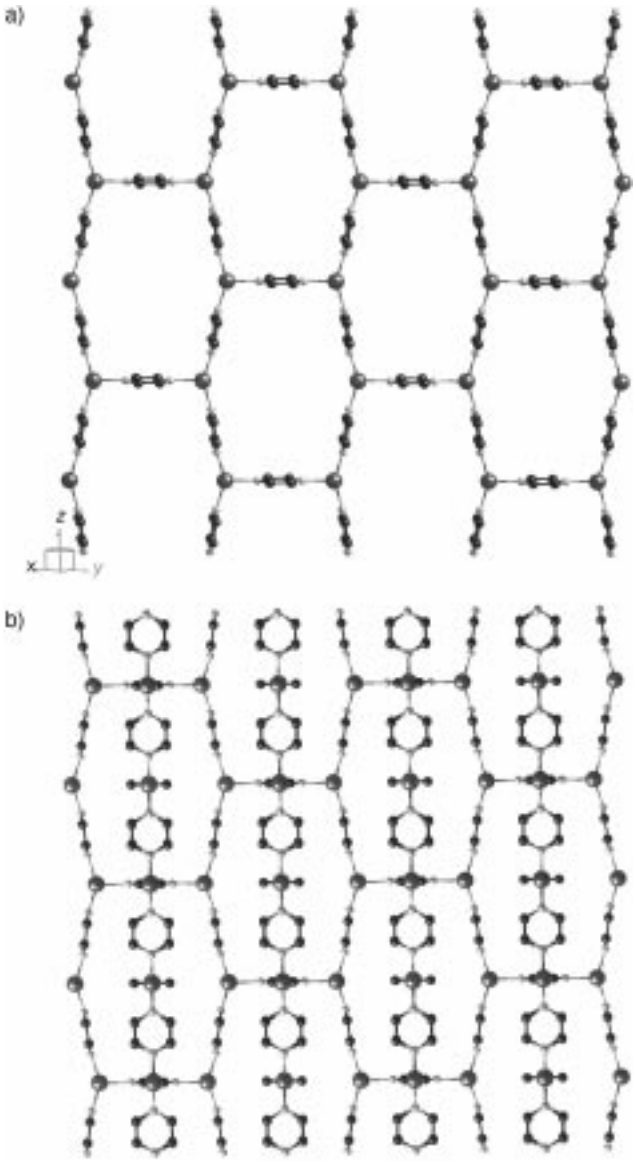

Figure 38. a) The two-dimensional honeycomb grid of $[Cu_2(pz)_3](SiF_6)$. b) A view of the interpenetration of two independent grids.

occupy the generated cavities. In contrast, $[Ag(pz)_2](PF_6)$[125] exhibits a structure constructed from $\{Ag_6(pz)_7\}$ bicyclic folded rings fused into two-dimensional pleated sheets (Figure 39).

The structure of $[Ag(pz)_2][Ag_2(pz)_5](PF_6)_3$[126] may simply reflect changes in reaction conditions, a dramatic demonstration of the structural variability of these solids. The structure contains two distinct layer motifs. The first is the common square grid based on fused $\{Ag_4(pz)_4\}$ rings; the second is

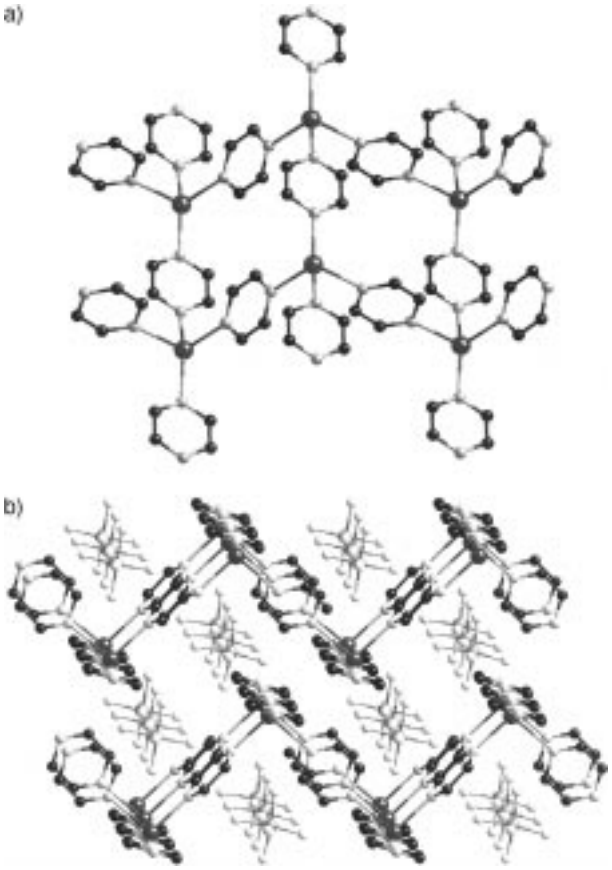

Figure 39. a) The building block for the sheet structure of $[Ag(pz)_2](PF_6)$. b) A view along the *a* axis of the undulating sheets and of the PF_6^- anions that occupy the interlamellar regions.

constructed from two parallel sheets of such square grids linked by perpendicular pyrazine ligands into a double layer. The coordination geometries of the Ag sites are $\{AgN_4\}$ square planar for the former motif and $\{AgN_5\}$ square pyramidal for the second. Single and double layers are mutually parallel and alternate in an ABAB sequence.

The structure of $[Cu_2(pzca)_3](ClO_4)_2 \cdot 2Me_2CO$[122] exhibits a two-dimensional structure constructed from fused hexagonal rings of four- and five-coordinate Cu^+ sites bridged by tridentate pyrazinecarboxamide ligands (Figure 40).

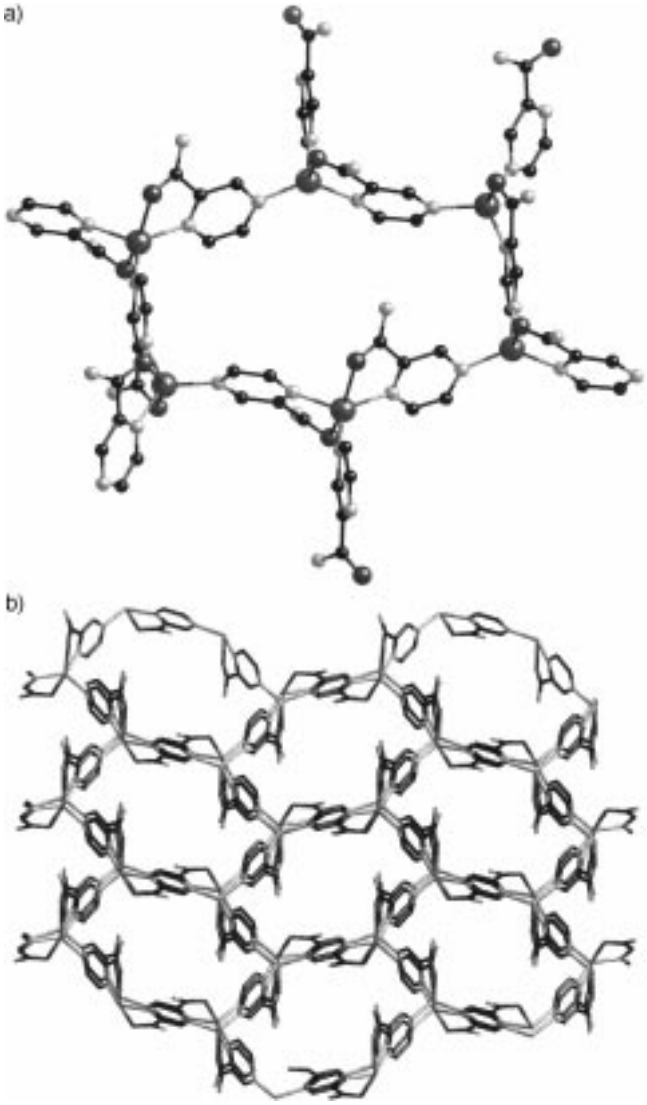

Figure 40. a) The hexagonal array of ligands at the copper centers. b) The layer structure of $[Cu_2(pzca)_3](ClO_4)_2 \cdot 2Me_2CO$.

3.5.3. Three-Dimensional Coordination Polymers of Pyrazine and Pyrimidine

It is curious that $[Ag(pz)_3](SbF_6)$[126] exhibits a simple structure based on $\{AgN_6\}$ octahedra linked into a cubic three-dimensional framework (Figure 41), topologically related to ReO_3, while $[Ag(pz)_2][Ag_2(pz)_5](PF_6)_3 \cdot 2Sol$ exhibits a structure composed of alternating $\{Ag(pz)_2\}^+$ single layers and $\{Ag_2(pz)_5\}^{2+}$ double layers with PF_6^- anions occupying both interlayer regions and channels within the double layers (Figure 41 b). The topological relationship of this structure to those of α-polonium and ReO_3 have been discussed.[126] The structural relationship of numerous frameworks of the types presented in this review to structural prototypes have been discussed extensively by Ciani and co-workers.[108, 113] In contrast to the Ag–pyrazine structures cited above, the structure $[Ag_2(2,3\text{-}Me_2pz)_3](SbF_6)_2$[133] (Figure 42) consists of zigzag $\{AgN_2\}$ chains cross-linked by bridging dimethylpyrazine ligands into an enantiomorphic three-dimensional framework.

The pyrimidine derivative $[Cu(pyrd)_2](BF_4)$[134] exhibits a noninterpenetrated structure constructed from tetrahedral $\{CuN_4\}$ sites linked by pyrimidine bridges. The distinctive channels which are characteristic of the structure are shown in Figure 43.

3.6. Coordination Polymers with Hexamethylenetetramine as Linker Ligand

Although hmta is potentially a tetradentate ligand, the structures reported to date exhibit both three- and four-connected geometries. Thus, the structure of $[Ag(hmta)](ClO_4)$[136] is constructed of three-connected Ag^I and hmta

sites resulting in $\{Ag_3(hmta)_3\}$ rings fused into a two-dimensional sheet (Figure 44). The structure of $[Ag_3(hmta)_2](ClO_4)_3 \cdot 2H_2O$[136] shares this trigonal sheet motif. However, the layers are linked by digonal Ag^+ cations, which are coordinated to the hmta nitrogen donors that project into the interlamellar region. The anions and solvent molecules occupy the large hexagonal channels.

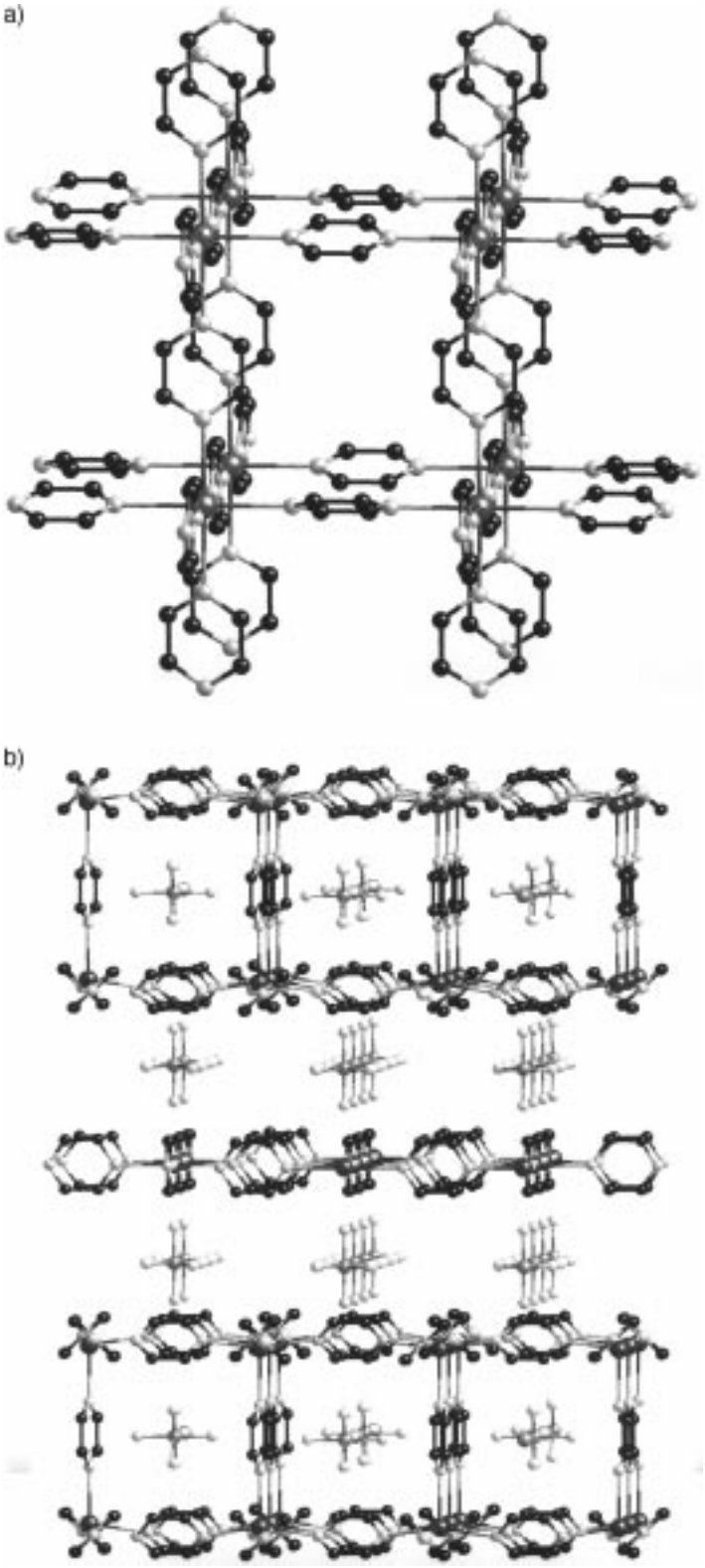

Figure 41. a) The simple cubic three-dimensional framework of $[Ag(pz)_3](SbF_6)$. b) A view of the structure of $[Ag(pz)_2][Ag_2(pz)_3](PF_6)_3$.

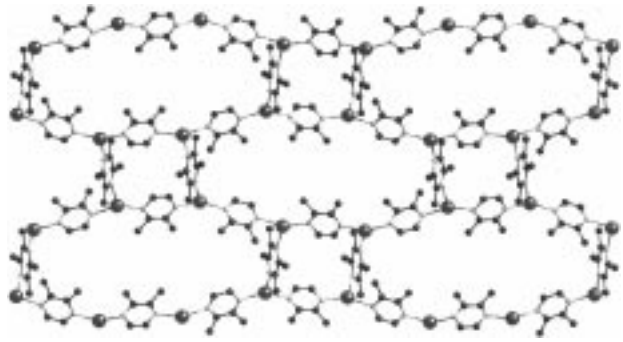

Figure 42. A view down the *a* axis of a single framework of $[Ag_2(2,3\text{-}Me_2pz)_3](SbF_6)_2$.

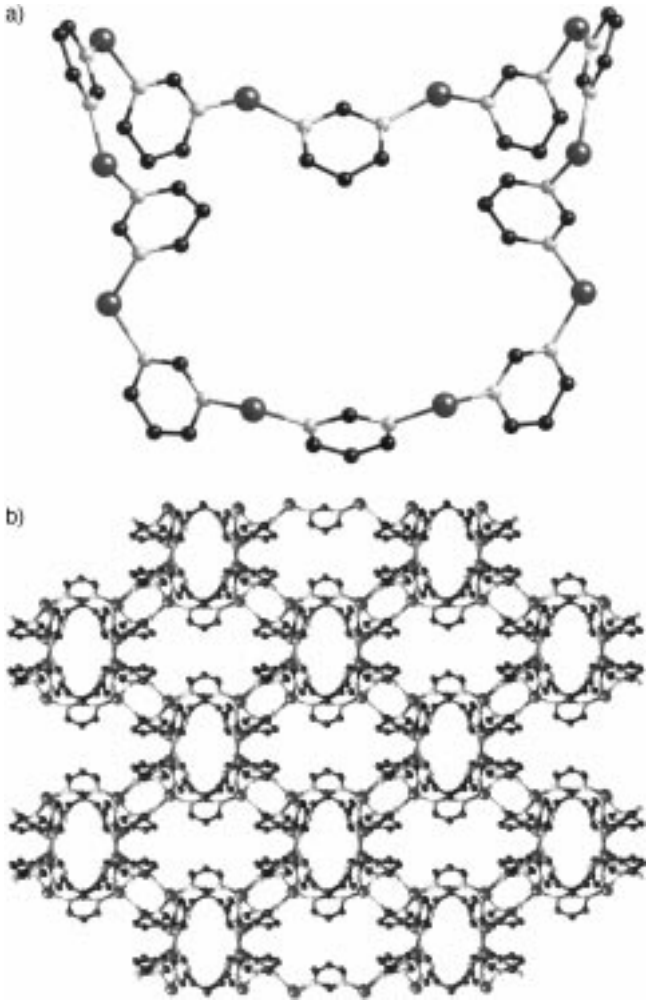

Figure 43. a) The cyclic building block for the structure of $[Cu(pyrd)_2](BF_4)$. b) The channels produced by the framework structure of $[Cu(pyrd)_2](BF_4)$.

In contrast to the above, the structure of $[Ag(hmta)](PF_6) \cdot H_2O$[138] consists of trigonally flattened $\{AgN_3\}$ sites linked into a three-dimensional helical framework. In contrast also to the structure of $[Ag_2(2,3\text{-}Me_2pz)_3](SbF_6)$, which exhibits a similar framework, there is no interpenetration in $[Ag(hmta)](PF_6) \cdot H_2O$; consequently, the framework is enantiomorphic.

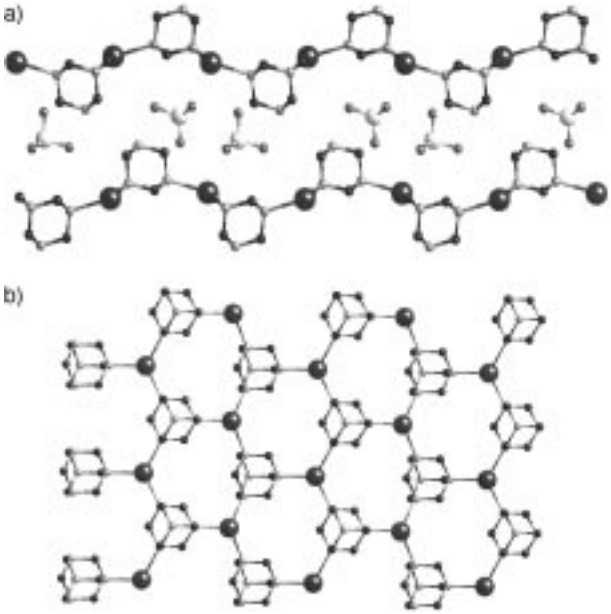

Figure 44. a) The stacking of two-dimensional $\{Ag(hmta)\}_n^{4+}$ layers and interlamellar ClO_4^- anions in $[Ag(hmta)](ClO_4)$. b) A view of a layer to show the three-connected geometries of the Ag^+ cations of the hmta ligands.

Finally, the structure of $[Ag_4(hmta)_3(H_2O)](PF_6)_4 \cdot 3EtOH$[135] exhibits common geometric motifs in a unique structural type. The structure consists of hexagonal $\{Ag_6(hmta)_6\}$ rings, reminiscent of the honeycomb motif of $[Cu_2(pz)_3](SiF_6)$, linked by trigonal $\{AgN_3\}$ centers into a three-dimensional framework. This results in spacious cavities and channels (Figure 45).

3.7. Prelude to Oxides: The Copper Sulfate–Organodiamine Linker System

While the structural chemistry of these coordination polymers is complex and as yet lacking in a totally cohesive overview, certain general principles for guiding their applications to oxide synthesis may be elicited. Most obviously, the coordination polymers described above are cationic and consequently can serve as unique counterions for negatively charged oxide clusters and/or polymers. Depending on the coordination preferences of the metal constituent of the polymer, the polymer chain may also bond to the peripheral oxo groups of the oxide component to provide access to heterometallic oxide–organic hybrid materials. For example, while Cu^I might be expected to form linear polymeric cationic chains with little or no interaction with the oxide surface, the coordination requirements of Mn^{II}, Fe^{II}, Co^{II}, and Ni^{II} would encourage direct interaction with the oxide surface under appropriate conditions.

The architectures adopted by these coordination polymers are suitable both for charge compensation and for a structure-directing role, both for the determination of the oxide dimensionality and the development of the intimate details of connectivity within the oxide skeleton. Within a naive conceptual construct, linear cationic chains could, in principle, thread through the pores of a three-dimensional open frame-

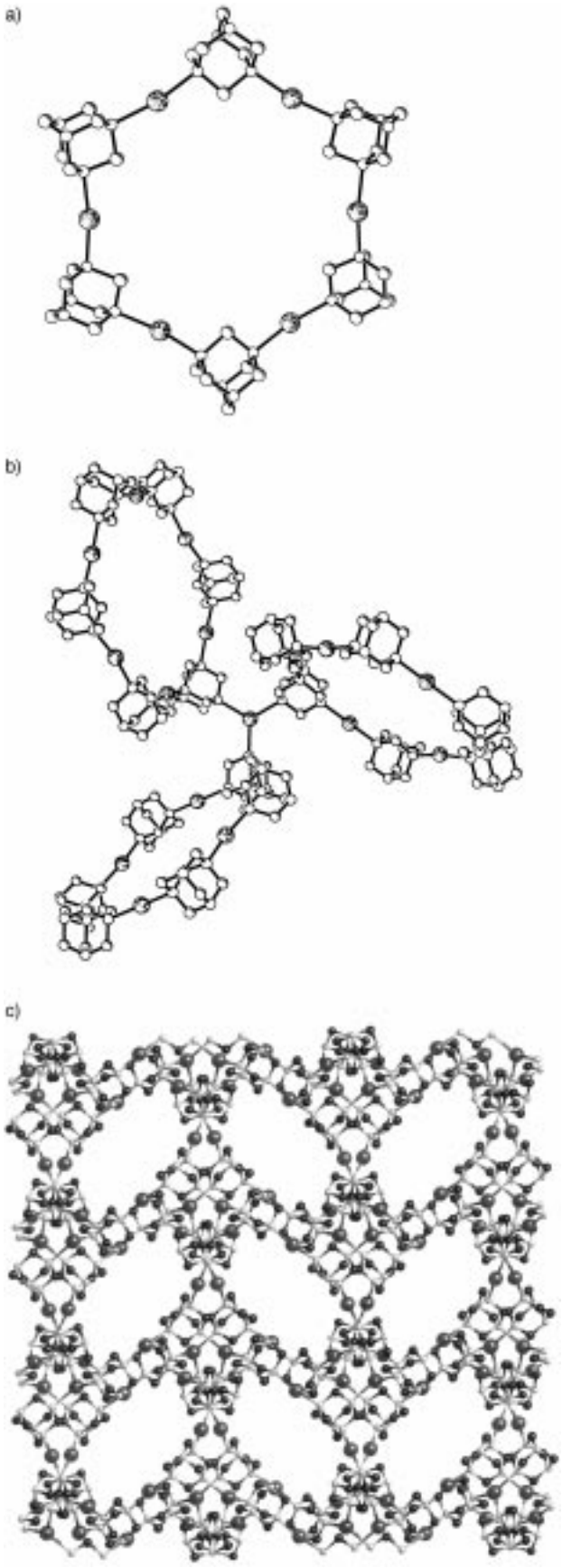

Figure 45. a) The cyclic building block of $[Ag_4(hmta)_3(H_2O)](PF_6)_4 \cdot 3EtOH$. b) The linking of three adjacent rings through the three-coordinate Ag site. c) A packing view along the *c* axis to show the rhombic channels which result from interpenetration.

work oxide or provide a cationic scaffolding to encapsulate clusters or one-dimensional structures. Alternatively, the linear polymeric cation may serve to stitch one- or two-dimensional oxide arrays into two- or three-dimensional covalently linked architectures. The two-dimensional square grid, honeycomb, double layer, or lattice-type polymeric cations may serve to sandwich alternating layers or strings of a negatively charged oxide component. The cavities and tunnels associated with the three-dimensional cationic structures of the adamantoid and other types might allow encryption of polyoxoanions or one-dimensional chains. Furthermore, from a simplistic geometric viewpoint, the introduction of spacers between donor groups of the bridging ligands of the polymeric cations provides spatial expansion and consequently may increase the void volume available to the anionic component. Moreover, expansion or contraction of metal–metal distances within the polymeric cationic moiety determines the periodicity of points of attachment between the heterometal sites of the polymeric cation and the surface of the oxide component in covalently linked composites. It is perhaps also significant that variable tethering of the metal sites of the polymeric cation results in variations in the charge/volume or charge/length ratio of the polymer, a characteristic which is necessarily reflected in the charge density of the oxide component. This observation raises the intriguing possibility of manipulation of the charge/volume ratios of oxides through the choice of cationic template.

However, it must be noted that the void volumes of the coordination polymer structures are often restricted by interpenetration. The interpenetration phenomenon reflects the efficient packing requirements of the crystalline state. Significantly, interpenetration is *not a universal phenomenon*. While there are, to date, insufficient examples to provide reliable guidelines for restricting interpenetration, several observations are relevant:

1) Appropriate coligand geometry can preclude interpenetration, as observed for $[Zn(4,4'\text{-bpy})_2(SiF_6)]\cdot x\,H_2O$.
2) Shortening of the donor–donor distance in the bridging ligand of the polymeric cation results in non-interpenetrating structures for $[Cu(pyrd)_2](BF_4)$, $[Ag(hmta)](PF_6)\cdot H_2O$, and $[Ag_4(hmta)_3(H_2O)](PF_6)_4\cdot 3\,EtOH$.
3) Efficient occupancy of void space by anions and solvent molecules can alleviate the need for interpenetration, as observed for $[Ag(hmta)](PF_6)\cdot H_2O$ and $[Cu(4,4'\text{-bpy})(H_2O)_2(BF_4)_2]\cdot 4,4'\text{-bpy}$.

In this regard, hydrothermal synthesis offers several advantages. Enhancement of the solubility of both organic and inorganic components allows a variety of space-filling entities to be introduced, which are subsequently "selected" in the hydrothermal crystallization. Most specifically, the hydrothermal method favors the encapsulation of water molecules of crystallization which form complex microstructures within the channels or cavities of the oxide array through multipoint hydrogen bonding to the oxide surface and to the proton sites of the cationic component. Furthermore, incorporation of large polyoxoanion clusters or of one- or two-dimensional oxide arrays should provide efficient cation–anion packing to prevent interpenetration of the cationic polymers.

To address the feasibility of oxide incorporation into cationic polymer arrays, the oxoanion sulfate was chosen as a model for a coordinating tetrahedral EO_4^{n-} subunit. Variations of reaction conditions and ligand spacer lengths resulted in the facile preparation of one-, two-, and three-dimensional composite materials.

As shown in Figure 46, the structure of $[Cu(4,4'\text{-bpy})(H_2O)_3(SO_4)]\cdot 2H_2O$[72] (**CUSO-1**) consists of $\{Cu(4,4'\text{-bpy})(H_2O)_3\}_n^{+2n}$ chains running parallel to the *ab* plane. The sulfate anions are weakly coordinated to the copper sites of a chain, and occupy interchain positions to provide the appropriate charge balance. Parallel $\{Cu(4,4'\text{-bpy})(H_2O)_3\}^{2+}$ chains form layers parallel to the *ab* plane and stack along the *c* axis. Adjacent layers are rotated by 60° to produce triangular cavities occupied by the sulfate anions or hexagonal cavities occupied by the ligand rings (Figure 46b).

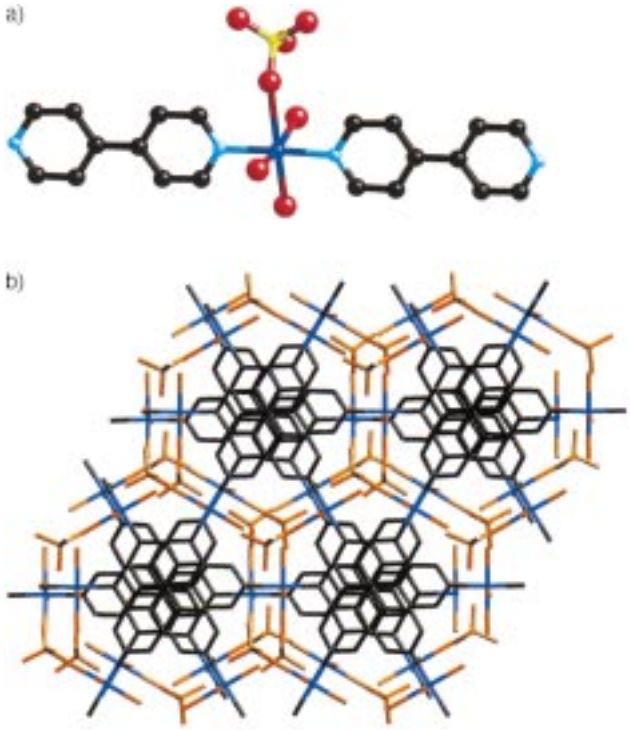

Figure 46. a) The Cu^{II} coordination geometry in $[Cu(4,4'\text{-bpy})(H_2O)_3(SO_4)]\cdot 2H_2O$ (**CUSO-1**). b) A view of the structure down the *c* axis to show the stacking of chains which produces hexagonal cavities, occupied by the rings of the ligand.

One major determinant of structure is the Cu^{II} coordination geometry. The copper site of **CUSO-1** exhibits distorted 5+1 octahedral geometry. The coordination sphere is defined by two pyridyl nitrogen donors from two 4,4′-bpy ligands, three aquo oxygen donors, and the oxygen atom of a sulfate anion. The coordination geometry may be described as a basal plane consisting of the *trans* nitrogen donors and aquo ligands, with axial positions occupied by an aquo group and the oxygen atom of a weakly interacting sulfate.

In contrast, the structure of $[Cu(bpe)_2][Cu(bpe)(H_2O)_2(SO_4)_2]\cdot 2H_2O$ (**CUSO-2**) is constructed from two motifs, a linear one-dimensional chain and a two-dimensional grid, which integrate to generate a unique three-dimensional framework. As shown in Figure 47, the one-dimensional chains consist of distorted octahedral copper sites bridged

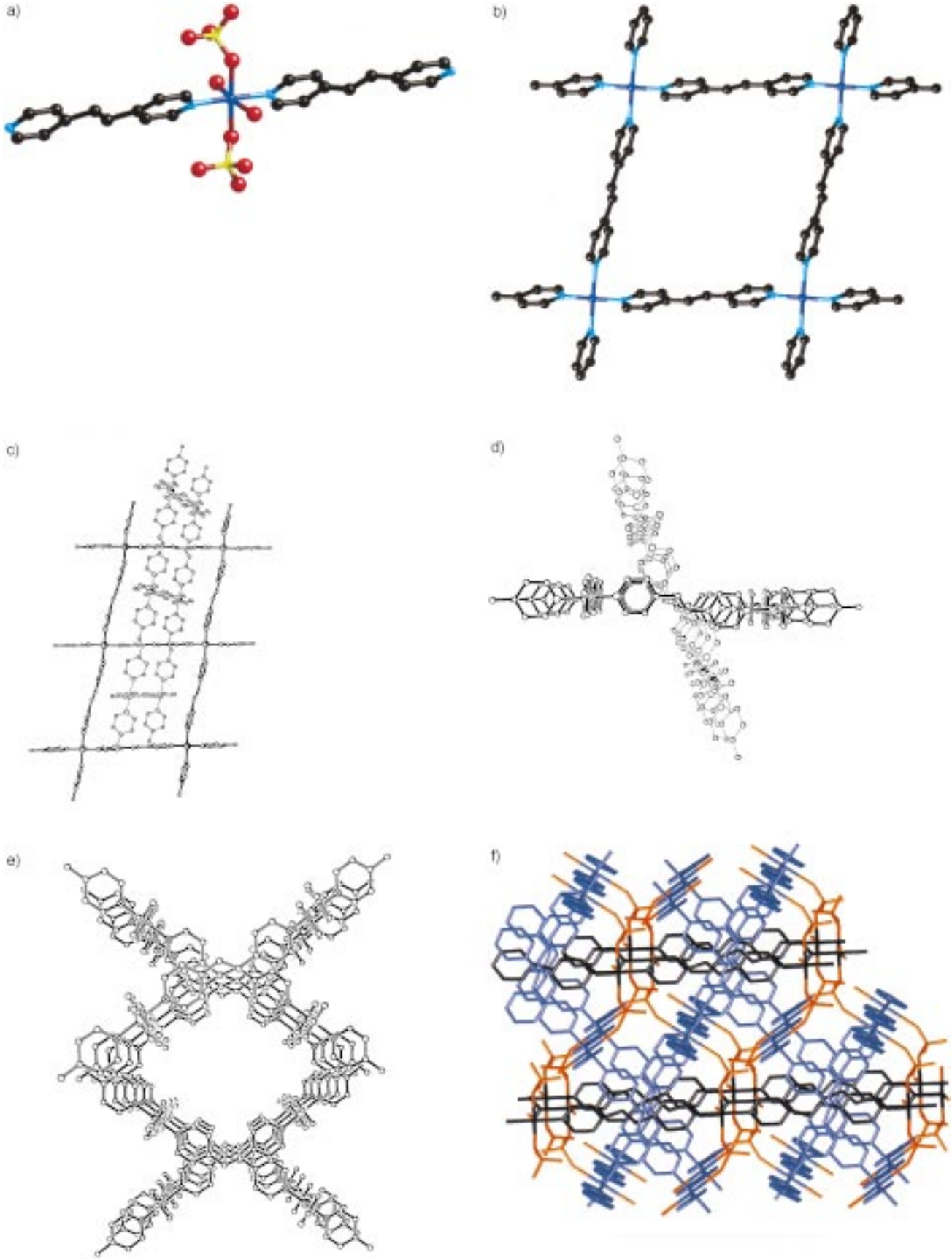

Figure 47. a) A view of one of the one-dimensional copper sites of **CUSO-2**. b) A view of the square grid associated with the second copper site. c), d) Two views of the interpenetration of grids in **CUSO-2**. e) A view parallel to the *c*-axis of the rhombic channels formed by the interpenetration of square grids. f) The threading of the one-dimensional chains through the network of square grids: the two-dimensional grids are in blue, the one dimensional chains in black, and the sulfate groups in orange.

by 4,4′-bpe ligands. Each Cu(1) center adopts $\{CuO_4N_2\}$ coordination geometry, defined by two *trans* pyridyl nitrogen donors from each of two bpe ligands, two aquo oxygen donors, and two oxygen donors from two sulfate groups. The sixfold coordination is best described as 4+2 distorted octahedral geometry. The equatorial plane is defined by two pyridyl nitrogen donors and two sulfate oxygen atoms. The weakly interacting axial positions are occupied by aquo ligands. Thus, in contrast to the structure of **CUSO-1**, the Cu–sulfate oxygen bonds are proximal while the Cu–aquo bonds are distal.

The second structural building block is the two-dimensional square grid pattern adopted by the $\{Cu(bpe)\}^{2+}$ chains of the Cu(2) sites. The proximal coordination at the Cu(2) centers consists of square planar $\{CuN_4\}$ units, with each Cu(2) bonded to four nitrogen donors from four bpe ligands, to produce the grid work pattern of Figure 47 b. These layers are propagated parallel to the crystallographic *ab* and *bc* planes to interweave as shown in Figure 47 c. In addition to the four nitrogen donors from the bpe ligands, each Cu(2) center participates in weak axial coordination to oxygen donors from sulfate groups of two adjacent one-dimensional chains associated with the Cu(1) sites. Consequently, the geometry of the Cu(2) centers is also best described as 4+2 distorted octahedral.

The one-dimensional chains are thus linked through weak sulfate bridges to the interpenetrating two-dimensional grids (Figure 47 d). These chains thread through the two-dimensional networks to produce the unique and complicated three-dimensional framework shown in Figure 47 e. The cross-linking of two-dimensional grids through interpenetrating one-dimensional chains is a unique feature of the structure.

The structure of $[Cu(bpe)(H_2O)(SO_4)]$ (**CUSO-3**) is constructed from one-dimensional $\{Cu(bpe)(H_2O)\}^{2+}$ chains linked through bridging sulfate groups into a three-dimensional framework. As shown in Figure 48, the chains consist of square-pyramidal Cu sites linked through bpe ligands. The geometry about the Cu sites is defined by *trans* nitrogen donors from two bpe ligands and two sulfate oxygen donors in

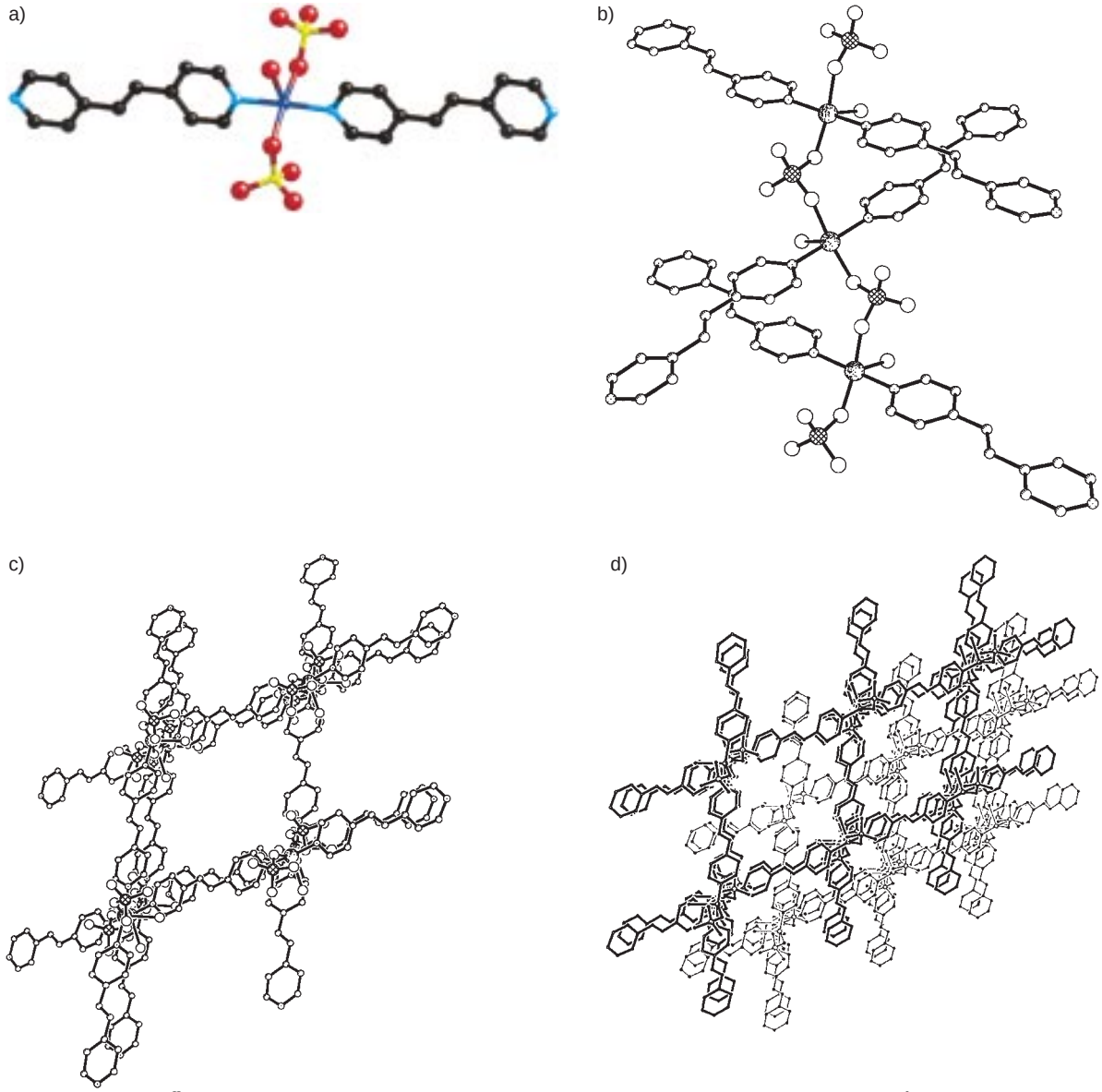

Figure 48. a) The Cu^{II} geometry in **CUSO-3**. b) A view of the undulating $\{Cu(SO_4)\}$ chain which links $\{Cu(bpe)\}^{2+}$ linear chains. c) A view along the [101] direction to show the rhombic grid of the three-dimensional framework. d) A view of the interpenetration of the two independent three-dimensional grids.

the equatorial plane, with an aquo ligand in the axial position. A copper center of a given chain is linked to copper sites from two adjacent chains through bridging sulfate groups. Each sulfate bridges copper centers from two neighboring chains by adoption of a μ^2-bridging mode. This connectivity results in a three-dimensional framework of linked chains shown in Figure 48c. **CUSO-3** illustrates the diversity of coordination environments adopted by copper sites in copper-bridging diamine composite solids, which can exhibit coordination numbers ranging from 2 to 6.

The structural versatility of the composites constructed from cationic polymers and a simple oxoanion encouraged us to substitute molybdate for sulfate in the synthesis, which led to the isolation of the original member of the family of organoamine-heterometallic-molybdenum oxide composites [Cu(bpe)(MoO_4)] (**MOXI-1**).[141]

The structure of **MOXI-1** is constructed from $\{Cu(bpe)\}^{2+}$ linear chains bridged through $\{MoO_4\}^{2-}$ tetrahedra into a three-dimensional framework. The fundamental structural motif (Figure 49a) consists of distorted trigonal bipyramidal Cu^{II} centers coordinated to two bpe ligands and three molybdate tetrahedra. The geometry at the Cu sites is defined by three oxygen donors from three $\{MoO_4\}^{2-}$ groups in the equatorial plane and two bpe nitrogen donors that occupy the axial positions. Each molybdate group bridges three neighboring Cu sites to produce a bimetallic oxide layer motif $\{CuMoO_4\}$ (Figure 49b). Each molybdenum site thus possesses one pendant terminal oxo group, which is directed above or below the plane. The connectivity in the plane generates twelve-membered $\{Cu_3Mo_3O_6\}$ rings which fuse to propagate the layer structure. The bpe ligands extend from the metal oxide layers at an angle of ca. 35° and bridge adjacent layers to generate the overall three-dimensional covalent connectivity (Figure 49c). The structural changes engendered by the replacement of sulfate in **CUSO-3** with molybdate in **MOXI-1** are significant. The sulfate groups adopt μ^2 modality, while the molybdates act as μ^3 bridges. The sulfate covalent attachment restricts the $\{CuSO_4\}$ motif to chains, in contrast to the layer structure adopted by the $\{CuMoO_4\}$ moiety of **MOXI-1**. It is noteworthy that the molybdate component not only displays variable points of attachment to the cationic array but may also aggregate into polyanion clusters or chains, sheets and frameworks to generate an expansive structural chemistry.

4. Organodiamine–Molybdenum Oxide Composite Materials

The cationic coordination polymers described in Section 3 represent one approach, albeit the structurally most novel and unique, to composite oxide phases. However, the organic component may adopt other structure-directing roles, as noted in Section 2.2. For convenience of classification, the MOXI class of composite materials has been divided into three subclasses based on the role of the organodiamine as a protonated cation, as a ligand to a molybdenum site of the oxide array, or as a ligand to a heterometallic site which may be part of a cationic coordination polymer or simply a mononuclear site associated with the molybdenum oxide array (Table 3).

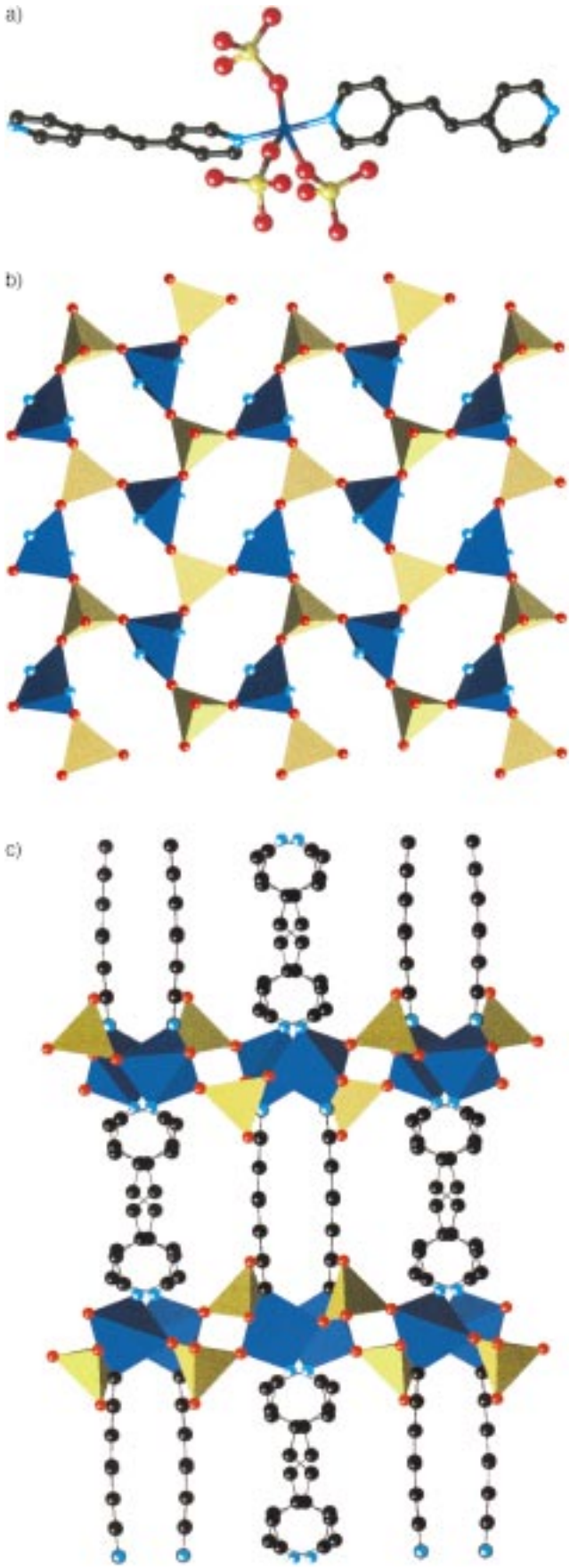

Figure 49. a) The Cu^{II} geometry in **MOXI-1**. b) The $\{CuMoO_4\}$ layer. c) A view of the alternating inorganic oxide layer–organic linker structure adopted by **MOXI-1**.

Table 3. Selected structural information for organic–inorganic hybrid materials of the organodiamine molybdenum oxide family.

Compound[a]	Mo oxide skeletal structure	Structure: metal coordination	Structure: description	Figure	Ref.
A. organic subunit incorporated as organoammonium cation					
$[H_2en][Mo_3O_{10}]$ (**MOXI-2**)	1D	$\{MoO_6\}$	1D chains of edge-, corner-, and face-sharing octahedra	50	[142]
$[H_3N(CH_2)_6NH_3][Mo_4O_{13}]$	1D	$\{MoO_6\}$	$\{Mo_8O_{26}\}^{4-}$ clusters constructed of edge-sharing octahedra, linked by corner-sharing into 1D chains	50	[143]
$[4,4'\text{-}H_2bpy][Mo_7O_{22}]\cdot H_2O$ (**MOXI-3**)	2D	$\{MoO_6\}$	edge- and corner-sharing octahedra producing a stepped 2D motif	51	[146]
B. organodiamine as ligand coordinated to Mo oxide skeleton					
$[MoO_3(2,2'\text{-bpy})]$ (**MOXI-4**)	1D	$\{MoO_4N_2\}$	corner-sharing $\{MoO_4N_2\}$ octahedra forming 1D chain	52	[148]
$[Mo_2O_6(2,2'\text{-bpy})]$ (**MOXI-5**)	1D	$\{MoO_4\}$ and $\{MoO_4N_2\}$	alternating corner-sharing $\{MoO_4\}$ tetrahedra and $\{MoO_4N_2\}$ octahedra in 1D chain	52	[148]
$[Mo_3O_9(2,2'\text{-bpy})_2]$ (**MOXI-6**)	1D	$\{MoO_4\}$ and $\{MoO_4N_2\}$	corner-sharing repeat of two $\{MoO_4N_2\}$ octahedra and one $\{MoO_4\}$ tetrahedron	52	[148]
$[Mo_4O_{13}(Hbpa)_2]$ (**MOXI-7**)	$\{MoO_5N\}$	$\{MoO_5\}$	1D chain of edge- and corner-sharing $\{MoO_5N\}$ octahedra and $\{MoO_5\}$ distorted square pyramids; the pendant protonated pyridyl N groups hydrogen bond to adjacent chains to form a 2D sheet	53	[149]
$[Mo_2O_6(bpp)]$ (**MOXI-31**)	1D	$\{MoO_4N_2\}$	1D chains of corner sharing Mo-octahedra linked by bpp ligands into a double chain	–	[150]
$[MoO_3(4,4'\text{-bpy})_{0.5}]$ (**MOXI-8**)	2D	$\{MoO_5N\}$	2D sheets constructed of fused $\{Mo_4O_4\}$ square grids; the sheets are linked by 4,4′-bpy ligands into a 3D covalent framework	54	[151]
$[HMo_2O_6(4,4'\text{-bpy})]$ (**MOXI-9**)	2D	$\{MoO_5N\}$	as for $\{MoO_3(4,4'\text{-bpy})\}$; one of four bridging oxo groups is protonated to render a mixed-valence material mixed	55	[151]
$[Mo_2O_6(Htrz)]$ (**MOXI-32**)	2D	$\{MoO_5N\}$	2D sheets of corner-sharing Mo octahedra with two-connected bridging Htz ligands projecting into the interlamellar space	–	[150]
C. organodiamines as ligands to heterometals					
$[\{Ni(2,2'\text{-bpy})_2\}_2Mo_4O_{14}]$	cluster	$\{MoO_4\}$ and $\{NiO_2N_4\}$	Two $\{Mo_2O_7\}^{2-}$ units linked by two $\{Ni(4,4'\text{-bpy})_2\}^{2+}$ groups into a $\{Mo_4Ni_2O_6\}$ ring	–	[171]
$[\{Cu(o\text{-phen})_2\}_2Mo_8O_{26}]$ (**MOXI-27**)	cluster	$\{MoO_4\}$, $\{MoO_6\}$, $\{CuON_4\}$	α-$[Mo_8O_{26}]$ cluster with peripheral corner-sharing $\{CuON_4\}$ square pyramids	56	[150]
$[Ni(2,2'\text{-bpy})_2Mo_4O_{13}]$ (**MOXI-10**)	$[Mo_8O_{26}]^{4-}$ cluster	$\{MoO_6\}$ and $\{NiO_2N_4\}$	β-$[Mo_8O_{26}]^{4-}$ clusters linked by $\{Ni(4,4'\text{-bpy})_2\}^{2+}$ bridges into a 1D chain	57	[172]
$[\{Cu(en)_2\}_2Mo_8O_{26}]$ (**MOXI-11**)	$[Mo_8O_{26}]^{4-}$ cluster	$\{MoO_5\}$, $\{MoO_6\}$, and $\{CuO_2N_4\}$	γ-$[Mo_8O_{26}]$ clusters linked by $\{Cu(en)_2\}^{2+}$ groups into a 2D sheet	59	[170]
$[\{Cu(4,4'\text{-bpy})\}_4Mo_8O_{26}]$ (**MOXI-12**)	$[Mo_8O_{26}]^{4-}$ cluster	$\{MoO_4\}$, $\{MoO_6\}$, and $\{CuN_2\}$ with two additional weak $Cu\cdots O$ interactions	δ-$[Mo_8O_{26}]^{4-}$ clusters encapsulated in a matrix of linear $\{Cu(4,4'\text{-bpy})\}^{+}$ polymeric rods	60	[177]
$[\{Cu(bpe)\}_4Mo_8O_{26}]$ (**MOXI-13**)	$[Mo_8O_{26}]^{4-}$ cluster	$\{Mo_4\}$, $\{Mo_6\}$, and $\{CuN_2\}$ with two additional weak $Cu\cdots O$ interactions	α-$[Mo_8O_{26}]^{4-}$ clusters linked by $\{Cu(bpe)\}^{+}$ polymeric rods	–	[178]
$[\{Ni(4,4'\text{-bpy})_2(H_2O)_2\}_2Mo_8O_{26}]$ (**MOXI-14**)	$[Mo_8O_{26}]^{4-}$ cluster	$\{MoO_5\}$, $\{MoO_6\}$, and $\{NiO_3N_3\}$	ε-$[Mo_8O_{26}]^{4-}$ linked to 1D $\{Ni(4,4'\text{-bpy})_2\}^{2+}$ chains to form a 2D network	62	[177]
$[\{Cu(pyrd)\}_4Mo_8O_{26}]$ (**MOXI-34**)	$[Mo_8O_{26}]^{4-}$	$\{MoO_6\}$, $\{MoO_5\}$, $\{CuN_2O_2\}$	γ-$[Mo_8O_{26}]^{4-}$ clusters bridged by $\{Cu_4(pyrd)_4O_6\}$ units into a 2D sheet	61	[178]
$[\{Cu_3(4,7\text{-phen})_3\}_2Mo_{14}O_{45}]$ (**MOXI-15**)	$[Mo_8O_{26}]^{4-}$ and $[Mo_6O_{19}]^{2-}$ clusters	$\{MoO_6\}$, $\{CuN_2\}$, $\{CuN_2O\}$, $\{CuN_2O_2\}$	β-$[Mo_8O_{26}]^{4-}$ and $[Mo_6O_{19}]^{2-}$ linked clusters through $\{Cu_3(4,7\text{-phen})_3\}^{3+}$ rings into a 2D network	63	[179]
$[\{Cu(4,4'\text{-bpy})\}_4Mo_{15}O_{47}]\cdot H_2O$ (**MOXI-16**)	1D	$\{MoO_6\}$, $\{CuN_2\}$	1D chains of edge- and corner-sharing Mo octahedra encapsulated in a matrix of linear $\{Cu(4,4'\text{-bpy})\}$ polymeric rods	64	[177]
$[Cu(2,2'\text{-bpy})Mo_2O_7]$ (**MOXI-17**)	1D	$\{MoO_5\}$, $\{MoO_6\}$, $\{CuO_4N_2\}$	1D chain of edge-sharing octahedra and square pyramids with fused peripheral $\{Cu\ (2,2'\text{-bpy})\}^{2+}$ groups	65	[172]
$[Co(2,2'\text{-bpy})Mo_3O_{10}]$ (**MOXI-18**)	1D	$\{MoO_4\}$, $\{MoO_6\}$, $\{CoO_4N_2\}$	1D chains of Mo edge-sharing octahedra and corner-sharing tetrahedra linked by $\{Co(2,2'\text{-bpy})\}^{2+}$ units into a 2D sheet	66	[172]

Table 3. (Continued)

Compound[a]	Mo oxide skeletal structure	Structure metal coordination	Structure description	Figure	Ref.
$[Cu_2(pyrd)Mo_3O_{10}]$ (**MOXI-19**)	1D	$\{MoO_6\}$ and $\{CuN_3O\}$	1D chains of edge-sharing Mo octahedra linked through $\{Cu_2(pyrd)\}$ groups into a 3D covalent framework; the material is mixed valence	67	[182]
$[Cu(2,2'\text{-bpy})Mo_4O_{13}]$ (**MOXI-30**)	1D	$\{MoO_6\}$ and square-pyramidal $\{CuN_2O_3\}$	1D chain of edge- and corner-sharing $\{MoO_6\}$ octahedra with fused peri- pheral $\{Cu(2,2'\text{-bpy})\}^{2+}$ groups	–	[180]
$[Cu(o\text{-phen})MoO_4]$ (**MOXI-20**)	$[MoO_4]^{2-}$ units	$\{MoO_4\}$ and $\{CuO_3N_2\}$	$\{Mo_2Cu_2O_4\}$ rings fused into a 1D chain	70	[150]
$[MoO_4\{FeCl(2,2'\text{-bpy})\}]$ (**MOXI-21**)	$[MoO_4]^{2-}$ units	$\{MoO_4\}$, $\{FeClO_3N_2\}$	corner-sharing $\{MoO_4\}$ tetrahedra and $\{FeClO_3(2,2'\text{-bpy})\}$ octahedra linked into a 1D chain	71	[181]
$[Mo_3O_{12}\{Fe(2,2'\text{-bpy})\}_2]\cdot 0.25\,H_2O$ (**MOXI-22**)	$[MoO_4]^{2-}$ units	$\{MoO_4\}$, $\{FeO_4N_2\}$	as for $[MoO_4\{FeCl(2,2'\text{-bpy})\}]$ with Cl on adjacent Fe sites replaced by O donor from $\{MoO_4\}$ unit	71	[181]
$[Mo_4O_{15}\{Fe(2,2'\text{-bpy})\}]$ (**MOXI-23**)	$[MoO_4]^{2-}$ and $[Mo_2O_7]^{2-}$ units	$\{MoO_4\}$, $\{FeO_4N_2\}$	as for $[Mo_3O_{12}\{Fe(2,2'\text{-bpy})\}_2]$ with bridging $\{MoO_4\}$ replaced by $\{Mo_2O_7\}$	71	[181]
$[Cu(bpa)_{0.5}(MoO_4)]$ (**MOXI-24**)	$[MoO_4]^{2-}$ units	$\{MoO_4\}$ and $\{CuO_5N\}$	2D $\{CuMoO_4\}$ sheets linked by bpa ligands into a 3D covalent framework	72	[182]
$[Cu(pz)_{0.5}(MoO_4)]$ (**MOXI-25**)	$[MoO_4]^{2-}$ units	$\{MoO_4\}$ and square-pyramidal $\{CuO_4N\}$	$\{Mo_2Cu_2O_4\}$ rings fused into 1D tubes which are linked by bridging oxygen atoms and py ligands into a 3D covalent framework	73	[182]
$[Cu(bpe)(MoO_4)]$ (**MOXI-1**)	$[MoO_4]^{2-}$ units	$\{MoO_4\}$ and trigonal-bipyramidal $\{CuO_3N_2\}$	1D $\{Cu(bpe)\}$ chains linked by $\{MoO_4\}$ groups into a 3D covalent framework	49	[141]
$[\{Ni(dpa)_2\}MoO_4]$ (**MOXI-26**)	$[MoO_4]^{2-}$ units	$\{MoO_4\}$ and $\{NiN_4O_2\}$	2D networks of fused $\{Ni_4(dpa)_4\}$ rings linked by η^2-$\{MoO_4\}$ tetrahedra into a 3D framework	–	[183]
$[\{Zn(o\text{-phen})\}MoO_4]$ (**MOXI-29**)	$[MoO_4]^{2-}$ units	$\{MoO_4\}$ and trigonal-bipyramidal $\{ZnN_2O_5\}$	1D chain of corner-sharing Mo tetrahedra and Cu square pyramids	–	[150]
$[\{Cu_2(trz)_2(H_2O)_2\}Mo_4O_{13}]$ (**MOXI-33**)	1D	$\{MoO_6\}$, $\{CuN_4O_2\}$, $\{CuN_2O_4\}$	1D chains of edge- and corner-sharing Mo octahedra entrained within a 3D $\{Cu_2(tz)_2\}^{2+}$ framework	68	[187]

[a] Compound identity number in boldface in parentheses.

4.1. Organoammonium – Molybdenum Oxide Phases

The use of organoammonium cations as structure-directing agents for oxide phases is well documented.[51] The prototypical molybdenum oxide is $(H_3NCH_2CH_2NH_3)[Mo_3O_{10}]$ (**MOXI-2**)[142] (Figure 50a). The structure consists of a one-dimensional chain of edge-, corner-, and face-sharing molybdenum octahedra. The cation exhibits multipoint hydrogen bonding to the terminal and bridging oxo groups of the chain, and occupies channels formed by parallel stacking of three adjacent chains.

The significant structural role played by the organic cation is manifest in a comparison of the structure of **MOXI-2** with that of $[H_3N(CH_2)_6NH_3][Mo_4O_{13}]$[143] (Figure 50b), which is constructed from $\{Mo_4O_{13}\}^{2-}$ units composed of edge-sharing octahedra. Two $\{Mo_4O_{13}\}^{2-}$ units fuse by edge sharing to form a compact $\{Mo_8O_{26}\}^{4-}$ cluster; propagation is achieved by four corner-sharing interactions between adjacent $\{Mo_8O_{26}\}^{4-}$ units. These organically templated structures may also be compared to the one-dimensional structures of $K_2[Mo_3O_{10}]$[144] and $(NH_4)_2[Mo_3O_{10}]$,[145] which serve to illustrate the variable modes of polyhedral condensation which are generated by the introduction of cations with different charge and spatial requirements.

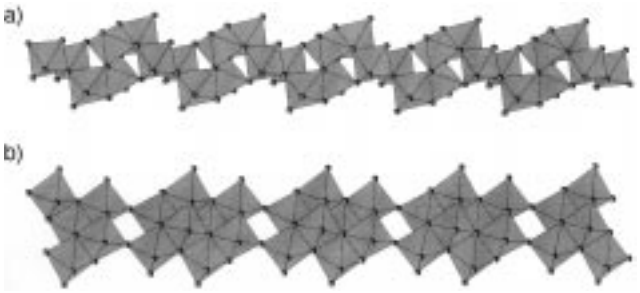

Figure 50. a) The structure of the one-dimensional chain of $(H_2en)[Mo_3O_{10}]$ (**MOXI-2**). b) The structure of the anion of $[H_3N(CH_2)_6NH_3][Mo_4O_{13}]$.

The only example of a two-dimensional organically templated molybdenum oxide of this subclass is provided by $(4,4'\text{-}H_2bpy)[Mo_7O_{22}]\cdot H_2O$[146] (**MOXI-3**), shown in Figure 51. The structure consists of molybdenum oxide layers, separated by an interlamellar region populated by $(4,4'\text{-}H_2bpy)^{2+}$ cations and H_2O molecules of crystallization. The inorganic subunit of **MOXI-3** is both structurally and compositionally related to the layered oxide MoO_3.[147] In a formal sense, **MOXI-3** may be considered to derive from MoO_3 through intercalation of $(4,4'\text{-}H_2bpy)^{2+}$ cations and water, requiring the addition of an oxide anion to the inorganic framework to achieve charge compensation. Since charge/volume considerations result in one bipyridinium cation for seven molybdenum oxide sites, **MOXI-3** may be reformulated as $(4,4'\text{-}H_2bpy)[(MoO_3)_7O]\cdot H_2O$ to reflect its relationship to the MoO_3 parent.

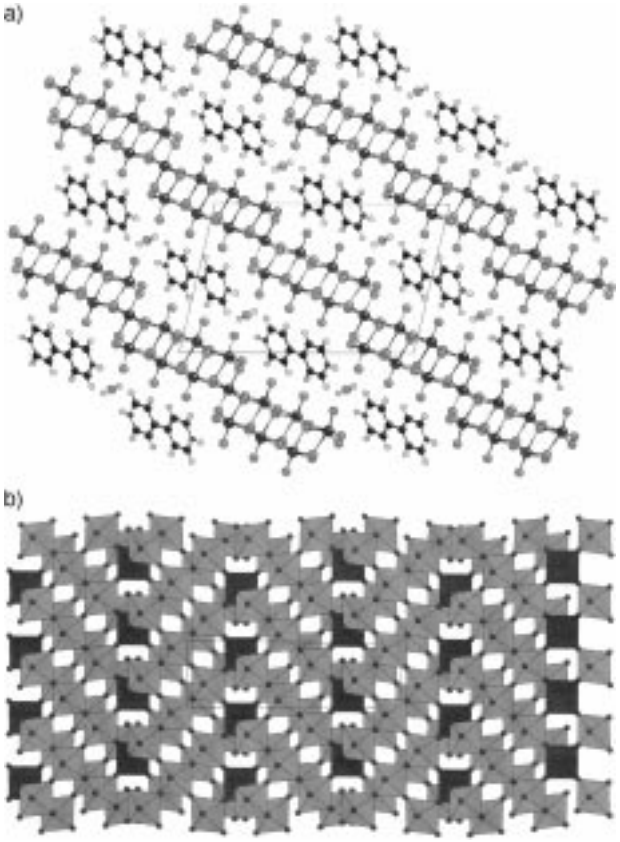

Figure 51. a) The stepped layer structure of **MOXI-3**. b) A view normal to the oxide layer. The darkened polyhedra indicate the positions of the dislocations that give rise to the "steps".

However, the layer in MoO_3 is constructed from linear ribbons, two polyhedra thick, of edge-sharing $\{MoO_6\}$ octahedra; adjacent ribbons are linked through corner-sharing to produce the layer structure. Consequently, each Mo site in MoO_3 displays three triply bridging, two doubly bridging, and one terminal oxo group. In contrast, the oxide layers of **MOXI-3** are distinctly stepped. While the motif of ribbons of edge-sharing octahedra is present in both MoO_3 and **MOXI-3**, the ribbon in the latter executes a 90° turn and shifts one polyhedral length along the *b* direction at the "step" juncture at every seventh Mo site. Adjacent ribbons are again linked through corner-sharing interactions, but in such a fashion as to produce three distinct $\{MoO_6\}$ sites. The organic cations and the water molecules occupy the interlamellar region and participate in strong multipoint hydrogen bonding to each other and to the terminal oxo groups of the layer. The structure provides a dramatic demonstration of the role of organic cations in influencing oxide structure.

4.2. Organodiamines as Ligands to the Molybdenum Oxide Array

The compounds of the $[(MoO_3)_n(2,2'\text{-bpy})_m]$ family illustrate ligand control of stepwise growth of the polymer chain. As shown in Figure 52, the structures of $[MoO_3(2,2'\text{-bpy})]$ (**MOXI-4**), $[(MoO_3)_2(2,2'\text{-bpy})]$ (**MOXI-5**) and $[(MoO_3)_3(2,2'\text{-bpy})_2]$ (**MOXI-6**)[148] are one-dimensional chains of fused

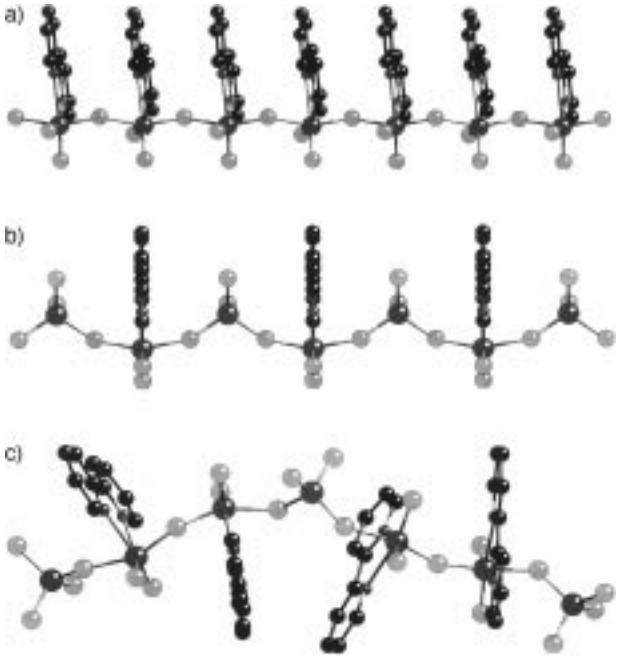

Figure 52. The structures of a) **MOXI-4**, b) **MOXI-5**, and c) **MOXI-6**.

molybdenum polyhedra. While the structure of **MOXI-4** consists of chains of corner-sharing $\{MoO_4N_2\}$ octahedra, that of **MOXI-5** is constructed from alternating corner-sharing $\{MoO_4N_2\}$ octahedra and $\{MoO_4\}$ tetrahedra. The structure of **MOXI-6** exhibits a repeat sequence of two corner-sharing $\{MoO_4N_2\}$ octahedra followed by a single $\{MoO_4\}$ tetrahedron. It is noteworthy that **MOXI-4–6** exhibit exclusively corner-sharing interactions while **MOXI-2**, $[H_3N(CH_2)_6NH_3][Mo_4O_{13}]$, $K_2[Mo_3O_{10}]$, and $(NH_4)_2[Mo_3O_{10}]$ exhibit edge sharing as one condensation mode. This suggests that the bipyridine ligand "passivates" the molybdenum oxide coordination sphere by blocking further Mo–oxo bond formation. This suggests a convenient route to low-dimensional metal oxides by exploitation of chelating amines as coligands.

Donor-group orientation has been seen in the case of the cationic coordination polymers of Section 3 to influence profoundly the structure of the array. Similarly, the structure of $[Mo_4O_{13}(Hbpa)_2]$ (**MOXI-7**)[149] is unique. The one-dimensional chain (Figure 53) is constructed from edge- and corner-sharing $\{MoO_5N\}$ octahedra and $\{MoO_5\}$ square pyramids. The $Hbpa^+$ group acts both as cation as a consequence of protonation of the nitrogen atom of the pendant arm and as a ligand covalently attached to the oxide chain. There is strong hydrogen bonding between the NH of the $Hbpa^+$ group and the oxo groups of an adjacent chain, to generate a two-dimensional rectangular grid motif, reminiscent of those observed for the one-dimensional coordination polymers, shown in Figure 6 for the prototypical $[Cu(4,4'\text{-bpy})(BF_4)_2(H_2O)_2]\cdot(4,4'\text{-bpy})$.

The rodlike 4,4′-bipyridine group can be used as a ligand, rather than as a cationic component as observed for **MOXI-3**. By raising the pH value of the reaction medium to prevent protonation of the pyridyl nitrogens, $[MoO_3(4,4'\text{-bpy})_{0.5}]$ (**MOXI-8**)[151] was prepared. The structure of **MOXI-8** (Figure 54) consists of layers of corner-sharing $\{MoO_5\}$ square

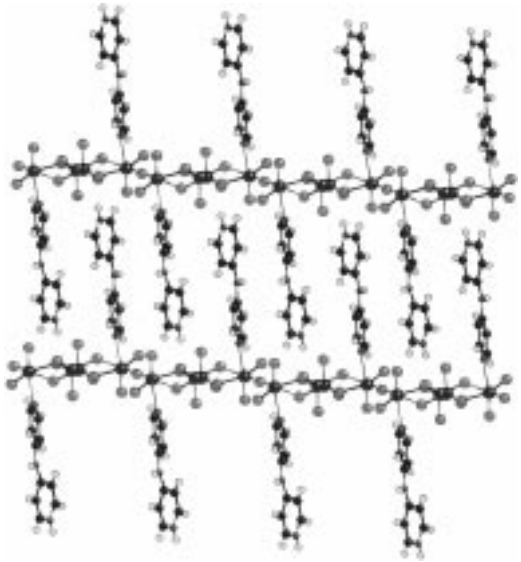

Figure 53. The structure of **MOXI-7**, which is constructed of one-dimensional chains hydrogen bonded into a rectangular grid motif.

pyramids linked through 4,4′-bipyridyl groups into a three-dimensional covalently bonded metal oxide/organic ligand framework. The overall structure of **MOXI-8** may be described in terms of alternating inorganic metal oxide layers and aromatic organic layers. The distorted $\{MoO_5N\}$ coordination geometry at each molybdenum site is defined by a terminal oxo group, four asymmetrically bridging oxo groups, and a pyridyl nitrogen donor, and has the typical "two short-two intermediate-two long" bond length geometry common to molybdenum oxides.

It should be pointed out that the structure of **MOXI-8** is quite distinct from the layered structure adopted by MoO_3,[147] which exhibits both edge and corner sharing of $\{MoO_6\}$ octahedra. However, the structure of **MOXI-8** does have some features in common with the proposed structure of the pyridine intercalation phase $[MoO_3(pyridine)]$.[152]

A mixed valence analogue of **MOXI-8**, $[HMo_2O_6(4,4'\text{-bpy})]$ (**MOXI-9**) may be readily prepared by the introduction of a reducing agent into the synthesis. The structure of **MOXI-9** is similar to that of **MOXI-8**, except that the octahedra adopt a more regular 5+1 type coordination, rather than the 2+2+2 observed for **MOXI-8** (Figure 55). This structural trend is similar to that observed for MoO_3 and the mixed valence oxide hydroxides $[MoO_{3-x}(OH)_x]$.[153–156]

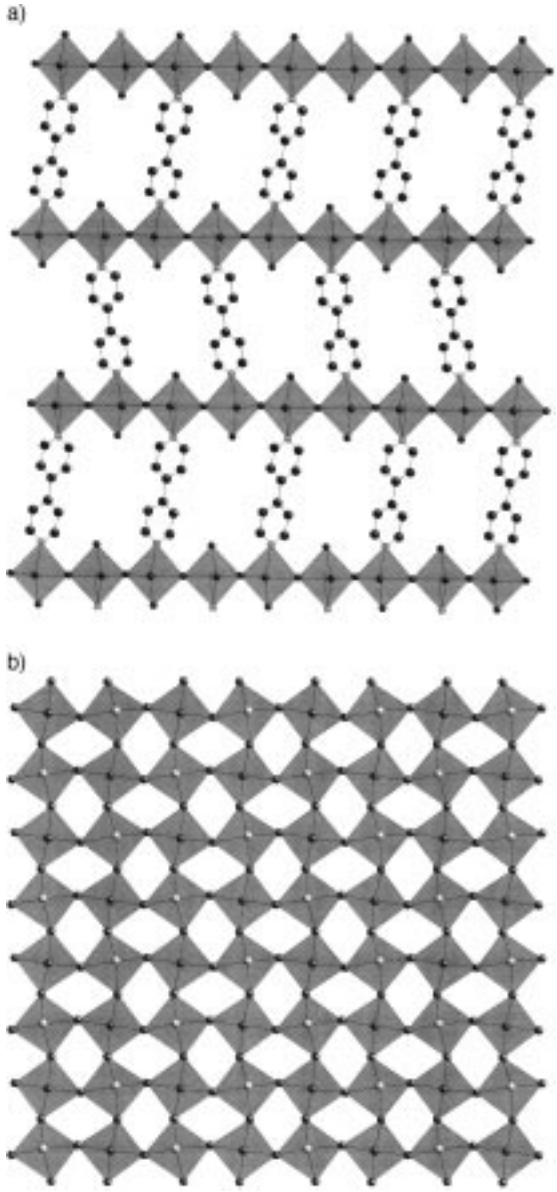

Figure 54. The structure of **MOXI-8** a) showing the linking of layers by 4,4′-bpy ligands; b) a view normal to the layer.

4.3. Molybdenum Oxide Phases Containing Organodiamine-Ligated Heterometals

The heterometal-containing molybdenum oxide composites of this type fall into three general subgroups, classified according to the dimensionality of the molybdenum array and to the dimensionality of the M′-Mo-O array. Three subgroups are identified:

1) Discrete molybdenum oxide polyanion clusters linked by heterometal–diamine coordination complexes or polymers into higher dimensional aggregates.
2) One-dimensional molybdenum oxide chains linked by heterometal–diamine coordination polymers into complex aggregates.
3) One-, two-, and three-dimensional arrays of mixed molybdenum oxide–heterometal–diamine fused polyhedra.

4.3.1. Solids Constructed from Discrete Molybdenum Oxide Clusters

There is significant contemporary interest in the solid-state chemistry of molecularly derived solids with extended linkages.[157, 158] One-dimensional ensembles have been prepared from the $[Mo_6Cl_8(O_2CR)_6]^{2-}$ cluster[159] and three-dimensional assemblies for $[Nb_6X_3Y_6]^{4+}$.[126, 127] Chain, layer, and three-dimensional frameworks based on polyoxometalate clusters, either directly fused through bridging oxo groups or linked through heterometallic sites, have also been described.[160–170]

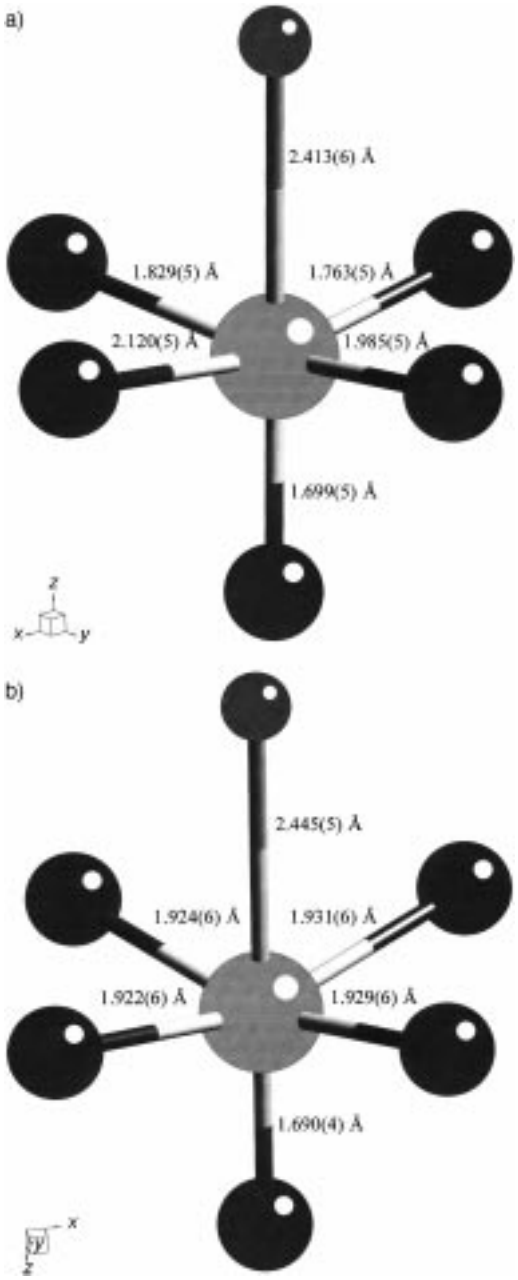

Figure 55. The contrasting geometries of the Mo sites of **MOXI-8** and **MOXI-9**.

Representative examples include the chain structure of $[\{Co(H_2O)_4\}_2(H_2W_{12}O_{42})]^{6-}$,[165] the two-dimensional network exhibited by $[\{Ni(en)_2\}_3(V_{18}O_{42}Cl)]^{-0.5}$,[170] and the three-dimensional framework of $[Na_2Co_2H_2W_{12}O_{42}(H_2O)_{12}]^{4-}$.[169]

The primitive protostructure for this subgroup of the review is provided by $[\{Ni(2,2'\text{-bpy})_2\}_2Mo_4O_{14}]$,[171] which displays a simple ring structure of two $\{Mo_2O_7\}^{2-}$ units linked by two $\{Ni(2,2'\text{-bpy})_2\}^{2+}$ groups into a cluster with a $\{Mo_4Ni_2O_6\}$ ring core. Similarly, the structure of $[\{Cu(o\text{-phen})_2\}_2Mo_8O_{26}]$ (**MOXI-27**) consists of an α-$[Mo_8O_{26}]^{4-}$ cluster with two $[Cu(o\text{-phen})_2]^{2+}$ groups covalently attached to peripheral oxo groups (Figure 56). While these structures lack extension into the polymeric domain, the ease of attachment of heterometal–diamine complexes to the surface of such clusters is established.

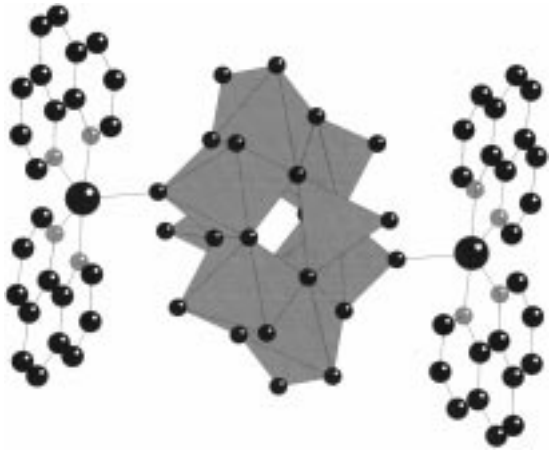

Figure 56. The structure of $[\{Cu(o\text{-phen})_2\}_2Mo_8O_{26}]$ (**MOXI-27**).

The prototypical solid-state structure is that of $[Ni(2,2'\text{-bpy})_2Mo_4O_{13}]$ (**MOXI-10**; Figure 57). The structure is constructed from β-$\{Mo_8O_{26}\}^{4-}$ clusters linked by $\{Ni(2,2'\text{-bpy})_2\}^{2+}$ bridges into a one-dimensional chain. It is instructive to note that the octamolybdate unit of **MOXI-10** is distinct from that observed for $[\{Cu(o\text{-phen})_2\}_2Mo_8O_{26}]$. Five isomers of $[Mo_8O_{26}]^{4-}$ have now been described. The α, β, and γ isomers

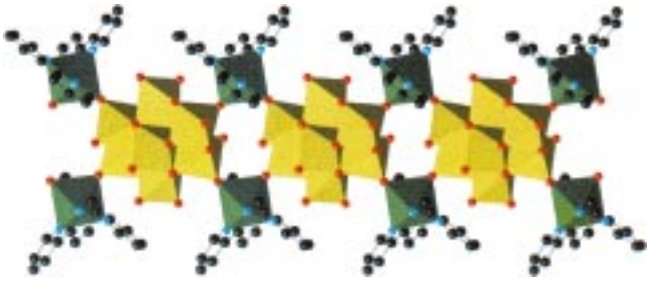

Figure 57. The structure of $[Ni(2,2'\text{-bpy})_2Mo_4O_{13}]$ (**MOXI-10**).

had been isolated in a number of salts,[174, 175] while the δ form has been reported as the (α-δ) or (β-δ) "intermediate" structure.[176] The ε form is thus far unique to the heterometal–diamine molybdenum oxide materials. As shown in Figure 58, the isomer structures differ in number, type, and fusion mode of the molybdenum polyhedra. The five forms are conceptually and chemically interrelated by minimal bond breaking through lengthening of axial interactions and polyhedral rotations. The occurrence of a particular isomer in the hydrothermal product is not predictable, a not unreasonable observation given the lack of significant energy differences between the structure types.

The steric constraints imposed by the bulky *o*-phen ligands of $[\{Cu(o\text{-phen})_2\}_2Mo_8O_{26}]$ are evidently released in the ethylenediamine derivative $[\{Cu(en)_2\}_2Mo_8O_{26}]$ (**MOXI-11**).[170] The structure is constructed from δ-$[Mo_8O_{26}]^{4-}$ clusters linked by $\{Cu(en)_2\}^{2+}$ groups into the two-dimensional sheet shown in Figure 59.

As the structural complexity of the heterometal–diamine complex cation increases, more exotic composite arrays of linked clusters are observed. Thus, the structure of $[\{Cu(4,4'\text{-bpy})\}_4Mo_8O_{26}]$ (**MOXI-12**), as shown in Figure 60, consists of

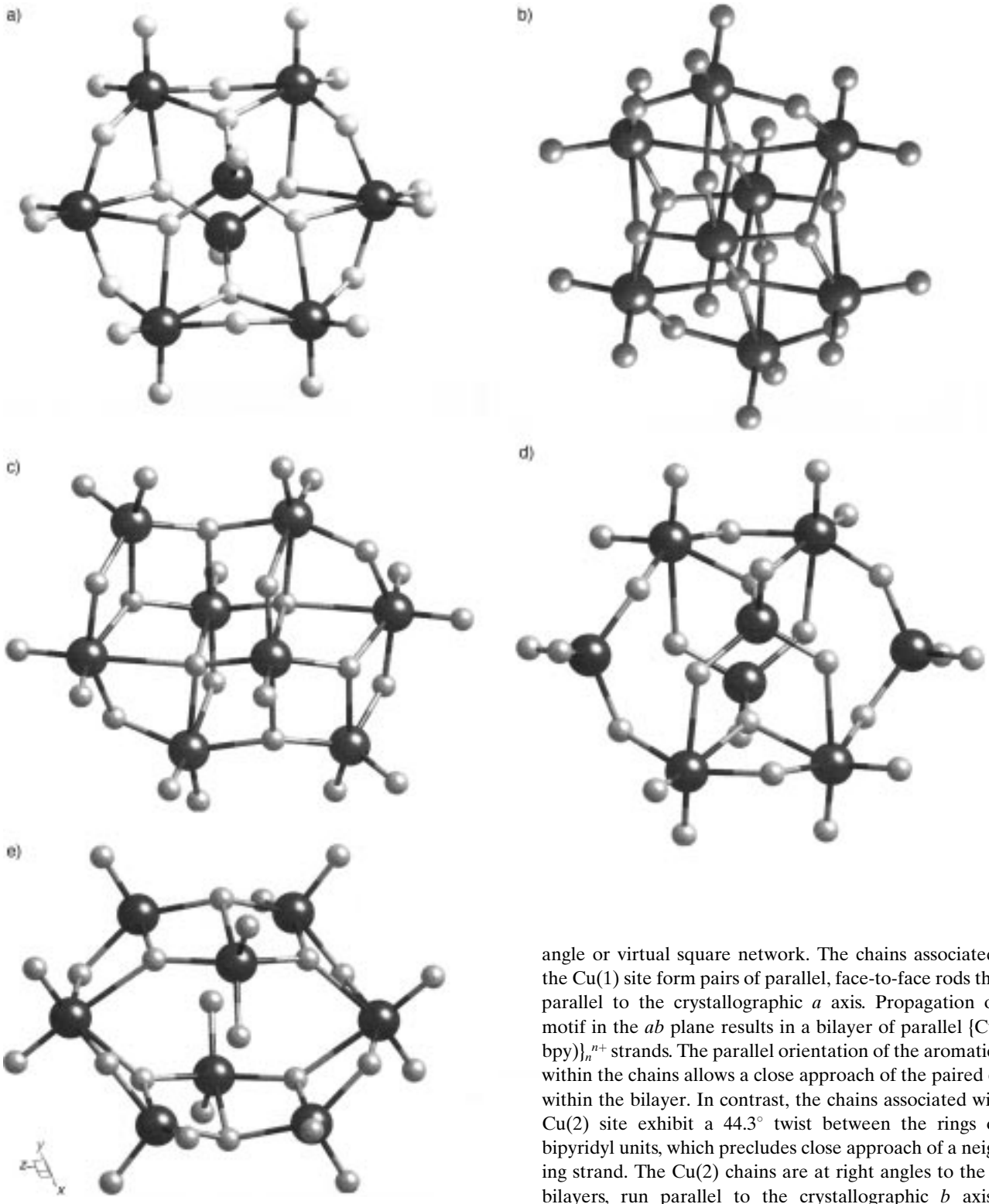

Figure 58. The structures of the a) α, b) β, c) γ, d) δ, and e) ε forms of $[Mo_8O_{26}]^{4-}$.

δ-$[Mo_8O_{26}]^{4-}$ clusters and $\{Cu(4,4'\text{-bpy})\}^{+}$ linear chains. The cation component, $\{Cu(4,4'\text{-bpy})\}^{+}$, provides the scaffolding as chains of digonally coordinated Cu^{I} centers. The relative orientation of the chains is unusual and results in cavities within the scaffolding that accommodate the $[Mo_8O_{26}]^{4-}$ units. There are two distinct chain environments that form a right angle or virtual square network. The chains associated with the Cu(1) site form pairs of parallel, face-to-face rods that run parallel to the crystallographic *a* axis. Propagation of this motif in the *ab* plane results in a bilayer of parallel $\{Cu(4,4'\text{-bpy})\}_n^{n+}$ strands. The parallel orientation of the aromatic rings within the chains allows a close approach of the paired chains within the bilayer. In contrast, the chains associated with the Cu(2) site exhibit a 44.3° twist between the rings of the bipyridyl units, which precludes close approach of a neighboring strand. The Cu(2) chains are at right angles to the Cu(1) bilayers, run parallel to the crystallographic *b* axis, and propagate as parallel strands in the *ab* plane.

The $[Mo_8O_{26}]^{4-}$ clusters occupy cavities defined by two adjacent pairs of Cu(1) chains and one Cu(2) strand from each of two adjacent layers. The terminal oxo group of one tripodal Mo site exhibits weak long-range interactions of 2.555(5) and 2.691(4) Å with the Cu(1) sites, while oxo groups of tetrahedral and octahedral ring Mo sites display essentially nonbonding interactions with the Cu(2) sites. This long-range connectivity provides a virtual layer structure, in which the

Figure 59. The structure of **MOXI-11**.

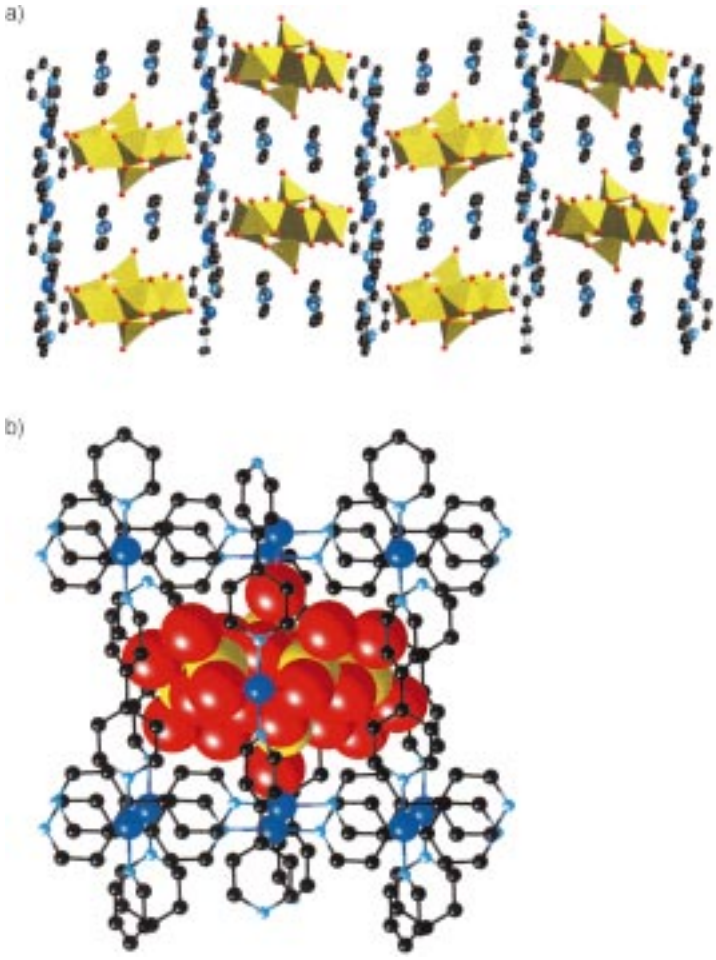

Figure 60. a) The structure of **MOXI-12**. b) A view of the $[Mo_8O_{26}]^{4-}$ polyoxoanion entrained within the rigid polymeric cation network.

Cu(1) bilayers and $[Mo_8O_{26}]^{4-}$ subunits are sandwiched between the layers of parallel $\{Cu(2)(4,4'\text{-bpy})\}_n^{n+}$ strands. Adjacent layers are slotted together since alternate Cu(2) strands interact with $[Mo_8O_{26}]^{4-}$ clusters of an adjacent layer.

A related structure is exhibited by $[\{Cu(bpe)\}_4Mo_8O_{26}]$ (**MOXI-13**). However, the α form of the octamolybdate is observed with capping tetrahedral sites involved in the bonding to the parallel $\{Cu(bpe)\}^+$ double chains. In contrast to the structure of **MOXI-11**, the interlamellar chains are parallel to the double chains.

An unusual structural variant of **MOXI-12** and **MOXI-13** results when pyridazine is introduced in place of the 4,4′-bipyridine of **MOXI-12** or the 4,4′-bipyridylethene of **MOXI-13**. In the case of $[\{Cu(pyrd)\}_4Mo_8O_{26}]$ (**MOXI-34**),[178] the γ-$[Mo_8O_{26}]^{4-}$ type is observed. Each molybdate cluster bonds to four $\{Cu_2(pyrd)_2\}$ units, which are present in the form of the tetranuclear $\{Cu_4O_6(pyrd)_4\}$ clusters (Figure 61). The copper

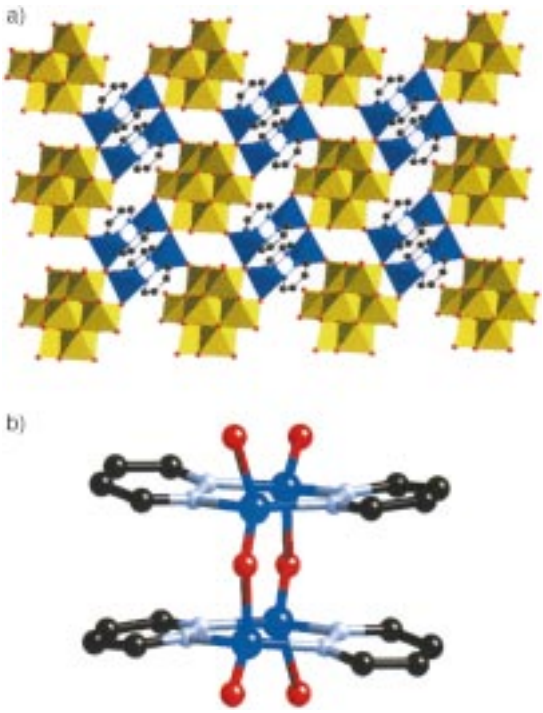

Figure 61. a) A view of the two-dimensional sheet of γ-$[Mo_8O_{26}]^{4-}$ clusters linked by $\{Cu_4O_6(pyrd)_4\}$ clusters of **MOXI-34**. b) The $\{Cu_4O_6(pyrd)_4\}$ cluster.

clusters consist of pairs of oxo-bridged copper tetrahedra which are linked through four pyridazine ligands in such a fashion as to generate a Cu_4 box of dimensions 3.25 Å × 3.02 Å with π-stacked pyridazine rings. Each $\{Cu_4O_6(pyrd)_4\}$ cluster links a molybdate cluster to three neighboring cluster units. The resultant two-dimensional sheet may be described in terms of corner-shared polyhedra from two distinct cluster types.

Modification of the coordination polymer scaffolding in these materials can be readily accomplished by the introduction of a d-block cation with coordination requirements different from those of Cu^I, such as Ni^{II} for which octahedral geometry is most common. The point is illustrated by the structure of $[\{Ni(4,4'\text{-bpy})_2(H_2O)_2\}_2Mo_8O_{26}]$ (**MOXI-14**; Figure 62). The structure of **MOXI-14** is constructed from novel ε-$[Mo_8O_{26}]^{4-}$ clusters and $\{Ni(H_2O)_2(4,4'\text{-bpy})_2\}_n^{2n+}$ one-dimensional zigzag chains. The molybdate cluster adopts an unprecedented structure consisting of six $\{MoO_5\}$ square pyramids and two $\{MoO_6\}$ octahedra that edge-share to form an ellipsoidal cluster, whose major axis is defined by the

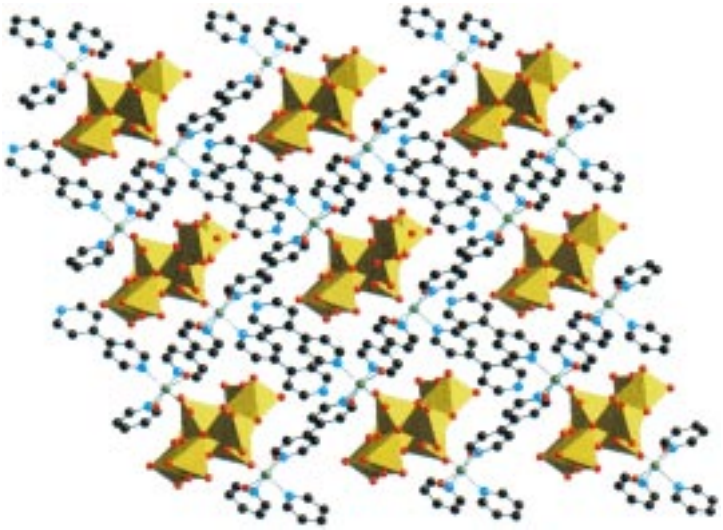

Figure 62. The structure of **MOXI-14**.

vector that joins the octahedral sites. The geometry adopted by this ε-$[Mo_8O_{26}]^{4-}$ subunit reflects the steric constraints imposed by the polymer scaffolding of the $\{Ni(H_2O)_2(4,4'\text{-bpy})_2\}_n^{2n+}$ motif. The cationic component forms zigzag chains of *fac*-$\{NiO_3N_3\}$ octahedra linked through bridging, bidentate 4,4′-bpy groups. Each Ni^{II} site of the chain is coordinated to nitrogen donors from three 4,4′-bpy ligands, two aqua ligands, and a terminal oxo group from the molybdate cluster subunit. Since the 4,4′-bpy groups occupy *cis* positions on the Ni^{II} sites, the $\{Ni(H_2O)_2(4,4'\text{-bpy})_2\}_n^{2n+}$ chain has a fold of about 90° at each Ni atom. It is noteworthy that the third 4,4′-bpy unit of each Ni center adopts monodentate coordination. The pendant 4,4′-bpy groups of adjacent $\{Ni(H_2O)_2(4,4'\text{-bpy})_2\}_n^{2n+}$ chains project into the interchain region to form π-stacked pairs, which define the boundaries of the interchain cavity.

The polymeric scaffolding of **MOXI-14** is connected to the polyoxoanion clusters by covalent bonding of the terminal oxo group of one Mo center to the Ni^{II} site. This produces a two-dimensional covalent framework with "chains" of $[Mo_8O_{26}]^{4-}$ groups incorporated within the polymeric $\{Ni(H_2O)_2(4,4'\text{-bpy})_2\}_n^{2n+}$ backbone. The anionic subunits are confined within a rectangular channel defined by neighboring $\{Ni(H_2O)_2(4,4'\text{-bpy})_2\}_n^{2n+}$ strands and the pendant 4,4′-bpy groups that project from these strands. The ellipsoidal structure adopted by the $[Mo_8O_{26}]^{4-}$ moiety in **MOXI-14** conforms to the shape constraints thus imposed.

The most unusual example of a solid constructed from linked clusters is provided by $[\{Cu_3(4,7\text{-phen})_3\}_2Mo_{14}O_{45}]$ (**MOXI-15**)[179] which consists of β-$[Mo_8O_{26}]^{4-}$ and $[Mo_6O_{19}]^{2-}$ clusters interconnected by $\{Cu_3(4,7\text{-phen})_3\}^{3+}$ rings into a two-dimensional network (Figure 63). The hexamolybdate fragments appear to be stabilized by sandwiching between $\{Cu_3(4,7\text{-phen})_3\}^{3+}$ rings, an observation which illustrates the dramatic influence of cation geometry on the anion packing.

4.3.2. Solids Exhibiting One-Dimensional Molybdenum Oxide Arrays

An example of one-dimensional molybdenum oxide chains linked to polymeric coordination cations is provided by

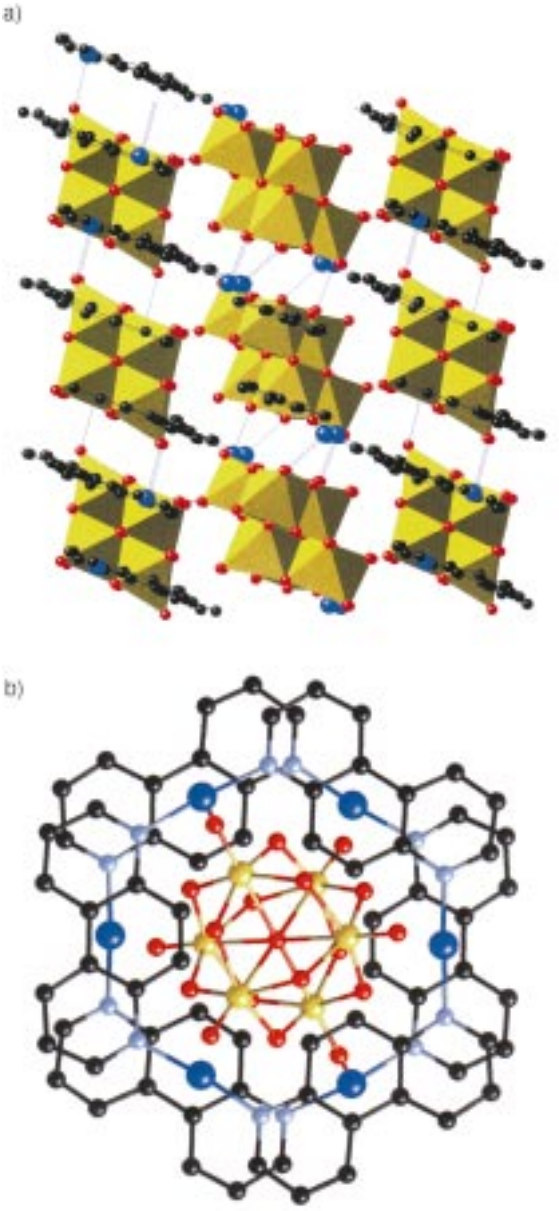

Figure 63. a) A polyhedral representation of the structure of **MOXI-15**. b) A view of the $[Mo_6O_{19}]^{2-}$ clusters sandwiched between $\{Cu_3(4,7\text{-phen})_3\}^{3+}$ rings.

$[\{Cu(4,4'\text{-bpy})\}_4Mo_{15}O_{47}]\cdot H_2O$ (**MOXI-16**; Figure 64).[177] The structure of **MOXI-16** is constructed from $\{Mo_{15}O_{47}\}_n^{4n-}$ chains parallel to the crystallographic *a* axis and $\{Cu(4,4'\text{-bpy})\}_n^{n+}$ rods parallel to the *b* axis. There are two distinct Mo environments. The Mo(1) sites form chains of *trans*, corner-sharing octahedra and have two terminal, one doubly bridging, and three triply bridging oxo groups. Two Mo(1) chains are linked by a double chain of Mo(2) centers, which is constructed from *cis*-planar, edge-sharing octahedra. Each Mo(2) site has a single terminal, one doubly bridging, and four triply bridging oxo groups. The terminal oxo group of each Mo(1) site is directed toward a Cu^+ site of the $\{Cu(4,4'\text{-bpy})\}_n^{n+}$ rods that extend at right angles to the $\{Mo_{15}O_{47}\}_n^{4n-}$ chains. The result is an inorganic virtual layer of parallel molybdenum oxide chains that is sandwiched between

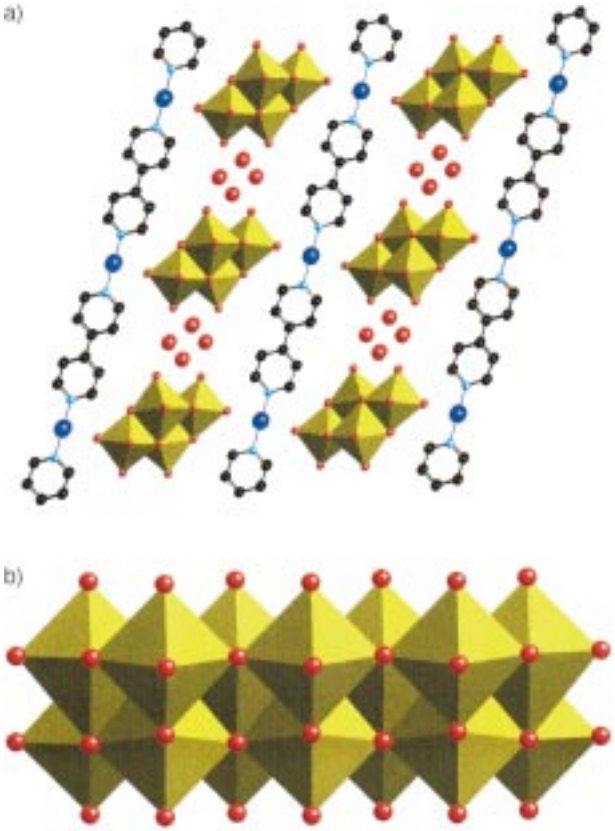

Figure 64. a) A view of the structure of **MOXI-16**, along the crystallographic *b* axis and parallel to the chain axis. b) A polyhedral view of the molybdenum oxide chain.

organic/inorganic composite layers; water molecules of crystallization occupy the interstrand region. It is noteworthy that the chain structure is not related to those previously described in Section 4.1.

An elaboration of structural types may be effected by modification of the nature of the organodiamine ligand. For example, exploitation of the chelating 2,2′-bipyridine in place of the bridging 4,4′-bipyridine resulted in the isolation of $[Cu(2,2'\text{-bpy})Mo_2O_7]$ (**MOXI-17**) and $[Co(2,2'\text{-bpy})Mo_3O_{10}]$ (**MOXI-18**).[172] The structure of **MOXI-17** consists of a buckled one-dimensional molybdenum oxide chain linked to peripheral $\{CuN_2O_4\}$ octahedra (Figure 65). The $\{Mo_2O_7\}$ chain is constructed from edge-sharing $\{MoO_6\}$ octahedra and $\{MoO_5\}$ square pyramids. Each molybdenum octahedron shares common edges with a neighboring molybdenum octahedron, a molybdenum square pyramid, and two copper octahedra, and a common corner with one square-pyramidal unit. One square-pyramidal site engages in edge sharing with an adjacent square pyramid and a molybdenum octahedron, and displays corner sharing with a second molybdenum octahedron and two $\{CuN_2O_4\}$ octahedra, while the second $\{MoO_5\}$ site exhibits edge sharing to a square-pyramidal and an octahedral molybdenum site, and corner-sharing to a $\{MoO_6\}$ site and a $\{CuN_2O_4\}$ octahedron. Consequently, each $\{CuN_2O_4\}$ unit links to four molybdenum polyhedra of the chain, to share four vertices in two edge and two corner interactions with the molybdenum sites. The folding of the molybdenum chain reflects the incorporation of the $\{CuN_2O_4\}$ units through four-point, two-edge attachments and illustrates the role of the M^{2+} site in defining chain geometry.

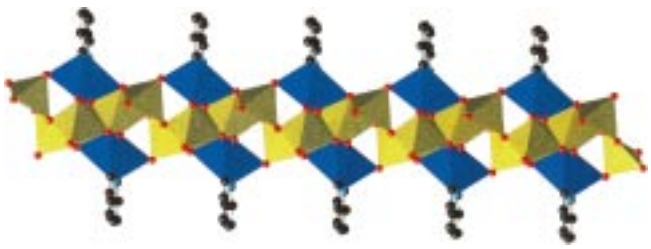

Figure 65. A view of the structure of **MOXI-17**.

Since one-dimensional molybdenum oxide chains are a recurring theme in oxide structural chemistry, the incorporation of appropriate metal–ligand subunits should allow bridging in higher dimensional solids. The structure of **MOXI-18** (Figure 66) illustrates this point. The structure consists of one-dimensional molybdenum oxide chains, constructed of molybdenum tetrahedra, octahedra and square pyramids, linked through $\{CoN_2O_4\}$ octahedra into a two-dimensional covalent network. The oxide chain itself results from the edge-sharing of $\{MoO_6\}$ octahedra and $\{MoO_5\}$ square pyramids. The $\{MoO_4\}$ tetrahedra link to the chain through a single corner-sharing interaction, but bridge two $\{CoN_2O_4\}$ octahedra through two additional corner-sharing linkages. Each Co site is defined by the nitrogen donors of the 2,2′-bpy ligand and four oxygen donors from three $\{MoO_4\}$ groups and one $\{MoO_6\}$ octahedron. The overall structure may be described as folded chains of edge-sharing molybdenum polyhedra linked through double chains of alternating $\{CoN_2O_4\}$ octahedra and $\{MoO_4\}$ tetrahedra into a two-dimensional network.

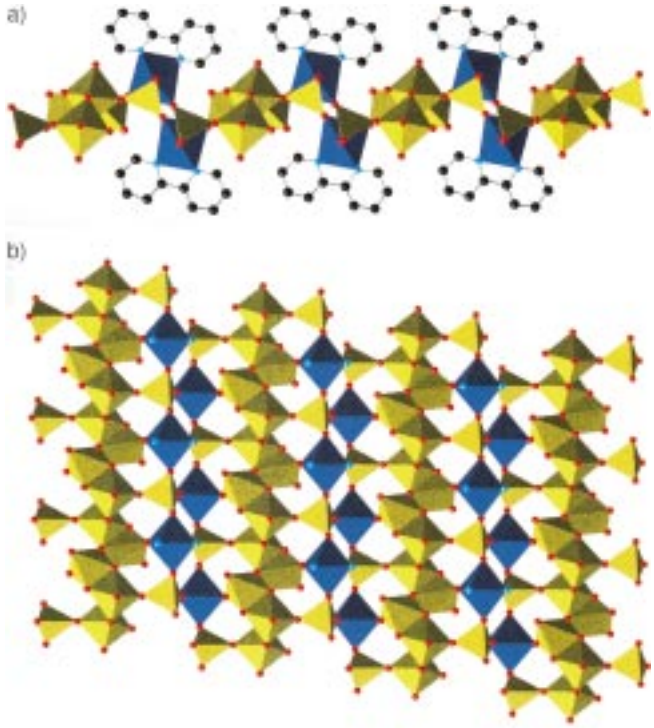

Figure 66. The structure of **MOXI-18** a) parallel to the two-dimensional net and b) normal to the layer. Co sites are blue; Mo sites are yellow.

Pyrimidine offers an intriguing ligand variant to the bridging bipyridine class of ligands in that the donor-to-donor distance is drastically reduced. The consequences of introducing pyrimidine into the Cu-molybdenum oxide chemistry are quite unanticipated. The structure of $[Cu_2(pyrd)Mo_3O_{10}]$ (**MOXI-19**)[182] is constructed from $\{MoO_6\}$ octahedra and $\{CuO_3N\}$ tetrahedra, which link to form a three-dimensional bimetallic oxide framework with channels occupied by the pyrimidine groups. As shown in Figure 67, the $\{MoO_6\}$ octahedra form a chain of edge-sharing polyhedra, structurally analogous to that observed for the one-dimensional

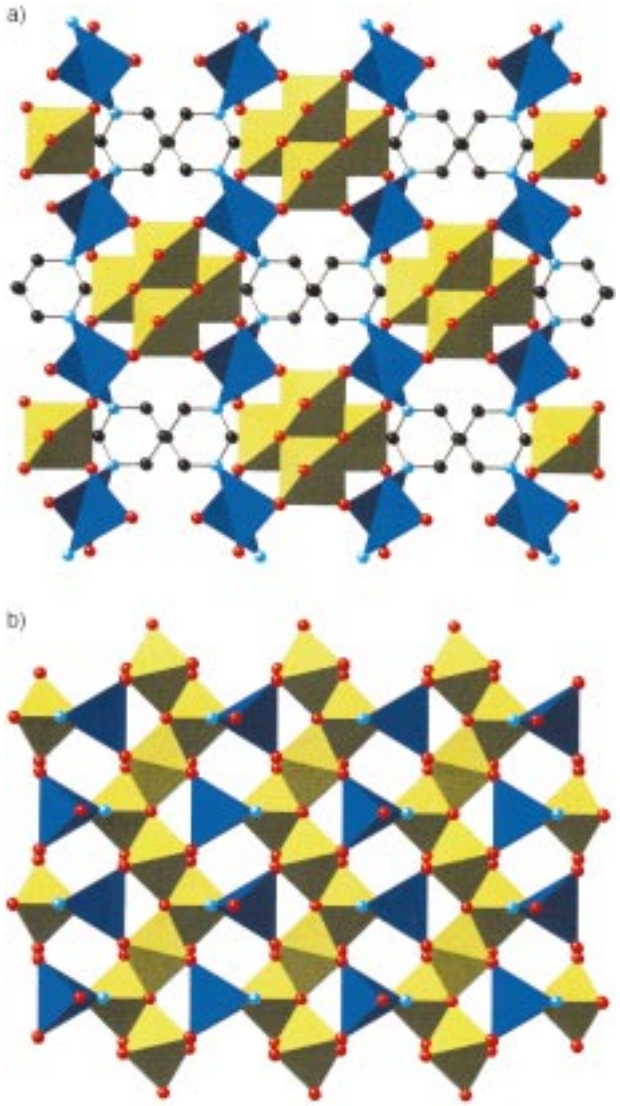

Figure 67. a) A view of the structure of **MOXI-19** to show the channels occupied by the pyrimidine groups. b) The linking of $\{Mo_3O_{10}\}^{2-}$ chains by {Cu(pyrd)} bridges.

$(NH_4)_2[Mo_3O_{10}]$. Each Cu site coordinates to two oxo groups of two Mo sites of one chain and bridges an adjacent chain by bonding to one oxo group. In addition, each Cu center coordinates to a nitrogen donor of a pyrimidine ligand, which serves to bridge to a second Cu site through its second nitrogen donor. When viewed along the crystallographic *a* axis, the Mo-oxide chains are linked through stacked $\{CuO_3N\}$ tetrahedra to produce channels of sufficient diameter to accommodate parallel stacks of pyrimidine groups.

It is noteworthy that crystals of **MOXI-19** are black, indicative of mixed valence; the only example to date for this class of materials. Valence sum calculations[173, 184] provide an average oxidation state of +5.7 for the Mo sites; curiously, the Cu sites exhibit an average oxidation state of +1.5, which suggests extensive electronic delocalization.

A curious feature of the structural chemistry of molybdenum oxides with metal-dipodal organonitrogen ligand complex cations is the absence of three-dimensional cationic frameworks, despite the use of M^{II} sites with octahedral coordination preferences. One expedient for the construction of such three-dimensional cationic frameworks would appear to be the introduction of tripodal or higher denticity ligands with appropriate donor-group orientations. The expectation of a three-dimensional cationic framework has been realized by employing 1,2,4-triazole as the organic component in the isolation of $[\{Cu_2(triazolate)_2(H_2O)_2\}Mo_4O_{13}]$ (**MOXI-33**).[187] As shown in Figure 68, the structure of **MOXI-33** consists of one-dimensional $\{Mo_4O_{13}\}_n^{2n-}$ chains entrained within the three-dimensional framework of the $\{Cu_2(triazolate)_2(H_2O)_2\}_n^{2n+}$ polymeric coordination cation. There are two unique copper sites in the cationic framework. One site, Cu(A), is effectively square pyramidal $\{CuN_4O\}$ through ligation to four triazolate nitrogen donors, one from each of four triazolate ligands and to a terminal oxo group of the molybdate chain. The second site, Cu(B), is octahedral $\{CuN_2O_4\}$, and exhibits coordination to two *trans* disposed triazolate nitrogen donors, two aqua ligands, and two terminal oxo groups of the molybdate chains. The organic moiety adopts the anionic triazolate form in a three-connected ligation mode. The resulting cationic framework is constructed from undulating chains of Cu(A) sites bridged through the 1,2-nitrogen donors of the triazolate ligands and linked to adjacent chains through the Cu(B) centers which coordinate to the remaining 4-position nitrogen donors of the triazolate ligands (Figure 68b). This connectivity pattern produces a honeycomb network when viewed along the crystallographic *c* axis. Furthermore, the disposition of bridging triazolate ligands about a chain results in linkage to four adjacent parallel chains giving rise to large tunnels which are occupied by the molybdate chains.

The undulating molybdate chain (Figure 68c) is constructed from edge-sharing molybdenum octahedra and tetrahedra. It is noteworthy that the polyhedral connectivity within these $\{Mo_4O_{13}\}_n^{2n-}$ chains is distinct from that reported for other one-dimensional molybdenum oxides: $K_2Mo_3O_{10}$, $(NH_4)_2Mo_3O_{10}$, $(H_3NCH_2CH_2NH_3)Mo_3O_{10}$, $[H_3N(CH_2)_6NH_3]$-Mo_3O_{10}, $Na(NH_4)Mo_3O_{10}$, and $[\{Cu(4,4'\text{-bpy})\}_4Mo_{15}O_{47}]$.[177] The chain structure conforms to the constraints imposed by the copper–triazolate framework and the coordination requirements of the Cu^{II} sites of the framework.

While it is tempting to classify the structural chemistry of **MOXI-33** in terms of "ship in the bottle" isolation of an oxide substructure within a rigid three-dimensional cationic framework, it is evident that this is a naive interpretation. Thus, $[Cu_2Br_2(trz)]$,[115] and $[Cu_3(trz)_2V_4O_{12}]$[150] exhibit distinctive coordination polymer substructures, as shown in Figure 69.

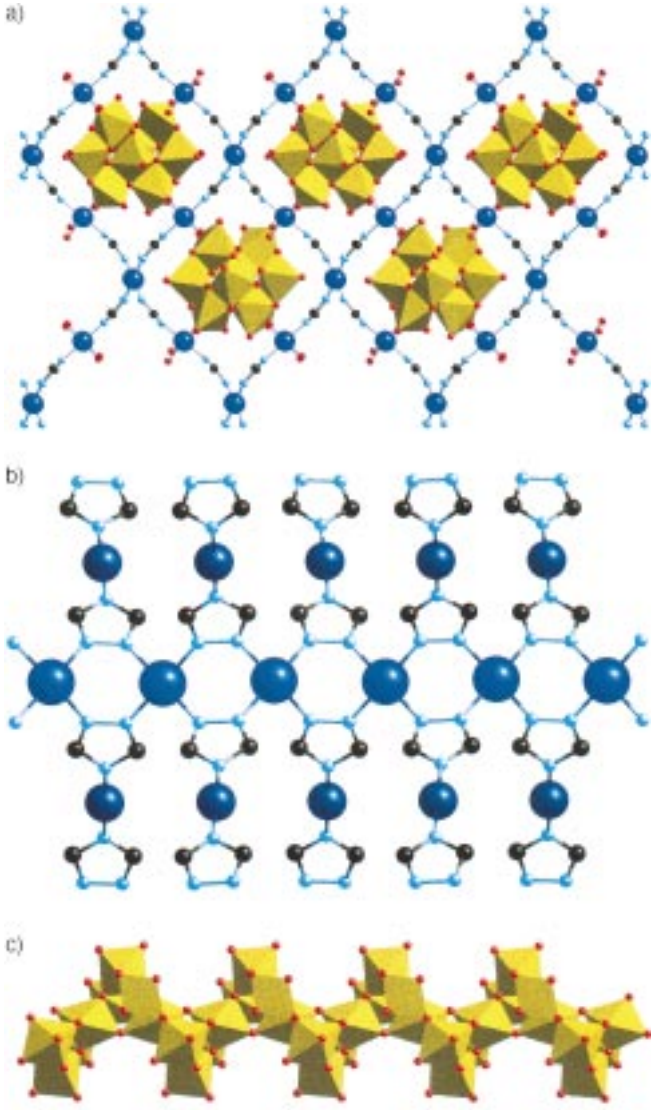

Figure 68. a) A view parallel to the molybdenum oxide chains of the structure of **MOXI-33**. b) A view of the $\{Cu_2(\text{triazolate})_2(H_2O)_2\}_n^{2n+}$ substructure. c) A view of the molybdenum oxide chain.

This observation belies the construct in which the engineered polymeric coordination cation provides a rigid matrix for the manipulation of the metal oxide motif, but rather suggests a synergism between the oxide and cationic coordination complex polymer at the organic–inorganic interface.

4.3.3. Solids Constructed from "Isolated" $[MoO_4]^{2-}$ and $[Mo_2O_7]^{2-}$ Units Fused to Bridging Heterometal–Diamine Units

The solids of this subclass are distinguished by the absence of Mo-O-Mo bridging interactions or limitation to a single Mo-O-Mo bridge unit, requiring that structural propagation occur through M′-O-Mo linkages. A simple prototype is provided by [Cu(*o*-phen)MoO_4] (**MOXI-20**; Figure 70). Two $[MoO_4]^{2-}$ tetrahedra and two $\{CuO_3N_2\}$ square pyramids form an eight-membered $\{Mo_2Cu_2O_4\}$ ring which propagates through Cu-O-Mo linkages into a stepped one-dimensional chain.

The structural versatility of such one-dimensional motifs is illustrated by the structures of $[MoO_4\{FeCl(2,2'\text{-bpy})\}]$ (**MOXI-21**), $[Mo_3O_{12}\{Fe(2,2'\text{-bpy})\}_2]\cdot 0.25\,H_2O$ (**MOXI-22**), and $[Mo_4O_{15}\{Fe(2,2'\text{-bpy})\}_2]$ (**MOXI-23**), which show the stepwise extension of chain repeat units by simple variations in reaction stoichiometries.

As shown in Figure 71, the structure of **MOXI-21** consists of one-dimensional chains comprised of $\{FeClN_2O_3\}$ octahedra and $\{MoO_4\}$ tetrahedra. Every iron octahedron corner shares through each of its oxygen atoms with an adjacent $\{MoO_4\}$ unit while each $\{MoO_4\}$ unit serves to bridge three iron octahedra. The terminal chlorides on the iron sites alternate such that two adjacent $\{FeClN_2O_3\}$ octahedra will have their chloride substituents oriented to opposite sides of the chain.

The structure of **MOXI-22** consists of chains constructed from $\{FeN_2O_4\}$ octahedra and $\{MoO_4\}$ tetrahedra. In the case of **MOXI-21**, all adjacent iron octahedra are linked through two $\{MoO_4\}$ tetrahedra. In contrast, in **MOXI-22** there are additional corner-sharing interactions between pairs of adjacent $\{FeN_2O_4\}$ octahedra and an additional $\{MoO_4\}$ tetrahedron. Consequently, adjacent pairs of $\{FeN_2O_4\}$ octahedra are linked through three $\{MoO_4\}$ tetrahedra. These units comprise two iron centers and three molybdenum centers and are then linked to a neighboring $\{Fe_2Mo_3\}$ unit by two corner-sharing interactions. Thus, the connectivity of adjacent iron sites in the chain alternates between linkage through three $\{MoO_4\}$ tetrahedra and linkage through two $\{MoO_4\}$ tetrahedra. The orientations of the additional $\{MoO_4\}$ units in **MOXI-22** with respect to the chain structure of **MOXI-21** alternate to occupy opposite sides of the chain.

MOXI-23 exhibits a one-dimensional structure very similar to that observed for **MOXI-22**. In the case of **MOXI-23**, however, the adjacent iron centers are bridged by two $\{MoO_4\}$ units and an $\{Mo_2O_7\}$ unit, while **MOXI-22** exhibits bridging through $\{MoO_4\}$ tetrahedra, exclusively. Adjacent $\{Mo_2O_7\}$ units in **MOXI-23** alternate to occupy opposite sides of the chain. The length of the $\{Mo_2O_7\}$ unit and the constraints thus imposed on the $\{FeN_2O_4\}$ units that it bridges perturb the structure of the one-dimensional chains with respect to the chains of **MOXI-22**.

As a common motif, **MOXI-21–23** all share a four-polyhedral ring which consists of two $\{MoO_4\}$ tetrahedra and two $\{FeXN_2O_3\}$ (X = Cl for **MOXI-21**, O for **MOXI-22** and **MOXI-23**) octahedra. These polyhedra corner-share such that each molybdenum center serves to bridge the two iron octahedra in the ring. Attachment to the next such four-ring is through the third corner-sharing interaction of each molybdenum tetrahedron. As the additional $\{MoO_4\}$ or $\{Mo_2O_7\}$ linkages are incorporated in **MOXI-22** and **MOXI-23**, the basic four-ring remains intact. However, the two iron centers in the four-polyhedra ring are now additionally linked through the aforementioned $\{MoO_4\}$ or $\{Mo_2O_7\}$ moieties. Thus, bridging of adjacent iron octahedra in **MOXI-22** and **MOXI-23** alternates between two molybdenum tetrahedra and either three molybdenum tetrahedra or two molybdenum tetrahedra and one dimolybdate bi-tetrahedral unit, respectively.

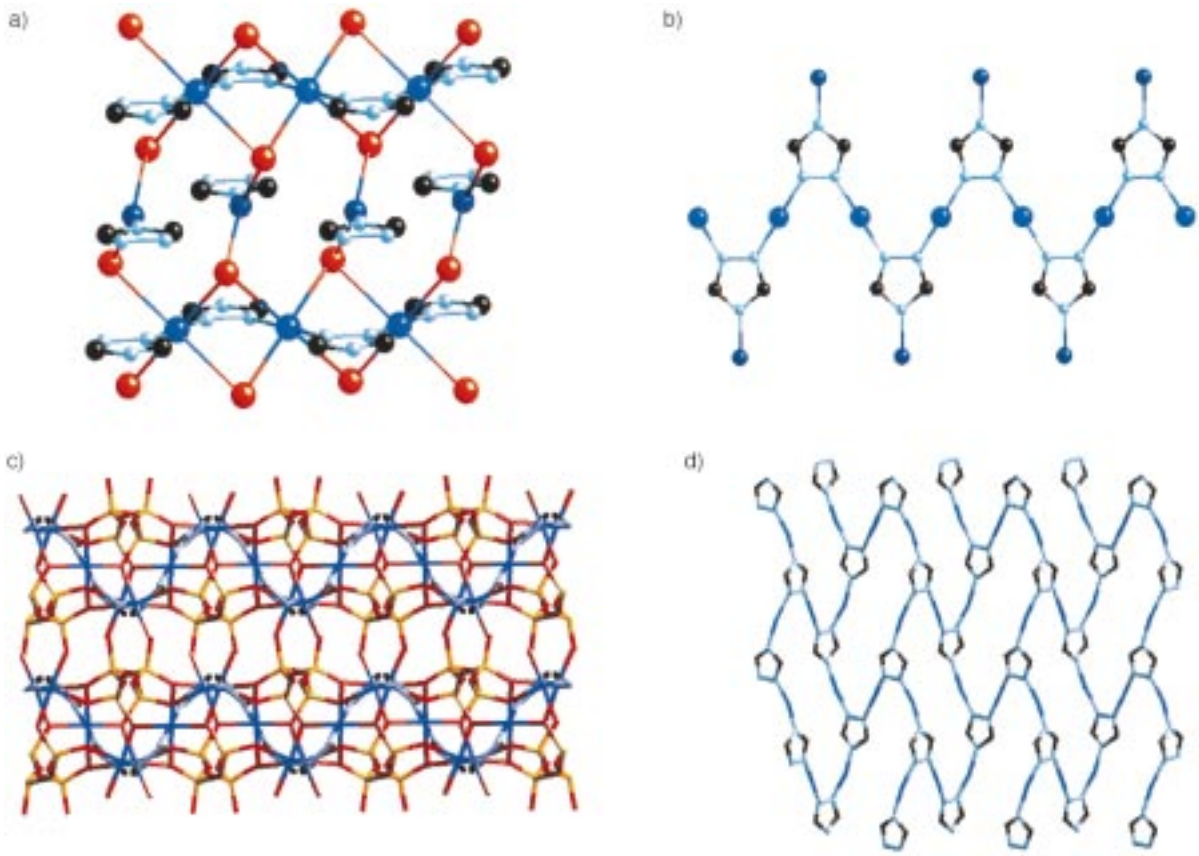

Figure 69. a) The structure of $[Cu_2Br_2(trz)]$. b) The copper–triazolate one-dimensional substructure of $[Cu_2Br_2(trz)]$. c) The structure of $[Cu_3(trz)_2V_4O_{12}]$. d) The copper–triazolate two-dimensional substructure of $[Cu_3(trz)_2V_4O_{12}]$.

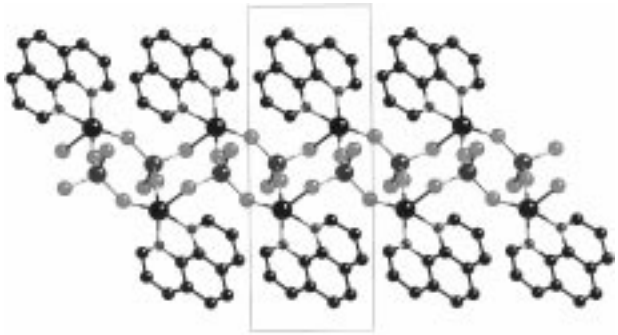

Figure 70. The structure of **MOXI-20**.

The final examples again illustrate the exploitation of bridging organodiamine ligands of significantly different donor-to-donor extension in providing structures with distinctive M′-O-Mo arrays. As shown in Figure 72, the structure of $[Cu(bpa)_{0.5}MoO_4]$ (**MOXI-24**) consists of $\{CuMoO_4\}$ bimetallic oxide layers covalently linked through bpa ligands into a three-dimensional framework. The structure exhibits the pattern of alternating organic–inorganic regions characteristic of the metal–organophosphonate phases.[44] The inorganic layer is constructed from $\{MoO_4\}$ tetrahedra and $\{CuO_5N\}$ octahedra which form double chains linked through {Cu-O-Mo} bridges into a two-dimensional network. One Cu site forms corner-sharing interactions with five adjacent Mo sites of the chain, while the second Cu site forms four corner-sharing linkages to Mo chain sites and one to an Mo site of an adjacent chain. In addition, the two unique Cu sites form a binuclear edge-sharing unit through a $\{Cu_2O_2\}$ interaction. One Mo site bridges three Cu binuclear units of a given chain and provides linkage to an adjacent chain through its fourth oxo group. The second Mo site bridges three Cu binuclear units of the chain and projects a terminal oxo group into the interlamellar region.

In comparing **MOXI-24** to $[Cu(bpe)MoO_4]$ (**MOXI-1**), the influence of ligand types on oxide structure is revealed. In contrast to **MOXI-1**, which contains {Cu-bpe-Cu-} chains with $\{CuO_4N_2\}$ coordination geometry, **MOXI-24** exhibits {Cu-bpa-Cu} binuclear units; that is, there is no {Cu-diamine-Cu-} chain propagation and the coordination geometry is $\{CuO_5N\}$. As shown in Figure 49, the layer structure adopted by **MOXI-1** consists of simple $\{Cu_3Mo_3O_6\}$ fused rings rather than the more complex connectivity enjoyed by **MOXI-24**. The consequences of ligand geometry are also manifest in the packing diagrams for **MOXI-1** and **MOXI-24**, shown in Figures 49 and 72, respectively.

Two contrasting geometric features of the ligands bpa and bpe are evident: the angles between the donor groups and the Cu–Cu distances imposed by linker length, 11.74 Å and 13.56 Å for **MOXI-24** and **MOXI-1**, respectively. To assess the influence of donor-group separation on structure, the oxide $[Cu(pz)_{0.5}MoO_4]$ (**MOXI-25**) was prepared. The structure consists of a complex three-dimensional bimetallic oxide with channels occupied by the pyrazine ligand (Figure 73). The

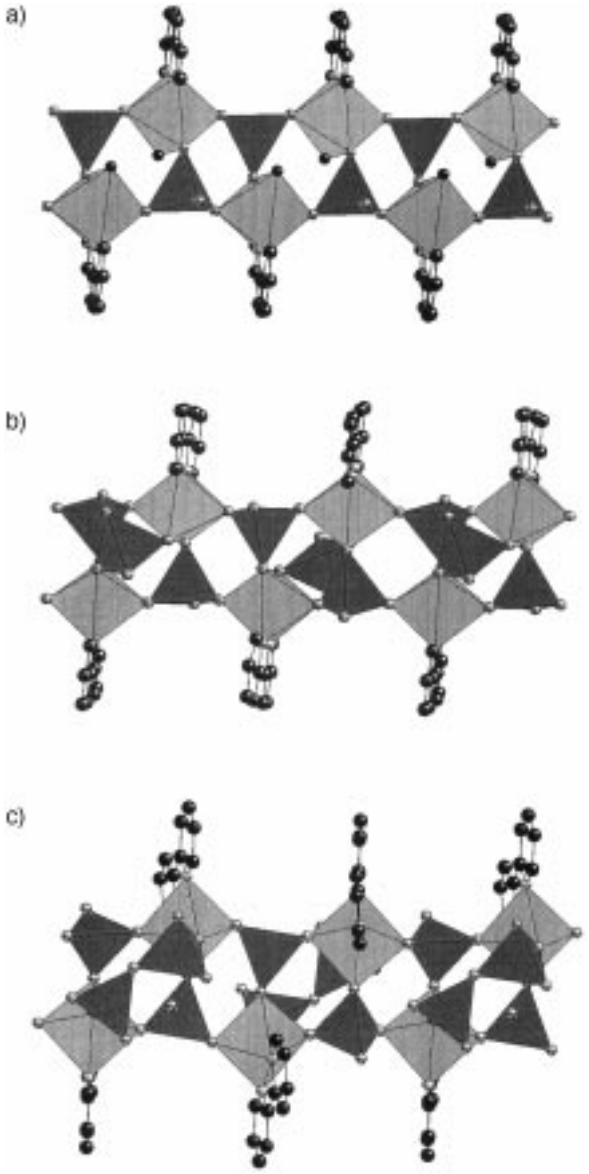

Figure 71. The chain structures of a) **MOXI-21**, b) **MOXI-22**, and c) **MOXI-23**.

structure is constructed from corner-sharing $\{MoO_4\}$ tetrahedra and $\{CuO_4N\}$ square pyramids, which form chains of stacked $\{Cu_2Mo_2O_4\}$ rings. Each Mo site links three adjacent Cu sites of a chain and employs the fourth oxo group to connect to an adjacent chain. Four adjacent chains are linked to form a cavity occupied by the pyrazines which serve to ligate to Cu sites of opposite chains.

5. Conclusions

Organodiamine-templated metal oxides represent a new class of materials in which an organic component exerts a crucial role in dictating the inorganic oxide microstructure. While in other examples of organic–inorganic hybrid materials, such as zeolites, MCM-41 type mesoporous materials, and TMPO's, the organic component adopts the role of charge-compensating and space-filling counterion for the negatively charged metal oxide skeleton, the organic components of the molybdenum oxide class manifest a variety of structural roles, including templating, tethering of functional groups, passivation of metal coordination spheres to produce low-dimensionality materials, and imprinting of structural information upon thermal removal.

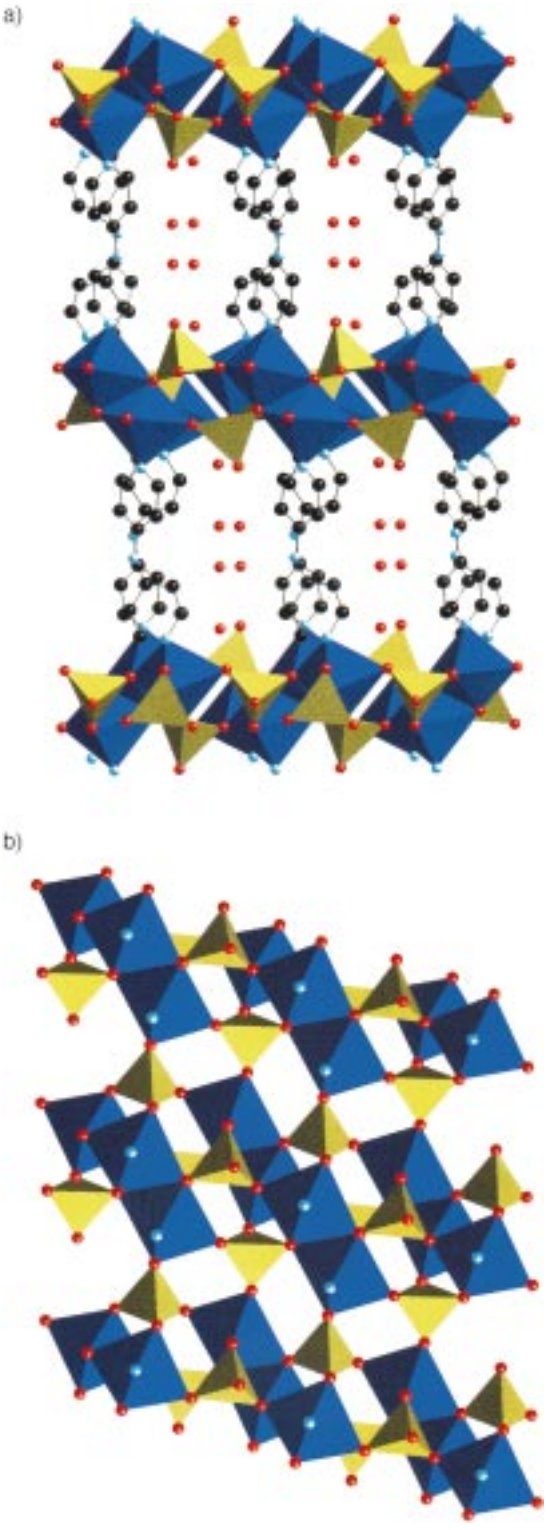

Figure 72. a) A view of the covalently linked three-dimensional structure of **MOXI-24**, showing the ligand bridging of $\{CuMoO_4\}$ layers. b) The $\{CuMoO_4\}$ layer structure of **MOXI-24**.

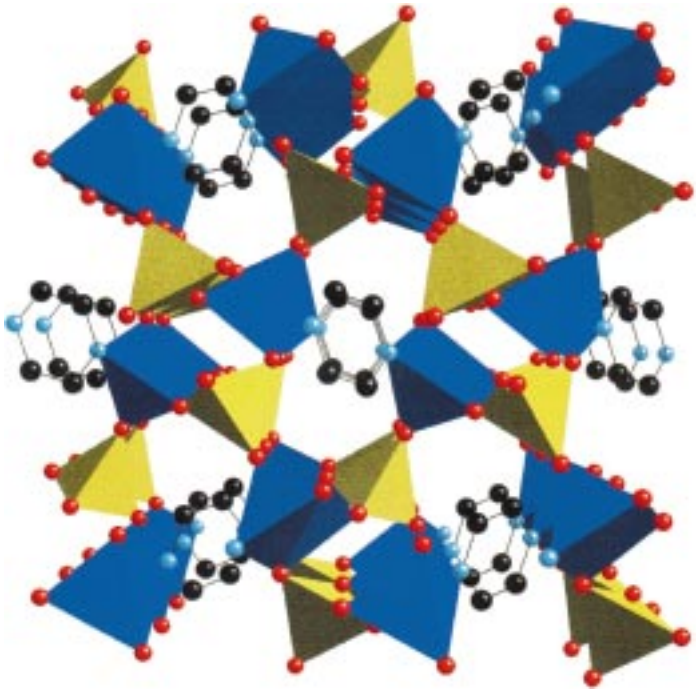

Figure 73. A view of the structure of **MOXI-25**, showing the channels occupied by the pyrazine ligands.

Of the three subclasses of organodiamine-molybdenum oxide solids, those based on the organodiamine as protonated cation and on direct ligation of the organodiamine to the oxide skeleton reflect the common modes of incorporation of organodiamines into coordination chemistry in general and are not unanticipated. The MOXI structures characterized by organodiammonium cations exhibit one- and two-dimensional structures, an observation consistent with the routine occurrence of low-dimensional structures in the inorganic molybdenum oxide chemistry. Such organic cation templated materials also reveal the structural role of multipoint hydrogen bonding and of the partitioning of the solid into polar and nonpolar domains. While the number of examples is too limited to draw general conclusions, it does appear that organodiammonium cations with alkyl backbones favor one-dimensional structures, while those with aromatic linkers provide layered network structures. This observation may reflect the greater facility for intercalation between oxide layers of flat aromatic residues which would favor two-dimensional structures, while the more effective multipoint hydrogen bonding propensities of the aliphatic NH_3^+ terminus, in contrast to the iminium $RR'R''NH^+$ terminus of the aromatic organoamines, might serve to disrupt propagation of oxide bridging interactions in more than one dimension.

The consequences of ligation of organodiamine groups directly to the molybdenum oxide skeleton are apparent in the passivation of the oxide surface, which again results in low-dimensionality oxide substructures. However, the influences of ligand geometry are also manifest in this small group of materials. Chelating bipyridyl ligands, such as 2,2′-bpy, by blocking two coordination sites on the same metal center and subtending a large volume of the coordination sphere with the organic residue passivate the metal toward oxide bridging in more than one dimension. In contrast, when the ligand geometry enforces a bridging modality on the nitrogen donors, more complex structures are observed, such as the hydrogen-bonded sheetlike structure of $[Mo_4O_{13}(Hbpa)_2]$ (**MOXI-7**) and the organically buttressed two-dimensional molybdenum oxide structure of $[MoO_3(4,4'\text{-bpy})_{0.5}]$ (**MOXI-8**).

The subclass of organodiamine-molybdenum oxides incorporating cationic coordination polymers is a natural evolution of the recent dramatic developments in the designed synthesis of coordination polymers through the propagation of structural characteristics by tethered donors of fixed geometries. The brief introduction to the organodiamine coordination polymers in Section 3 of this review reveals a remarkably diverse structural chemistry which reflects a number of characteristics including tether length and geometry, the disposition of the donor groups, the presence of additional functional groups, the coordination preferences of the metal and its oxidation state, and the role of the anion. While this latter influence has often been overlooked, it is manifest in the contrasting structures of $[Ag(pytz)(MeCN)](PF_6)$ and $[Ag(pytz)(NO_3)]$ and in the structural role of the coordinating sulfate oxoanions in the structures of **CUSO 1–3**. Molybdate, whether as monomeric $[MoO_4]^{2-}$ or as oligomeric $[Mo_xO_y]^{2-}$ or as one- or two-dimensional networks, may be considered a charge-balancing anion for the cationic coordination polymer. The two component units would seem ideally suited for the preparation of new complex ionic materials.

A consistent feature of the MOXI materials of this subclass is the absence of interpenetration of coordination polymer frameworks, a characteristic attribute of coordination polymer structures with "innocent" anions. The exclusion of interpenetration of polymer units in the MOXI materials reflects both the effective space-filling role of the molybdenum oxide anion component and ligation of the oxide to the coordination polymer through bridging oxo group interactions. Such interactions can be relatively weak, as in the case of $[Cu(4,4'\text{-bpy})]_4[Mo_{15}O_{47}]$ where the distinctiveness of the coordination polymers and molybdenum oxide chains is evidently maintained, or quite strong as for $[Cu(bpe)MoO_4]$, where the Cu^{II} centers have been intimately incorporated into the bimetallic oxide layer.

While both ligand geometry and the coordination preferences of the heterometal play a structural role, it is premature to offer more than a tentative analysis of their influences on the synthetic design. Extension of the spacer between nitrogen donors may favor layer structures. The structures of both $[Cu(bpe)MoO_4]$ and $[Cu(bpa)_{0.5}MoO_4]$ exhibit the characteristic pattern of metal oxide sheets alternating with organic tethers, a motif shared by metal organodiphosphonates, $[M_x(O_3P\text{-linker-}PO_3)_y]$.[185] Such partitioning into polar and nonpolar domains appears to be a structural characteristic of such hybrid materials.

Of course, an obvious expedient is to minimize the distance between donors, as in pyrazine or pyrimidine. The structural chemistry is now quite different from that observed for copper-pyrazine and copper-pyrimidine with conventional anions, reviewed in Section 3.5. The structures of $[Cu(pz)_{0.5}MoO_4]$ (**MOXI-25**) and $[Cu_2(pyrd)Mo_3O_{10}]$ (**MOXI-19**) do

not possess cationic coordination polymer subunits but rather exhibit incorporation of the copper into the three-dimensional copper-molybdate framework with the organic component occupying well-defined channels in the framework. It may be that sterically less demanding organic components can be more readily accommodated in the void volumes of three-dimensional frameworks, whereas extended rodlike tethers dictate two dimensional networks or discrete coordination polymer substructures. As evidenced by the structures of $[Cu_2Br_2(trz)]$, $[Cu_3(trz)_2V_4O_{12}]$, and $[\{Cu_2(trz)_2(H_2O)_2\}Mo_4O_{13}]$, the anionic component of these materials is not simply a "clay" to be molded by the engineered polymer substructure, but rather exerts a pronounced influence on the cationic substructure. The synergistic relationship between the substructures of these composite oxide materials belies a simple "ship in the bottle" approach to their design and reveals a complex chemistry at the organic–inorganic interface. This observation suggests that predictability of detailed structural features in the designed synthesis of such materials will continue to prove problematic.

The current interest in inorganic solid-state materials reflects useful properties derived from molecular recognition which result in applications to sorption, catalysis, molecular electronics, and optical systems. Molecular recognition in the sense of appropriate juxtaposition of functional groups for reactivity and cooperative electronic effects is often related to the periodicity of the crystalline state. These considerations render the pursuits of designed synthesis and crystal engineering quite attractive. While completely predictable design remains elusive, the introduction of organodiamine components has allowed us to fashion a new class of composite materials with novel two- and three-dimensional bimetallic oxide structures with channels and cavities whose dimensions are dictated by the geometry of the organodiamine.

However, it is also evident that the synthesis of the MOXI family of materials has achieved at best a primitive degree of design and predictability. Such composite materials are complex, possessing an interactive structural hierarchy. Furthermore, in addition to this spatial hierarchy, such materials are generally metastable kinetic phases requiring a shift in paradigm from the thermodynamic to the kinetic domain. This intrinsic dynamic nature of such materials further enhances their essential complexity. Such complexity sets limits on the degree of predictability.[186] Arguably, design does not require total predictability, but rather an appreciation of the reciprocity of structure–function relationships. This suggests that as the products of empirical development are unravelled, control of desired properties will be achieved.

The evolution of the MOXI family of materials will require continued definition of the chemical possibilities. These include not only the roles of ligand geometries and heterometal coordination preferences but a systematic investigation of the vast hydrothermal parameter space, which includes factors such as pH value, stoichiometries, temperature, fill volume, and sacrificial precursors. As the data base for these materials expands, the synthetic and structural patterns will emerge as well as an appreciation for the structure–function relationships of this family of oxides.

This work was supported by NSF Grant CHE9617232. We also thank the Keck Foundation for partial funding of the X-ray crystallographic laboratory.

Received: June 8, 1998
Supplemented version: October 19, 1998 [A285IE]
German version: *Angew. Chem.* **1999**, *111*, 2798–2848

[1] N. N. Greenwood, A. Earnshaw, *Chemistry of the Elements*, Pergamon Press, New York, **1984**.
[2] "Inorganic Biomaterials": L. L. Hench in *Materials Chemistry, An Emerging Discipline, Ser. 245* (Eds.: L. V. Interrante, L. A. Casper, A.-B. Ellis), American Chemical Society, **1995**, chap. 21, pp. 523–547.
[3] B. Mason, *Principles of Geochemistry*, 3rd ed., Wiley, New York, **1966**.
[4] S. Mann, *J. Chem. Soc. Dalton Trans.* **1993**, 1.
[5] S. Mann, S. L. Burkett, S. A. Davis, C. E. Fowler, N. H. Mendelson, S. D. Sims, D. Walsh, N. T. Whilton, *Chem. Mater.* **1997**, *9*, 2300.
[6] A. F. Wells, *Structural Inorganic Chemistry*, 4th ed., Oxford University Press, Oxford, **1975**.
[7] T. G. Reynolds, R. C. Buchanan in *Ceramic Materials for Electronics* (Ed.: R. C. Buchanan), 2nd ed., Dekker, New York, **1991**, p. 207.
[8] W. Büchner, R. Schliebs, G. Winter, K. H. Büchel, *Industrial Inorganic Chemistry*, VCH, New York, **1989**.
[9] W. H. McCarroll in *Encyclopedia of Inorganic Chemistry*, *Vol. 6* (Ed.: R. B. King), Wiley, New York, **1994**, p. 2903.
[10] G. H. Hartling in *Ceramic Materials for Electronics* (Ed.: R. C. Buchanan), 2nd ed., Dekker, New York, **1991**, p. 129.
[11] H. W. Leverenz, *Luminescence of Solids*, Wiley, New York, **1980**.
[12] R. Einzinger, *Annu. Rev. Mater. Sci.* **1987**, *17*, 299.
[13] J. M. Tarascon, P. Barboux, P. F. Miceli, L. H. Greene, G. W. Hull, M. Eibschutz, S. A. Sunshine, *Phys. Rev. B* **1988**, *37*, 7458.
[14] D. I. Makin in *Modern Oxide Materials* (Eds.: B. Cockayne, D. W. Jones), Academic Press, New York, **1972**, p. 235.
[15] C. N. R. Rao, K. J. Rao in *Solid State Compounds* (Eds.: A.-K. Cheetham, P. Day), Clarendon Press, Oxford, **1992**, p. 281.
[16] J. D. Bierlein, C. B. Arweiler, *Appl. Phys. Lett.* **1987**, *49*, 917.
[17] G. Centi, F. Trifuro, J. R. Ebner, V. M. Franchetti, *Chem. Rev.* **1988**, *88*, 55.
[18] R. K. Grasselli, *Appl. Catal.* **1985**, 15, 127.
[19] M. Gasior, I. Gasior, B. Grzybowska, *Appl. Catal.* **1984**, *10*, 87.
[20] T. Okuhara, M. Misono in *Encyclopedia of Inorganic Chemistry*, *Vol. 6* (Ed.: R. R. King), Wiley, New York, **1994**, p. 2889.
[21] H. Niiyama, E. Echigoya, *Bull. Chem. Soc. Jpn* **1972**, *45*, 655.
[22] T. Yamaguchi, *Appl. Catal.* **1990**, *61*, 1.
[23] A. Clearfield, *Chem. Rev.* **1988**, *88*, 125.
[24] J. M. Newsam in *Solid State Compounds* (Eds.: A.-K. Cheetham, P. Day), Clarendon Press, Oxford, **1992**, p. 234.
[25] D. M. Ruthven, *Principles of Absorption and Absorption Processes*, Wiley-Interscience, New York, **1984**.
[26] R. Szostak, *Molecular Sieves—Principles of Synthesis and Identification*, Van Nostrand Rheinhold, New York, **1988**.
[27] J. A. Raleo, *Zeolite Chemistry and Catalysis*, ACS Monograph (7), American Chemical Society, Washington, DC, **1976**.
[28] *New Developments in Zeolite Science* (Eds.: Y. Murakami, A. Iijima, J. W. Ward), Elsevier, Amsterdam, **1986**.
[29] D. E. W. Vaughan, *Properties and Applications of Zeolites*, (Ed.: R. P. Townsend), The Chemical Society, London, **1979**, p. 294 (Chem. Soc. Special Publ. No. 33).
[30] S. I. Stupp, P. V. Braun, *Science* **1997**, *277*, 1242.
[31] C. M. Zaremba, A. M. Belcher, M. Fritz, Y. Li, S. Mann, P. K. Mansma, D. E. Morse, J. S. Speck, G. D. Stucky, *Chem. Mater.* **1996**, *8*, 679.
[32] J. V. Smith, *Chem. Rev.* **1988**, *88*, 149.
[33] M. L. Occelli, H. C. Robson, *Zeolite Synthesis*, American Chemical Society, Washington, DC, **1989**.
[34] C. T. Kresge, M. E. Leonowicz, W. J. Roth, J. C. Vartuli, J. S. Beck, *Nature* **1992**, *359*, 710.
[35] S. Mann, *Nature* **1993**, *365*, 499.

[36] R. C. Haushalter, L. A. Mundi, *Chem. Mater.* **1992**, *4*, 31.
[37] M. I.Khan, L. M. Meyer, R. C. Haushalter, C. L. Schweitzer, J. Zubieta, J. L. Dye, *Chem. Mater.* **1996**, *8*, 43.
[38] S. Mann, G. Ozin, *Nature* **1996**, *382*, 313.
[39] J. C. MacDonald, G. M. Whitesides, *Chem. Rev.* **1994**, *94*, 2383.
[40] R. M. Barrer, *Hydrothermal Chemistry of Zeolites*, Academic Press, New York, **1982**.
[41] J. S. Beck, J. C. Vartuli, W. J. Roth, M. E. Leonowicz, C. T. Kresge, R. D. Schmitt, C. T.-W. Chen, D. H. Olson, E. W. Sheppard, S. B. McCullen, J. B. Higgins, J. L. Schlenker, *J. Am. Chem. Soc.* **1992**, *114*, 10834.
[42] R. C. Haushalter, K. G. Strohmaier, F. W. Lai, *Science* **1989**, *246*, 1289.
[43] C. Warren, R. C. Haushalter, J. Zubieta, unpublished results.
[44] M. I.Khan, J. Zubieta, *Prog. Inorg. Chem.* **1995**, *43*, 1.
[45] A. Rabenau, *Angew. Chem.* **1985**, *97*, 1017; *Angew. Chem. Int. Ed. Engl.* **1985**, *24*, 1026.
[46] R. A. Laudise, *Chem. Eng. News* **1987**, *65*(39), 30.
[47] J. Gopalakrishnan, *Chem. Mater.* **1995**, *7*, 1265.
[48] V. Soghomonian, Q. Chen, R. C. Haushalter, J. Zubieta, C. J. O'Connor, Y.-S. Lee, *Chem. Mater.* **1993**, *5*, 1690.
[49] M. I. Khan, Y.-S. Lee, C. J. O'Connor, R. C. Haushalter, J. Zubieta, *Chem. Mater.* **1994**, *6*, 721.
[50] M. I. Khan, R. C. Haushalter, C. J. O'Connor, J. Zubieta, *Chem. Mater.* **1995**, *7*, 593.
[51] Y. Zhang, J. R. D. DeBord, C. J. O'Connor, R. C. Haushalter, G. Clearfield, J. Zubieta, *Angew. Chem.* **1996**, *108*, 1067; *Angew. Chem. Int. Ed. Engl.* **1996**, *33*, 989.
[52] M. J. Zaworotko, *Chem. Soc. Rev.* **1994**, *23*, 283.
[53] M. Fujita, Y. J. Kwon, S. Washiza, K. Ogura, *J. Am. Chem. Soc.* **1994**, *116*, 1151.
[54] "Supramolecular Architecture" (Ed.: T. Bein): *ACS Symp. Ser.* **1992**, *499*.
[55] O. Ermer, *Adv. Mater.* **1991**, *3*, 608.
[56] K. Inoue, T. Hayamizu, H. Iwamura, D. Hashizume, Y.Ohashi, *J. Am. Chem. Soc.* **1996**, *118*, 1803.
[57] R. Robson in *Comprehensive Supramolecular Chemistry*, *Vol. 6* (Eds.: J. L. Atwood, J. E. D. Davies, D. D. MacNicol, F. Vögtle, J.-M. Lehn), Pergamon, New York, **1996**, p. 733.
[58] G. R. Desiraju, *Crystal Engineering. The Design of Organic Solids*, Elsevier, Amsterdam, **1989**.
[59] M. C. Etler, *Acc. Chem. Res.* **1990**, *23*, 120.
[60] J. M. Lehn, *Pure Appl. Chem.* **1994**, *66*, 1961.
[61] T. Iwamoto in *Comprehensive Supramolecular Chemistry*, *Vol. 6* (Eds.: J. L. Atwood, J. E. D. Davies, D. D. MacNicol, F. Vögtle, J.-M. Lehn), Pergamon, New York, **1996**, p. 643.
[62] B. F. Abrahams, B. F. Hoskins, D. Michail, R. Robson, *Nature* **1994**, *369*, 727.
[63] A. J. Blake, S. J. Hill, P. Hubberstey, W.-S. Li, *J. Chem. Soc. Dalton Trans.* **1997**, 913.
[64] M.-X. Li, G.-Y. Xie, Y.-D. Gu, J. Chen, P.-J. Zheng, *Polyhedron* **1995**, *14*, 1235.
[65] X.-M. Chen, M.-L. Tong, Y.-J. Luo, Z.-N. Chen, *Aust. J. Chem.* **1996**, *49*, 835.
[66] L. Carlucci, G. Ciani, D. M. Proserpio, A. Sironi, *J. Chem. Soc. Dalton Trans.* **1997**, 1801.
[67] A. S. Batsanov, M. J. Begley, P. Hubberstey, J. Stroud, *J. Chem. Soc. Dalton Trans.* **1996**, 1947.
[68] P. Losier, M. J. Zaworotko, *Angew. Chem.* **1996**, *108*, 2957; *Angew. Chem. Int. Ed. Engl.* **1996**, *35*, 2779.
[69] O. M. Yaghi, H. Li, T. L. Groy, *Inorg. Chem.* **1997**, *36*, 4292.
[70] N. Masciocchi, P. Cairati, L. Carlucci, G. Mezza, G. Ciani, A. Sironi, *J. Chem. Soc. Dalton Trans.* **1996**, 2739.
[71] a) F. Robinson, M. J. Zaworotko, *J. Chem. Soc. Chem. Commun.* **1995**, 2413; b) O. M. Yaghi, H. Li, *J. Am. Chem. Soc.* **1996**, *118*, 295.
[72] D. Hagrman, R. P. Hammond, R. C. Haushalter, J. Zubieta, *Chem. Mater.* **1998**, *10*, 2091.
[73] A. J. Blake, S. J. Hill, P. Hubberstey, W.-S. Li, *J. Chem. Soc. Dalton Trans.* **1998**, 909.
[74] M. Fujita, Y. J. Kwon, S. Washizu, K. Ogura, *J. Am. Chem. Soc.* **1994**, *116*, 1151.
[75] R. W. Gable, B. F. Hoskins, R. Robson, *J. Chem. Soc. Chem. Commun.* **1990**, 1677.
[76] S. Subramanian, M. J. Zaworotko, *Angew. Chem.* **1995**, *107*, 2295; *Angew. Chem. Int. Ed. Engl.* **1995**, *34*, 2127.
[77] J. Li, H. Zeng, J. Chen, Q. Wang, X. Wu, *Chem. Commun.* **1997**, 1213.
[78] M. Kondo, T. Yoshitomi, K. Seki, H. Matsuzaka, S. Kitagawa, *Angew. Chem.* **1997**, *109*, 1844; *Angew. Chem. Int. Ed. Engl.* **1997**, *36*, 1725.
[79] O. M. Yaghi, G. Li, *Angew. Chem.* **1995**, *107*, 232; *Angew. Chem. Int. Ed. Engl.* **1995**, *34*, 207.
[80] M.-L. Tong, B.-H. Ye, J.-W. Cai, X.-M. Chen, S. W. Ng, *Inorg. Chem.* **1998**, *37*, 2645.
[81] L. Carlucci, G. Ciani, D. M. Proserpio, A. Sironi, *J. Chem. Soc. Chem. Commun.* **1994**, 2755.
[82] L. R. MacGillivray, S. Subramamian, M. J. Zaworotko, *J. Chem. Soc. Chem. Commun.* **1994**, 1325.
[83] S. Lopez, M. Kahraman, M. Harmata, S. W. Keller, *Inorg. Chem.* **1997**, *36*, 6138.
[84] O. M. Yaghi, H. Li, *J. Am. Chem. Soc.* **1995**, *117*, 10401.
[85] A. J. Blake, N. R. Champness, A. Khlobystov, D. A. Lemenovskii, W.-S. Li, M. Schröder, *Chem. Commun.* **1997**, 2027.
[86] M. Fujita, Y. J. Kwon, O. Sasaki, K. Yamaguchi, K. Ogura, *J. Am. Chem. Soc.* **1995**, *117*, 7287.
[87] L. Carlucci, G. Ciani, D. W. v. Gudenberg, D. M. Proserpio, *Inorg. Chem.* **1997**, *36*, 3812.
[88] T. L. Hennigar, D. C. MacQuarie, P. Losier, R. D. Rogers, M. J. Zaworotko, *Angew. Chem.* **1997**, *109*, 1044, *Angew. Chem. Int. Ed. Engl.* **1997**, *36*, 972.
[89] M. Fujita, Y. J. Kwon, M. Miyazawa, K. Ogura, *J. Chem. Soc. Chem. Commun.* **1994**, 1977.
[90] L. Carlucci, G. Ciani, P. Macchi, D. M. Proserpio, *Chem. Commun.* **1998**, 1837.
[91] M. A. Withersby, A. J. Blake, N. R. Champness, P. Hubberstey, W.-S. Li, M. Schröder, *Angew. Chem.* **1997**, *109*, 2421; *Angew. Chem. Int. Ed. Engl.* **1997**, *36*, 2327.
[92] M. J. Hannon, C. L. Painting, W. Errington, *Chem. Commun.* **1997**, 1805.
[93] A. Neels, H. Stoeckli-Evans, A. Escuer, R. Vicente, *Inorg. Chem.* **1995**, *34*, 1946.
[94] O.-S. Jung, S. H. Park, D. C. Kim, K. M. Kim, *Inorg. Chem.* **1998**, *37*, 610.
[95] C. L. Schauer, E. Matwey, F. W. Fowler, J. W. Lauher, *J. Am. Chem. Soc.* **1997**, *119*, 10245.
[96] K. N. Power, T. L. Hennigar, M. J. Zaworotko, *Chem. Commun.* **1998**, 595.
[97] M. O'Keeffe, *Z. Kristallogr.* **1991**, *196*, 21.
[98] M. O'Keeffe, *Nature* **1998**, *392*, 879.
[99] A. J. Blake, N. R. Champness, S. S. M. Chung, W.-S. Li, M. Schröder, *Chem. Commun.* **1997**, 1005.
[100] A. J. Blake, N. R. Champness, A. N. Khlobystov, D. A. Lemenovskii, W.-S. Li, M. Schröder, *Chem. Commun.* **1997**, 1339.
[101] A. J. Blake, N. R. Champness, S. S. M. Chung, W.-S. Li, M. Schröder, *Chem. Commun.* **1997**, 1675.
[102] B. F. Hoskins, R. Robson, D. A. Slizys, *J. Am. Chem. Soc.* **1997**, *119*, 2952.
[103] B. F. Hoskins, R. Robson, D. A. Slizys, *Angew. Chem.* **1997**, *109*, 2430; *Angew. Chem. Int. Ed. Engl.* **1997**, *36*, 2336.
[104] R. LaDuca, Jr., J. Zubieta, unpublished results.
[105] L. P. Wu, Y. Yamagiwa, T. Kuroda-Sowa, T. Kamikawa, M. Munakata, *Inorg. Chim. Acta.* **1997**, *256*, 155.
[106] P. C. M. Duncan, D. M. L. Goodgame, S. Menzer, D. J. Williams, *Chem. Commun.* **1996**, 2127.
[107] D. Venkataraman, S. Lee, J. S. Moore, P. Zhang, K. A. Hirsch, G. B. Gardner, A. C. Covey, C. L. Prentice, *Chem. Mater.* **1996**, *8*, 2030.
[108] M. Bertelli, L. Carlucci, G. Ciani, D. M. Proserpio, A. Sironi, *J. Mater. Chem.* **1997**, *7*, 1271.
[109] J. G. J. Jarvis, *Acta Crystallogr.* **1962**, *15*, 964.
[110] B. F. Abraham, S. R. Batten, H. Hamit, B. F. Hoskins, R. Robson, *Angew. Chem.* **1996**, *108*, 1794; *Angew. Chem. Int. Ed. Engl.* **1996**, *35*, 1690.
[111] S. R. Batten, B. F. Hoskins, R. Robson, *Angew. Chem.* **1995**, *107*, 884, *Angew. Chem. Int. Ed. Engl.* **1995**, *34*, 820;.

[112] S. R. Batten, B. F. Hoskins, R. Robson, *J. Am. Chem. Soc*. **1995**, *117*, 5385.
[113] L. Carlucci, G. Ciani, D. M. Proserpio, A. Sironi, *J. Am. Chem. Soc.* **1995**, *117*, 4562.
[114] a) M. Inoue, M. Kubo, *Coord. Chem. Rev.* **1976**, *21*, 1; b) P. J. Steel, *Coord. Chem. Rev.* **1990**, *106*, 227.
[115] R. Hammond, J. Zubieta, unpublished results.
[116] R. G. Vranka, E. L. Amma, *Inorg. Chem.* **1966**, *5*, 1020.
[117] T. Otieno, S. J. Retting, R. C. Thompson, J. Trotter, *Can. J. Chem.* **1989**, *67*, 1964.
[118] T. Otieno, S. J. Retting, R. C. Thompson, J. Trotter, *Can. J. Chem.* **1990**, *68*, 1901.
[119] T. Fetzer, A. Lentz, T. Debaerdemaeker, *Z. Naturforsch. B* **1989**, *44*, 553.
[120] J. Pickardt, B. Staub, *Z. Naturforsch. B* **1996**, *51*, 947.
[121] F. Kubel, J. Strahle, *Z. Naturforsch. B* **1981**, *36*, 441.
[122] M. Munakata, L. P. Wu, T. Kuroda-Sowa, M. Maekawa, K. Moriwaki, S. Kitagawa, *Inorg. Chem*. **1997**, *36*, 5416.
[123] J. Pickardt, B. Staub, *Z. Naturforsch. B* **1997**, *52*, 1456.
[124] S. Kawata, S. Kitagawa, H. Kimagai, S. Iwabuchi, M. Katada, *Inorg. Chim. Acta* **1998**, *267*, 143.
[125] L. Carlucci, G. Ciani, D. M. Proserpio, A. Sironi, *Inorg. Chem.* **1995**, *34*, 5698.
[126] L. Carlucci, G. Ciani, D. M. Proserpio, A. Sironi, *Angew. Chem.* **1995**, *107*, 2037; *Angew. Chem. Int. Ed. Engl*. **1995**, *34*, 1895.
[127] C. V. K. Sharma, S. T. Griffin, R. D. Rogers, *Chem. Commun.* **1998**, 215.
[128] F. Lloret, G. DeMunno, M. Julve, J. Cano, R. Ruiz, A. Caneschi, *Angew. Chem.* **1998**, *110*, 143; *Angew. Chem. Int. Ed. Eng.* **1998**, *37*, 135.
[129] J. S. Haynes, S. J. Retting, J. R. Sams, R. C. Thompson, J. Trotter, *Can. J. Chem.* **1987**, *65*, 420.
[130] T. Otieno, S. J. Retting, R. C. Thompson, J. Trotter, *Inorg. Chem.* **1993**, *32*, 1607.
[131] J. A. Real, G. DeMunno, M. C. Munoz, M. Julve, *Inorg. Chem.* **1991**, *30*, 2701.
[132] P. W. Carreck, M. Goldstein, E. M. McPartlin, W. D. Unsworth, *J. Chem. Soc. Chem. Commun.* **1971**, 1634.
[133] L. Carlucci, G. Ciani, D. M. Proserpio, A. Sironi, *Chem. Commun*. **1996**, 1393.
[134] S. W. Keller, *Angew. Chem.* **1997**, *109*, 295; *Angew. Chem. Int. Ed. Engl.* **1997**, *36*, 247.
[135] L. Carlucci, G. Ciani, D. M. Proserpio, A. Sironi, *Inorg. Chem*. **1997**, *36*, 1736.
[136] L. Carlucci, G. Ciani, D. W. v. Gudenberg, D. M. Proserpio, A. Sironi, *Chem. Commun*. **1997**, 631.
[137] A. Michelet, B. Voissat, P. Khodadad, N. Rodier, *Acta. Crytallogr. Sect. B* **1981**, *37*, 2171.
[138] L. Carlucci, G. Ciani, D. M. Proserpio, A. Sironi, *J. Am. Chem. Soc*. **1995**, *117*, 12861.
[139] B. F. Hoskins, R. Robson, D. A. Slizys, *Angew. Chem.* **1997**, *109*, 2861; *Angew. Chem. Int. Ed. Engl.* **1997**, *36*, 2752.
[140] M.-L. Tong, X.-M. Chen, X.-L. Yu, T. C. W. Mak, *J. Chem. Soc. Dalton Trans.* **1998**, 5.
[141] D. Hagrman, R. C. Haushalter, J. Zubieta, *Chem. Mater*. **1998**, *10*, 361.
[142] M. I. Khan, J. Zubieta, *Inorg. Chim. Acta*. **1993**, *213*, 325.
[143] Y. Xu, L.-H. An, L.-L. Koh, *Chem. Mater*. **1996**, *8*, 814.
[144] K. Range, A. Fässler, *Acta Crystallogr. Sect C* **1990**, *46*, 488.
[145] B. M. Gatehouse, P. Leverett, *J. Chem. Soc. A* **1968**, 1398.
[146] P. J. Zapf, R. C. Haushalter, J. Zubieta, *Chem. Commun*. **1997**, 321.
[147] L. Kihlborg, *Ark. Kemi* **1963**, *21*, 357.
[148] P. J. Zapf, R. C. Haushalter, J. Zubieta, *Chem. Mater*. **1997**, *9*, 2019.
[149] P. J. Zapf, R. L. LaDuca, Jr., R. S. Rarig, Jr., K. M. Johnson III, J. Zubieta, *Inorg. Chem.* **1998**, *37*, 3411.
[150] P. J. Zapf, J. Zubieta, unpublished results.
[151] R. L. LaDuca, Jr., P. J. Zapf, C. J. Warren, R. C. Haushalter, J. Zubieta, unpublished results.
[152] J. W. Johnson, A. J. Jacobson, S. M. Rich, J. F. Brody, *J. Am. Chem. Soc.* **1981**, *103*, 8246.
[153] R. Roussean, E. Canadell, P. Alemany, D. H. Galván, R. Hoffmann, *Inorg. Chem*. **1997**, *36*, 4627.
[154] S. Adams, K.-H. Ehses, J. Spilker, *Acta Crystallogr. Sect. B* **1993**, *49*, 958.
[155] P. G. Dickens, J. J. Birtill, C. J. Wright, *J. Solid State Chem*. **1979**, *28*, 185.
[156] K.-A. Wilhelmi, *Acta Chem. Scand*. **1969**, *23*, 419.
[157] S. L. Suib, *Chem. Rev.* **1993**, *93*, 803.
[158] F. J. DiSalvo, *Science* **1990**, *247*, 649.
[159] N. Prokopuk, D. F. Shriver, *Inorg. Chem*. **1997**, *36*, 5609.
[160] O. Recheweg, H.-J. Meyer, *Z. Naturforsch. B* **1995**, *50*, 1377.
[161] O. Recheweg, H.-J. Meyer, *Z. Anorg. Allg. Chem.* **1996**, *622*, 411.
[162] V. N. Molchanov, I. V. Tatjanina, E. A. Torchenkova, *J. Chem. Soc. Chem. Commun*. **1981**, 93.
[163] T. Yamase, H. Naruke, *J. Chem. Soc. Dalton. Trans.* **1991**, 285.
[164] J. R. Galán-Mascarós, C. Giménez-Saiz, S. Triki, J. Gómez-Garcia, E. Coronado, L. Ouahab, *Angew. Chem.* **1995**, *107*, 1601; *Angew. Chem. Int. Ed. Engl.* **1995**, *34*, 1460.
[165] H. T. Evans, Jr., T. J. R. Weakley, G. B. Jameson, *J. Chem. Soc. Dalton Trans.* **1996**, 2537.
[166] C. Giménez-Saiz, J. R. Galán-Mascarós, S. Triki, E. Coronado, L. Ouahab, *Inorg. Chem*. **1995**, *34*, 524.
[167] E. K. Anderson, J. Villadsen, *Acta Chem. Scand*. **1993**, *47*, 748.
[168] A. Kitamura, T. Ozaki, A. Yagasaki, *Inorg. Chem*. **1997**, *36*, 4275.
[169] I. Loose, M. Bösing, R. Klein, B. Krebs, R. P. Schulz, B. Scharbert, *Inorg. Chim. Acta*, **1997**, *263*, 99.
[170] J. R. D. DeBord, R. C. Haushalter, L. M. Meyer, D. J. Rose, P. J. Zapf, J. Zubieta, *Inorg. Chim. Acta* **1997**, *256*, 165.
[171] Y. Zhang, P. J. Zapf, L. M. Meyer, R. C. Haushalter, J. Zubieta, *Inorg. Chem*. **1997**, *36*, 2159.
[172] P. J. Zapf, C. J. Warren, R. C. Haushalter, J. Zubieta, *Chem. Commun*. **1997**, 1543.
[173] I. D. Brown in *Structure and Bonding in Crystals*, *Vol. II* (Eds.: M. O'Keefe, A. Navrotsky), Academic Press, New York, **1981**, p. 1.
[174] M. T. Pope, *Heteropoly and Isopoly Oxometalates*, Springer, New York, **1983**.
[175] M. Inoue, T. Yamase, *Bull. Chem. Soc. Jpn*. **1995**, *68*, 3055.
[176] R. Xi, B. Wang, K. Isobe, T. Nishioka, K. Toriumi, Y. Ozawa, *Inorg. Chem*. **1994**, *33*, 833.
[177] D. Hagrman, C. Zubieta, D. J. Rose, J. Zubieta, R. C. Haushalter, *Angew. Chem.* **1997**, *109*, 904; *Angew. Chem. Int. Ed. Engl.* **1997**, *36*, 795.
[178] D. Hagrman, C. Sangregorio, C. J. O'Connor, J. Zubieta, *Chem. Commun.* **1998**, 1283.
[179] D. Hagrman, P. J. Zapf, J. Zubieta, *Chem. Commun.* **1998**, 1283.
[180] P. J. Zapf, D. Hagrman, J. Zubieta, unpublished results.
[181] P. J. Zapf, R. P. Hammond, R. C. Haushalter, J. Zubieta, *Chem. Mater.* **1998**, *10*, 1336.
[182] D. Hagrman, C. J. Warren, R. C. Haushalter, R. S. Rarig, Jr., K. M. Johnson III, R. L. LaDuca, Jr., J. Zubieta, *Chem. Mater*. **1998**, *10*, 3294.
[183] R. L. LaDuca, Jr., R. Finn, J. Zubieta, unpublished results
[184] I. D. Brown, K. K. Wu, *Acta. Crystallogr. Sect. B* **1976**, *32*, 1957.
[185] D. M. Poojary, B. Zhang, A. Clearfield, *J. Am. Chem. Soc*. **1997**, *119*, 12550, and references therein.
[186] G. B. Olson, *Science* **1997**, *277*, 1237.
[187] D. Hagrman, J. Zubieta, *Chem. Commun.* **1998**, 2005.
[188] S. R. Batten, R. Robson, *Angew. Chem.* **1998**, *110*, 1558; *Angew. Chem. Int. Ed.* **1998**, *37*, 1460.